Superconductive Effects in Thin Cluster Films

John Antony Hugh Grigg

Department of Physics and Astronomy

University of Canterbury

Supervisor: Prof. Simon Brown

A thesis submitted for the degree of

Masters of Science in Physics

June 2012

Abstract

In this thesis, the superconductive and superresistive properties of thin percolating films of lead nanoclusters are presented. The samples were created by depositing clusters from an inert gas aggregation cluster source onto substrates held at either room temperature or 10K.

Observations of the characteristic behaviours of the samples were made through $R(T)$ and $V(I)$ measurements. Several interesting features were observed - smooth and discrete steps in the $R(I)$ curves, hysteresis between increasing and decreasing bias currents, and non-zero resistances at superconducting temperatures. Explanations are proposed in terms of theoretical models of several phenomena - phase slips, phase slip centres and hotspots - which have seen little prior application to percolating systems in literature.

Contents

List of Figures

LIST OF FIGURES

List of Tables

1

Introduction

Superconductivity is a phenomenon that has fascinated the minds of scientists, engineers and the general population alike. In the century that has passed since its discovery by Heike K. Onnes, huge advancements have been made in both our fundamental understanding of low-temperature physics, and in its application to many areas of technology. For example, superconducting magnets have allowed physicists to probe the origins of the universe and the particles that inhabit it through their use in supercolliders like the Large Hadron Collider, while also enabling breakthroughs in other fields like chemistry and medicine (through Nuclear Magnetic Resonance (NMR), utilised in MRI machines) [1].

Superconductivity is reasonably well-understood at macroscopic sizes in bulk materials. However, in recent decades, focus has shifted towards superconductivity in smaller-scale systems. This is an important area of research: with the ongoing trend for miniaturisation of circuitry and packing as many transistors as possible into modern computer processors it is useful to know how superconductivity scales as well and whether it is possible to utilise it in novel electronics.

One important effect that has been discovered is that as the size of a superconducting material is reduced the material does not necessarily maintain perfect conductivity. Many different nanoscale superconductors have been observed over the years, and there are numerous instances (predominantly in one and two-dimensional systems) where the superconductor does not transition directly to zero resistance as it does in the bulk, but has some finite resistance in the superconducting temperature region. Furthermore, there are superconducting systems which exhibit an increase in resistance below the

superconducting threshold. Various mechanisms have been proposed to explain these observations, but there is still controversy in the literature on many points.

In this thesis, superconducting percolating films of lead nanoclusters are created through a random deposition technique, and their conductive properties studied. The work undertaken within aims to investigate this lower limit of superconductivity, and determine the causes of these non-resistive effects. The percolating systems we examine are inherently more complex than a perfect one-dimensional wire or uniform thin film, due to their intermediate dimensionality.

Chapter 2 examines the existing literature, and along with some background theory covers several phenomena which could be occuring within the films. Chapter 3 goes over the setup of the experiment, the calibration and characterisation of the Pb nanocluster source, and the experiments themselves. Chapter 4 outlines, analyses and discusses the experimental results, and Chapter 5 summarises the findings and suggests further work.

2

Background theory

2.1 Superconductivity

Superconductivity is a phenomenon whereby a material undergoes a phase transition below some critical temperature T_c, with the resistance generally dropping to zero. There are two hallmarks of a superconductor: one is perfect conductivity which means a current can be passed through the superconductor with no voltage drop across it, so none of the applied power is dissipated by the superconductor. The other hallmark is perfect diamagnetism - a superconductor will both exclude a magnetic field from entering it, and expel an existing penetrating magnetic field as it is cooled down from a normal state to a temperature below T_c.

A bulk superconductor generally has zero resistance at low temperatures, though this is not always the case in systems with restricted dimensionality (usually quasi-one-dimensional or quasi-two-dimensional - see Section 2.2 for an overview). As the temperature is increased past T_c the superconductor transitions into a normal state with a finite resistance R_N. Likewise, the perfect conductivity and diamagnetism of a superconductor have finite transition points; an applied current above some critical current I_c, or an applied magnetic field above some critical field strength H_c, will cause superconductivity to break down in the medium.

2.1.1 BCS theory

The Bardeen Cooper Schrieffer (BCS) theory of superconductivity [2] is a microscopic theory of superconductivity. A key idea of the theory is that superconductivity arises

from bound pairs of electrons known as Cooper pairs; such a bound state can form if there is an attractive interaction between the electrons, regardless of the strength of the interaction [3]. Individual electrons are fermions - they have half-integer spin, and must obey the Pauli exclusion principle. However, a bound pair of electrons has integer spin, and behaves much like a boson in that the bound pairs can condense into the ground state (forming a Bose condensate).

It is important to note that the BCS theory puts no restriction on the interaction between the electrons other than it must be an attractive interaction which can be approximated by some negative potential near the Fermi energy; the exact nature of the interaction can be medium-dependent. In classic superconductors, the source of the attractive interaction is a phonon-mediated interaction. An electron traveling through a medium will tend to polarise the region around it by attracting positive ions in the lattice towards it; this slightly more positive region in the medium will in turn attract another electron, which gives rise to an effective attraction between the two electrons. The size of this interaction is dependent on how susceptible to displacement the positive ions in the lattice are, and lattice vibrations are known as phonons. The net interaction between the pair of electrons will be attractive when this phonon-mediated interaction exceeds the repulsive Coulombic potential from the two negative charges.

An important prediction of the BCS theory is the presence of an energy gap associated with superconductivity, $\Delta(T)$. The gap arises from the difference in energy between the ground state of the bound pair Bose condensate, and the free conduction electrons (often referred to as quasiparticles). The superconducting energy gap is predicted to have the form

$$\Delta(T) = \frac{\pi}{e^{\gamma}} k_B T_c \sqrt{1 - \frac{T}{T_c}}, \tag{2.1}$$

where $\gamma \approx 0.577...$ is Euler's constant; so the gap is zero at T_c and increases to a limiting value of $\Delta(0) \approx 1.764 k_B T_c$. The minimum energy required to break apart a Cooper pair to give two electrons is therefore $E_g = 2\Delta(T)$.

The BCS theory is very effective at providing a microscopic description of classical superconductors. It is limited though by the fact that it requires the superconducting energy gap $\Delta(T)$ to have no spatial variation. In addition, BCS theory alone is unable to fully explain more exotic systems, such as high-temperature superconductors.

2.1.2 Ginzburg Landau theory

As outlined in the previous section, the microscopic BCS theory of superconductivity is an accurate theory in well-defined systems, but becomes increasingly intractable as the complexity of the system increases. Often the interest lies in the macroscopic effects that result from spatial inhomogeneity; in these situations, the full power of BCS theory is generally not required to be able to make sense of many effects that emerge from superconductivity.

The Ginzburg Landau (GL) theory [4] is a macroscopic model of superconductivity. The idea underpinning the theory is the introduction of a superconducting order parameter $\psi(\boldsymbol{r})$, a complex function which gives a measure of "how superconducting" the medium is. $\psi(\boldsymbol{r})$ describes the superconducting electrons, and can be though of as the wavefunction of the center-of-mass motion of the Cooper pairs [5]. The standard form for the superconducting order parameter is

$$\psi(\boldsymbol{r}) = |\psi(\boldsymbol{r})|e^{i\varphi(\boldsymbol{r})}, \tag{2.2}$$

where $|\psi(\boldsymbol{r})|^2 \equiv n_s^*$ gives the local density of superconducting carriers, and $\varphi(r)$ is the phase of the order parameter.

Ginzburg and Landau argued that the free energy associated with a superconducting system could be described in terms of $\psi(\boldsymbol{r})$, and from this derived a differential equation for $\psi(\boldsymbol{r})$ in terms of the applied magnetic field,

$$\alpha(T)\psi + \beta|\psi|^2\psi + \frac{1}{2m^*}\left(\frac{\hbar}{i}\nabla - \frac{e^*}{c}\boldsymbol{A}\right)^2\psi = 0, \tag{2.3}$$

where $m^* \approx 2m$ and $e^* = 2e$ are the effective mass and charge of a Cooper pair, and A is the magnetic vector potential. The superconducting current is then given as

$$\boldsymbol{J}_s = \frac{e^*}{m^*}|\psi|^2\left(\hbar\nabla\varphi - \frac{e^*}{c}\boldsymbol{A}\right). \tag{2.4}$$

Equations 2.3 and 2.4 are known as the GL differential equations. $\alpha(T)$ and β are phenomenological parameters, and can be evaluated along with the local density of

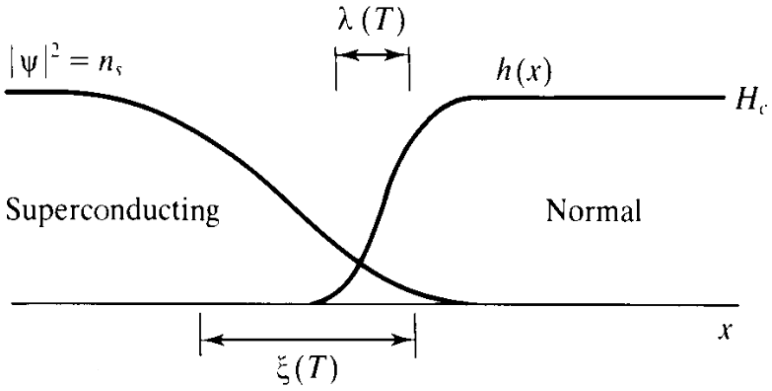

Figure 2.1: Interface between superconducting and normal domains in the intermediate state [5].

superconducting particles n_s^* [5]:

$$\alpha(T) = -\frac{2e^2}{mc^2} H_c^2(T)\lambda_{eff}^2(T) \propto \frac{1-t^2}{1+t^2} \quad \approx (1-t), \tag{2.5}$$

$$\beta(T) = \frac{16\pi e^4}{m^2c^4} H_c^2(T)\lambda_{eff}^4(T) \propto \frac{1}{(1+t^2)^2} \approx const, \tag{2.6}$$

$$n_s^* \equiv \frac{n_s}{2} = \frac{mc^2}{8\pi e^2 \lambda_{eff}^2(T)} \qquad \propto 1-t^4 \quad \approx 4(1-t), \tag{2.7}$$

$$\tag{2.8}$$

where $t \equiv T/T_c$ and $\lambda_{eff}(T)$ is the effective penetration depth of a magnetic field for a superconductor in the bulk. H_c and λ_{eff} can both be determined either through experimental measurement, or direct calculation using BCS theory.

Although the GL theory was originally developed phenomenologically to explain the experimental observations of superconductivity, it was subsequently shown [6] to be a limiting case of the microscopic BCS theory under suitable generalisations for spatial inhomogeneity where $\psi(\boldsymbol{r})$ is directly proportional to the gap parameter $\Delta(r)$ - subject to the restrictions that the temperature be sufficiently close to T_c, and the superconducting gap does not vary too rapidly across the medium.

One of the early successes of the GL theory was in explaining the intermediate state of superconductors, where superconducting and normal regions coexist within a superconductor at an applied magnetic field above H_c. Figure 2.1 depicts a boundary between superconducting and normal domains in the simple one-dimensional case,

showing the interaction between the penetrating magnetic field strength $h(x)$ and the superconducting order parameter ψ. $h(x)$ interacts with the superconducting phase over the characteristic penetration depth λ_{eff}, while ψ interacts with the normal phase over another characteristic length predicted by GL theory - the coherence length, which describes the size of thermodynamic fluctuations within the superconducting state:

$$\xi(T) = \sqrt{\frac{\hbar^2}{2m|\alpha(T)|}}. \tag{2.9}$$

The penetration depth describes the distance that an external magnetic field can penetrate a superconductor:

$$\lambda_{eff}(T) = \sqrt{\frac{m}{4\mu_0 e^2 \psi_0^2}}, \tag{2.10}$$

where ψ_0 is the equilibrium value of the order parameter in zero magnetic field.

The ratio of the penetration depth and the coherence length gives the GL parameter,

$$\kappa = \frac{\lambda_{eff}(T)}{\xi(T)}, \tag{2.11}$$

a dimensionless quantity that is independent of temperature (because both $\lambda_{eff}(T)$ and $\xi(T)$ vary as $(1-t)^{1/2}$ near T_c).

2.1.3 Type-I vs. type-II superconductors

Superconductors can be split into two types, based on the behaviour of the boundary between normal and superconducting regions. The boundary illustrated in Figure 2.1 is for a type-I superconductor, where $\lambda < \xi$. In this regime, there is a positive surface energy associated with boundary walls between normal and superconducting domains [5]. Magnetic fields are excluded from the superconducting region completely, in that the magnetic field strength drops to zero over a small distance from the superconducting boundary. Type-I superconductors have a simple phase diagram, with a single critical field H_c above which superconductivity is destroyed and the magnetic field penetrates the sample.

In type-II superconductors the critical field H_c for a type-I superconductor is replaced by the two critical fields H_{c1} and H_{c2}. Below H_{c1} magnetic fields are completely screened from the interior of the superconductor, as for type-I; above H_{c2} the superconductivity is unable to nucleate and the magnetic field penetrates completely. But

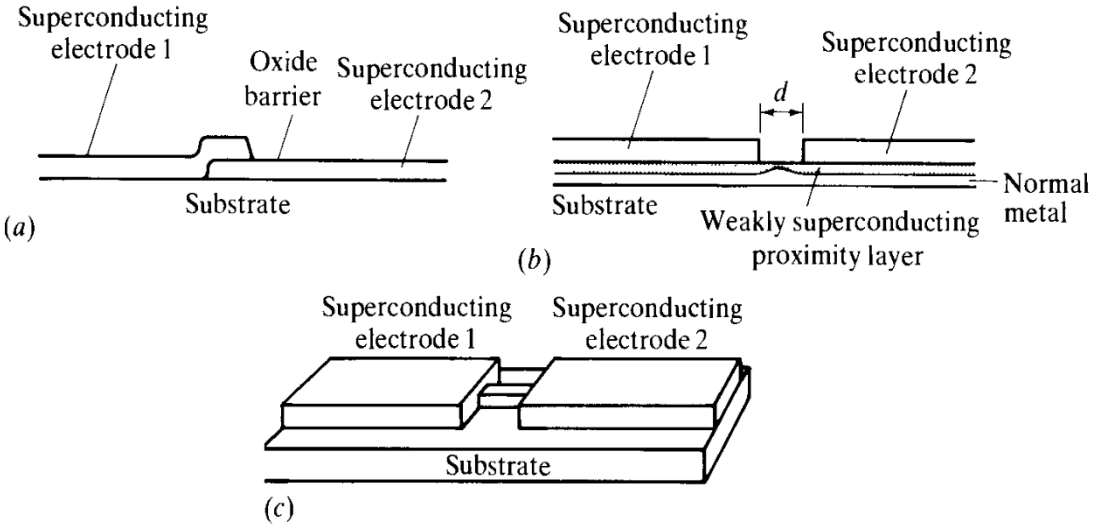

Figure 2.2: Three types of Josephson junction: (a) S-I-S, (b) S-N-S and (c) S-c-S [5].

between H_{c1} and H_{c2} there is a third phase known as the mixed or Schubnikov state, and in this phase the magnetic field can penetrate the superconductor without destroying the superconductivity. This is because a type-II superconductor has $\lambda > \xi$ - in this regime, there is a negative surface energy associated with the superconducting-normal boundary wall, and so the domains will continue to subdivide until they reach a limiting size of ξ. These limiting, quantised domains are known as vortices, and are discussed in more detail in Section 2.7.1.

The breakpoint between the type-I and type-II superconducting regimes occurs at $\kappa = 1/\sqrt{2}$ [7].

2.1.4 Josephson junctions

Josephson junctions are superconducting devices with a rather interesting property - they convert dc voltage into ac current, and although they are not continuous superconductors they support dc superconducting currents with no voltage drop.

A Josephson junction consists of two superconducting regions separated and connected by a "weak link". Figure 2.2 gives examples of various types of Josephson junctions. The original situation considered by Josephson [8] was for two superconducting regions separated by a thin insulating layer (an S-I-S junction), but the weak link can also be a constriction in the superconducting film (an S-c-S junction) or a

normal metal layer which via the proximity effect [5] becomes weakly superconducting (an S-N-S junction).

Josephson made two predictions about the behaviour of these superconducting junctions. Firstly, if the two superconducting regions on either side of the barrier have a phase difference of φ_{12}, then a non-zero dc supercurrent will flow between them given by [8]

$$I_s = I_c \sin \varphi_{12}. \tag{2.12}$$

The important point is that the supercurrent will flow with no potential difference between the two superconducting regions; the two regions have superconducting phase coherence even though there is a barrier between them. This is known as the dc Josephson effect.

Secondly, the relationship between the phase difference between two points in a superconductor and the potential difference applied across them is given by the Josephson relation [8, 9]

$$\frac{d\varphi_{12}}{dt} = \frac{2eV}{\hbar}, \tag{2.13}$$

i.e. the phase difference will steadily increase when a non-zero voltage is applied. From Equation 2.12, this means that if a dc voltage is applied across a Josephson junction, an ac supercurrent will oscillate through it with a frequency $\nu = \frac{2eV}{h}$ and amplitude I_c. This is known as the ac Josephson effect.

Both effects have extensive confirmation in the literature. While the ac Josephson effect is not directly examined in this thesis, the Josephson relation is important in the development of the theory of phase slips (see Section 2.3), and the dc Josephson effect is fundamental to many of the phenomena discussed in the following sections.

2.2 Superresistivity

The previous section provided an overview of superconductivity - in and of itself a fascinating subject. Even more intriguing, however, is a superconducting effect that occurs under certain conditions which results in a resistance increase below the critical temperature; this effect is known as superresistivity.

Superresistivity has been observed by many researchers [10–12]. Figure 2.3 shows a range of $R(T)$ curves observed for various granular films of differing material and

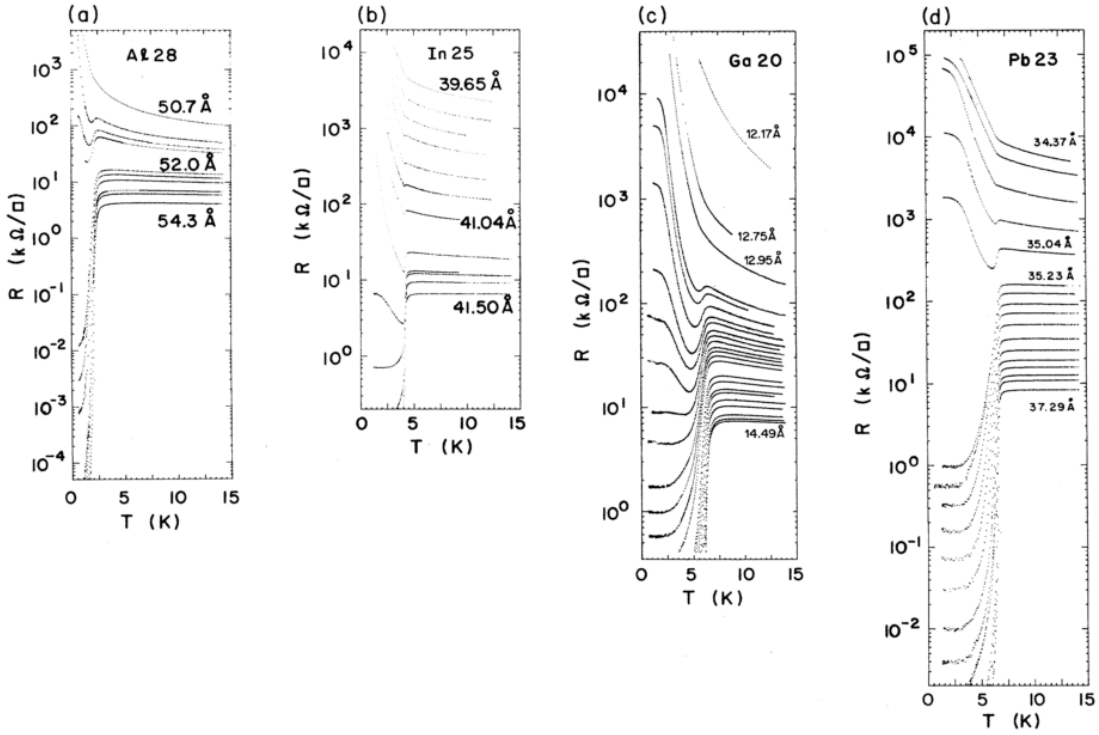

Figure 2.3: The evolution of $R(T)$ curves for (a) Al, (b) In, (c) Ga, and (d) Pb, obtained in situ after successive increments of film thickness. Note that in all cases the entire evolution from insulating to globally superconducting spans an interval of nominal thickness of less than one monolayer. [10]

increasing coverage. Successive curves on a graph were measured between incremental depositions on the sample. These graphs show four distinct regions:

- a globally superconducting region - this is standard superconducting behaviour where the resistance of the film drops to zero below T_c,
- an incomplete superconducting region - the resistance drops below T_c but levels off to a finite value,
- a "quasireentrant" region - the resistance drops below T_c briefly but then rises and (in many samples) eventually levels off, and
- a superinsulating region - below T_c the resistance increases (eventually levelling off in some samples).

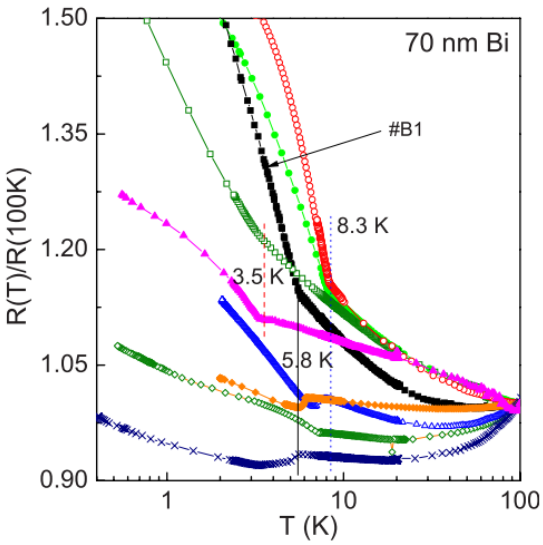

Figure 2.4: R vs T curves of nine granular Bi nanowire samples (d=70 nm, L=6 μm) showing a super-resistive behaviour at a well-defined T_{sr}. [13]

All of these regions transition at the same temperature for a particular element, indicating that superconductivity is either responsible for or contributes to the effects seen. Additionally, the entire range of curves corresponds to only a few monolayers of deposition, implying that the effect is very sensitive to the coverage of the system.

Experiments on superconducting granular Bi nanowires [14] found an increase in resistance below some characteristic temperature (labelled the superresistive temperature, T_{sr}) in over half of the samples studied. Further investigation [13] confirmed these observations. Figure 2.4 shows the $R(T)$ behaviour of the non-superconducting samples. Unlike the thin films considered earlier, the critical temperatures vary significantly between samples; this indicates that the exact value of T_{sr} is very sensitive to the exact growth conditions of the sample.

An explanation for the above behaviour was proposed [10, 13] to be a consequence of there being localised pairing of electrons within individual islands, but no global phase coherence of the superconducting order parameter. Thus the individual islands of clusters go superconducting below T_{sr} and Cooper pairs form within them, but the overall sample becomes more resistive. The superinsulating regions exhibit "strong insulating behaviour and [thermally] activated conductivity" [10], and are thought to

be dominated by tunneling of normal-state quasiparticles between islands [12].

Vinokur and coworkers [15] gave a theoretical treatment of superinsulativity in an array of small superconducting islands linked in a square matrix by Josephson weak links. They investigated a transition dual to the superconducting BKT transition (see Section 2.7.2), and showed that it separates an insulating phase (thermally activated with a finite, if large resistance) and a superinsulating phase (with infinite resistance). The investigators give rise theoretically to the superinsulating phase through the quantum uncertainty principle $\Delta\phi\Delta n \geq 1$, where ϕ is the Josephson phase difference across the junction, and n is the number of Cooper pairs transferred through the junction. Because these two quantities cannot both be known to arbitrary precision, the system can be in either of two states where one of these quantities dominates; hence, the collective phase which is characteristic of a superconductor is the dual of the collective charge of a superinsulator.

Non-zero resistance in the superconducting state has also been observed in ultrathin ($\leq$ 10nm) MoGe nanowires [16] which was attributed to a localisation of Cooper pairs (similar to above) but caused by the presence of Quantum Phase Slips (see Section 2.3.5). It is stated that the nanowires are in an insulating state, but this seems to differ from the superinsulating behaviour observed in the granular films [10, 12]. Common to both experiments is that non-zero resistance is only observed when the normal-state resistance $R_N > R_Q = h/4e^2$ (or the normal-state resistance per square for the granular films).

2.3 Phase slips

Phase slips are processes by which the momentum of the superconducting electrons relaxes in quasi-one-dimensional superconducting wires. They manifest as an "instantaneous" change in the phase difference of the superconducting order parameter by 2π, which decreases the supercurrent and reduces the average velocity of the superconducting pairs. This results in a potential difference across the wire.

2.3.1 Phase in a superconducting wire

In order for a superconducting wire to be quasi-one-dimensional, the order parameter must be stable across the wire; this places a theoretical upper limit on the width or

diameter of the wire of [17, 18]

$$d_{max} = \pi\sqrt{2}\xi(T) \approx 4.44\xi(T), \tag{2.14}$$

where $\xi(T)$ is the coherence length of the superconducting material.

Consider a superconducting wire of length L and diameter $d \ll \xi(T)$. In this configuration it is energetically unfavourable for the superconducting order parameter to vary across the width of the wire and so the wire can be approximated as one-dimensional [19, 20]. The usual one-dimensional solution for the GL equations is [21]

$$\psi(x) = |\psi(x)|e^{i\varphi(x)}, \tag{2.15}$$

where φ is the phase of $\psi(x)$. Note that when a phase difference between two locations is mentioned, the total phase difference $\Delta\varphi$ is implied, not the relative phase difference $\Delta\phi$ between the phases as measured with respect to the Argand plane. Mathematically, $\Delta\phi = \Delta\varphi \mod 2\pi$ - a full traversal of $\psi(x)$ around the Argand plane gives $\Delta\phi = 0$, but $\Delta\varphi = 2\pi$.

The superconducting current in a one-dimensional wire is [22]

$$I_s = \frac{e\hbar}{m}|\psi(x)|^2\frac{\partial\varphi}{\partial x}, \tag{2.16}$$

where I_s is the superconducting current and $\partial\varphi/\partial x$ is the phase gradient, which is $\Delta\varphi/L$ for a constant supercurrent density along the wire. (The effect of magnetic field is not considered and not included in the equation.) I_s is proportional to the gradient of the phase of the order parameter; if the phase difference between the ends of the wire is zero, then there is no supercurrent flowing. Hence, a useful way to imagine the supercurrent is by visualising $\psi(x)$ as being a helix, spiralling through the complex plane along the length of the wire.

Figure 2.5(a) shows one possible configuration for $\psi(x)$ (a "configuration" meaning a particular unique instance of $\psi(x)$ defined both by the phase φ and magnitude $|\psi(x)|$ over the length of the wire). Note that in this instance, the amplitude of $\psi(x)$ is constant along the entire length of the wire. In reality, random thermal fluctuations within the wire will cause variations in the order parameter, giving a wide range of possible configurations for $\psi(x)$ (such as Figure 2.5(b)). The order parameter describes a large number of superconducting pairs, and it is unlikely that any random fluctuation will affect all pairs within a region equally and instantaneously; therefore it makes sense

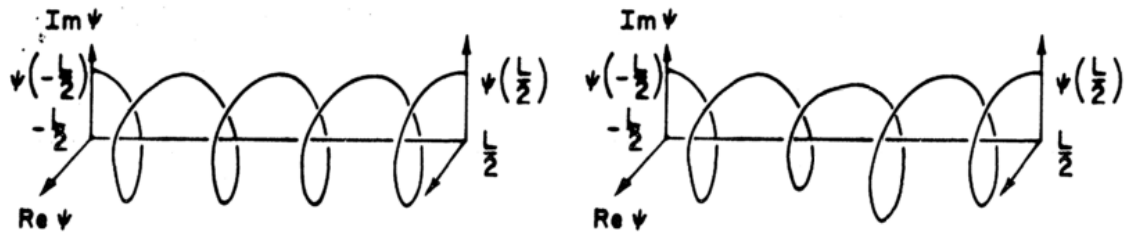

Figure 2.5: (a) The order parameter $\psi(x)$ for a uniform current-carrying state. [17] (b) A non-uniform $\psi(x)$

to consider the variations in the order parameter to be continuous rather than discrete [21].

The relationship between the phase difference between two points in a superconductor and the potential difference is given by the Josephson relation (Equation 2.13 above). Under an applied voltage, the phase difference will steadily increase. From Equation 2.16 this implies that the supercurrent will also increase, as the superconducting electrons are accelerated by the potential - akin to "winding up" the order parameter in Figure 2.5, putting more turns on the helix. Naïvely this would result in the supercurrent increasing to infinity; however, eventually the velocity of the superconducting pairs will exceed the critical velocity v_c corresponding to the critical current I_c and the superconductivity will be destroyed. This is related to the accelerative supercurrent of the London equation $E = \partial(\Lambda \boldsymbol{J}_s)/\partial t$ (as noted in Ref. [5]).

2.3.2 The phase slip process

The phase slip process itself was first proposed by Little [21], who considered a "one-dimensional" superconducting wire with the ends joined together to form a continuous ring. The boundary condition on the order parameter is that it be single-valued, which in such a ring places a periodic restriction on the phase of $\psi(x)$:

$$\Delta\varphi = \varphi(L + x) - \varphi(x) = 2\pi n. \tag{2.17}$$

In terms of the helical graph in Figure 2.5, the ring can hold only an integer number of turns. The different configurations for $\psi(x)$ can therefore be grouped into subensembles by the number of turns, n that they contain. $\psi(x)$ can vary between configurations

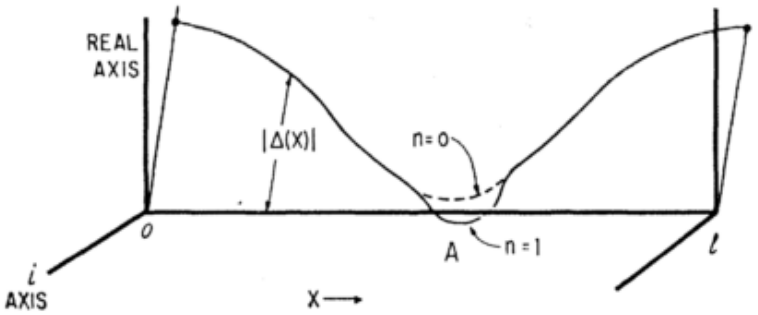

Figure 2.6: The order parameter $\psi(x)$, which is complex, is drawn as a function of position. Two possible configurations are shown, one for an order parameter in the subensemble $n = 0$ and the other for $n = 1$. Near A, $\psi_1(x)$ makes an excursion round the Argand diagram while $\psi_0(x)$ does not. [21]

within a subensemble depending on the size of the random fluctuations, but it is topologically impossible for $\psi(x)$ to transition from one subensemble to another without the order parameter being driven to zero at some point [21]. This topological restriction is the same as, for example, attempting to add or remove twists on a Möbius strip - it is possible to deform the paper ring continuously, but to actually change the number of twists the ring must be cut open, twisted and then glued back together. Similarly, the different configurations of $\psi(x)$ within a subensemble are homeomorphic (can be deformed continuously from one to another), but the different subensembles are not.

The process of transitioning between subensembles of $\psi(x)$ is what constitutes a phase slip - a random fluctuation occurs which drives the order parameter at some point in the wire to zero, momentarily breaking the phase coherence and making a small region of the superconductor normal. The phase of $\psi(x)$ at that point is then free to "slip" by an integer multiple of 2π, before the order parameter then recovers to a non-zero value.

Figure 2.6 gives an example of this process, showing two different configurations for $\psi(x)$ from neighbouring subensembles. At the point A, both $\psi_1(x)$ and $\psi_0(x)$ are suppressed close to zero. However, there is a significant difference between them: $\psi_0(x)$ has zero net phase difference, and so zero net supercurrent, whereas $\psi_1(x)$ circles around the Argand plane, and thus has a total phase difference of 2π and corresponds to a non-zero supercurrent. Since $\psi(x)$ must vary continuously, a transition from $\psi_1(x)$ to $\psi_0(x)$ (or vice-versa) must pass through $\psi(x) = 0$.

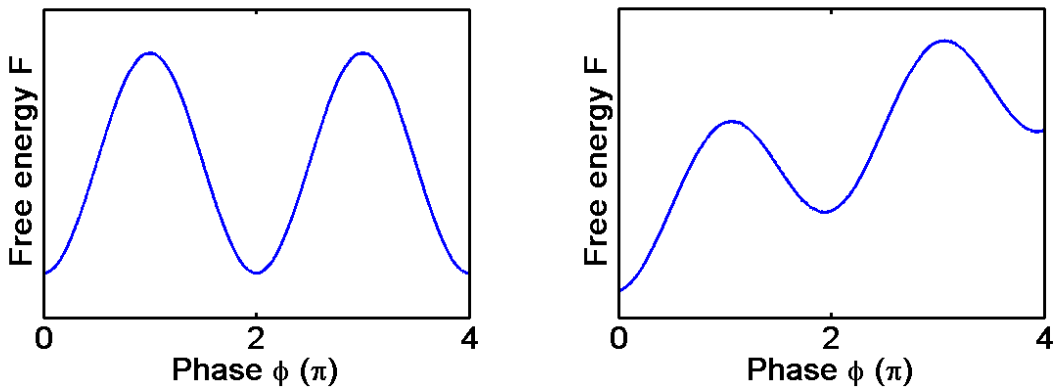

Figure 2.7: Free energy potential wells (a) at zero voltage bias and (b) at non-zero voltage bias.

This transition between subensembles has some energy barrier $\Delta F(T)$, corresponding to the condensation energy required to suppress the order parameter to zero within some small region. Local energy fluctuations below the energy of the barrier will change the order parameter but keep the same overall configuration, while larger fluctuations will lead to phase slips. Because the source of energy is thermal fluctuations, such events are known as TAPSs. The length of the suppressed region is on the order of the coherence length $\xi(T)$; such a length minimizes both the gradient and amplitude of the condensate free energy, resulting in the lowest energy barrier [23].

Figure 2.7(a) shows $\Delta F(T)$ as a function of the phase difference φ (Figure 2.7(b) is discussed in the next section). A phase slip occurs when a thermal fluctuation causes the order parameter to surpass the energy barrier and move into an adjacent energy minimum. There is equal probability of a phase slip decreasing the phase as there is of increasing it, because there is an equal energy barrier for either direction. The latter is often referred to as an anti-phase slip, because it acts to increase the supercurrent.

Little [21] modeled the phase slip process with an Arrhenius-type equation for the resistance of the superconducting wire,

$$R_{Little}(T) = R_N \exp\left[-\frac{\Delta F(T)}{k_B T}\right], \tag{2.18}$$

where R_N is the normal-state resistance, and $\Delta F(T)$ is the free energy barrier for phase slips described above. This model becomes unrealistic at temperatures close to

T_c because $R_{Little}(T_c) = R_N$ whereas generally the resistance at T_c should be less than the normal-state resistance due to superconducting fluctuations [22].

2.3.3 The LAMH model of TAPSs

The LAMH theory [17, 24] generalises the argument in Ref. [21] from a one-dimensional superconducting ring (described above) to the superconducting wire considered in Section 2.3.1. The phase difference is no longer constrained to be an integer multiple of 2π (as it was in the superconducting ring due to boundary conditions), but can vary continuously between the ends of the wire. This is the situation discussed at the end of Section 2.3.1, where an applied voltage can destroy the superconductivity within the wire.

The LAMH model centres around two main ideas:

- A steady current through a superconductor under an applied voltage is possible if fluctuations within the superconductor stochastically reduce the phase difference between its ends at the same average rate as the voltage increases it.

- The fluctuations can be represented as continuous random motion of the superconducting order parameter $\psi(x)$ through a continuous function space of states (as described in Section 2.3.2), and these states are solutions of the GL equations.

Phase slips do not result in a constant rate of change of phase, because each random phase slip event is a discrete 2π jump; instead, there is an average rate of occurrence of phase slips, which in turn gives an average rate of change of the phase of the order parameter. As described in Section 2.3.2, with zero applied voltage there is equal probability of a phase slip decreasing the phase as there is of increasing it (Figure 2.7(a)). Therefore the two processes have equal average rates, and so the net average rate of phase slips is zero.

However, with an applied voltage the rates of phase slips and anti-phase slips will begin to differ, because the energy barriers for phase slips in the two directions have some difference $\delta F = \Delta F(T)_f - \Delta F(T)_r$ (Figure 2.7(b)). The origin of this difference is in the electrical work done along the wire [25]. The net average frequency of phase slips is therefore given by the difference between the average rate of phase slips and the average rate of anti-phase slips. With each phase slip contributing a reduction

of 2π to the phase, it is clear from Equation 2.13 that in order to maintain a steady phase difference between the ends of the wire (and hence a steady current through the superconducting wire), the average frequency of phase slips must be $2eV/h$.

The LAMH model gives a different form for the resistance of the superconducting wire to the Little model:

$$R_{LAMH}(T) = R_Q \left(\frac{\hbar\Omega(T)}{k_B T}\right) \exp\left[-\frac{\Delta F(T)}{k_B T}\right], \tag{2.19}$$

with

$$\Delta F(T) = V_{PS}\left(\frac{H_c^2}{8\pi}\right) \tag{2.20}$$

$$= \frac{8\sqrt{2}}{3} A\xi(T)\left(\frac{H_c^2}{8\pi}\right), \tag{2.21}$$

where $R_Q = h/4e^2$ is the quantum resistance, $V_{PS} \approx 3.77\xi(T)A$ is the effective volume of the phase slip, A is the cross-sectional area of the wire at the location of the phase slip, and H_c is the temperature-dependent thermodynamic critical field.

$\Omega(T)$ is the attempt frequency; it is related to the rate at which fluctuations in the order parameter occur, and is only weakly sensitive to $T_c - T$ and to the current in the wire [24]. It was initially proposed to be [17]

$$\Omega(T) = N_e/\tau_e, \tag{2.22}$$

where N_e is the number of conduction electrons and $\tau_e \approx 10^{-12}$s is a normal-state electron scattering time; this was chosen rather arbitrarily as a rough estimate of the rate at which $\psi(x)$ changes. McCumber and Halperin [24] used a time-dependent GL equation to re-estimate $\Omega(T)$, finding an equation of the form $\Omega(T) = N(T)/\tau(T)$, where $N(T)$ is the number of statistically independent subsystems along the wire, and $\tau(T)$ is a microscopic diffusion time. The full equation for $\Omega(T)$ is

$$\Omega(T) = \frac{L}{\xi(T)}\frac{1}{\tau_{GL}}\sqrt{\frac{\Delta F(T)}{k_B T}}, \tag{2.23}$$

where (L/ξ) is the length of the wire in units of the coherence length, and $\tau_{GL} = (\pi\hbar)/(8k_B\Delta T)$ is the relaxation time in the GL equation ($\Delta T \equiv (T_c - T)$). (L/ξ) gives an estimate of the number of independent locations at which phase slips can occur along the wire, since each phase slip requires the order parameter to be suppressed

over about a coherence length. This estimate for $\Omega(T)$ is smaller than the original estimate of Equation 2.22 by a factor $N_\xi \equiv N_e/N(T)$, which is approximately the number of conduction electrons in a length $\xi(T)$ of the wire. For the geometry of the superconducting whisker-crystal wires studied by Webb and Warburton [26], $N_\xi \geq 10^{10}$.

It is important to note that near T_c, $H_c \propto \Delta T$ and $\xi(T) \propto (\Delta T)^{-1/2}$. Using these, $\Delta F(T)$ can be expanded from Equation 2.21 to give

$$\Delta F(T) = \frac{8\sqrt{2}}{3} A\xi(0) \left(\frac{H_c^2(0)}{8\pi}\right) \left(1 - \frac{T}{T_c}\right)^{3/2}. \tag{2.24}$$

Hence the LAMH theory cannot be applied very close to T_c, because $\Delta F(T)$ goes to zero as $(\Delta T)^{3/2}$, and thus so does $R_{LAMH}(T)$.

While the derivation [24] of Equation 2.23 above is sound, the time-dependent GL formulation used to obtain it is known to suffer from serious drawbacks [27], and in general is not applicable much below T_c. Ref. [28] derives the pre-exponential factor using a more solid microscopic effective action formulation. The resistance contribution from the resulting Golubev Zaikin (GZ) model is

$$R_{GZ}(T) = \frac{4\pi\sqrt{6\pi}}{e^2} \frac{aT_c}{T} \frac{L}{\xi(T)} \sqrt{\frac{\Delta F(T)_{GZ}}{T}} \exp\left[-\frac{\Delta F(T)_{GZ}}{T}\right], \tag{2.25}$$

where $a = T^*/T_c$ defines the effective crossover temperature between TAPS and QPS (see Section 2.3.5), and

$$\Delta F(T)_{GZ} = \frac{16\pi^2}{21\zeta(3)} s N_0 \sqrt{\pi D} (T_c - T)^{3/2} \tag{2.26}$$

($\zeta(3) \approx 1.2$) turns out to be exactly equal to the magnitude of $\Delta F(T)$ for the LAMH model in the limit of small transport currents [28].

So far only $R(T)$ relationships have been considered for determining the presence of phase slips in a sample, because the resistance caused by TAPSs is strongly dependent on temperature. However, it is still possible to extract some evidence of phase slips from $V(I)$ data. For small bias currents at temperatures slightly below T_c, the $V(I)$ curve is given by [27, 30]

$$V = \frac{\hbar\Omega(T)}{e} \exp\left[-\frac{\Delta F(T)}{k_B T}\right] \sinh(I/I_0), \tag{2.27}$$

where $I_0 = 4ek_BT/h$. Differentiating this with respect to the bias current gives

$$\frac{dV}{dI} = \frac{\hbar\Omega(T)}{eI_0} \exp\left[-\frac{\Delta F(T)}{k_B T}\right] \cosh(I/I_0), \tag{2.28}$$

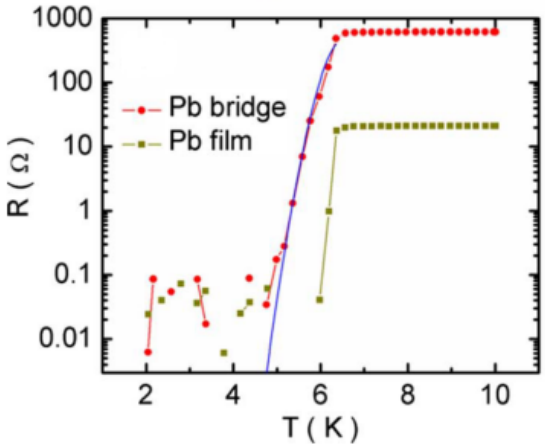

Figure 2.8: R(T) curves for a Pb nanobridge measured both across the nanobridge and across a nearby region of unconstricted two-dimensional film. The solid blue curve is a fitting of the LAMH model near T_c [29].

which can be written in the form $dV/dI = R(T)\cosh(I/I_0)$. Therefore, by fitting this equation to dV/dI vs I curves at different temperatures, the resistance at zero bias current can be extrapolated, and then fitted to the $R(T)$ equation for the TAPS model.

2.3.4 TAPSs in experiments

As mentioned above, phase slips create a resistance stochastically - randomly-occuring phase slips make up a "background noise" resistance. As such, it is not expected that individual jumps or steps in resistance would be observed corresponding to individual phase slips, but rather an average resistance corresponding to the time-averaged sum of the ongoing slips. This agrees with what has been observed in the literature - a broadening of the superconducting transition, such as in Figure 2.8.

TAPSs have been used to explain observations of resistance as a function of temperatures in a variety of samples, such as superconducting whisker-crystal wires [26, 31], quasi-1D nanowires [32–34] and nanobridges [29, 30]. The LAMH model has provided good fits to many experiments [29, 32, 33] (eg. Figure 2.8), despite the fact that, strictly, it is only applicable in a narrow temperature window. The size of this window is somewhat disputed, with some experiments showing poor LAMH fits below $0.9T_c$ [35, 36], while others have found that LAMH fits well down to $0.65T_c$ [31].

The equations for the resistance of a quasi-one-dimensional wire given in the sections above cannot be directly fitted to experimental data, because the free energy barrier term $\Delta F(T)$ is non-linear. There are several different possible (equivalent) expressions for the free energy barrier:

$$\Delta F(T) = \frac{8\sqrt{2}}{3} A\xi(0) \left(\frac{H_c^2(0)}{8\pi}\right) \left(1 - \frac{T}{T_c}\right)^{3/2}, \tag{2.29}$$

$$\Delta F(T) = 0.83 k_B T_c \frac{R_Q}{R_N} \frac{L}{\xi(0)} \left(1 - \frac{T}{T_c}\right)^{3/2}, \tag{2.30}$$

$$\Delta F(T) = \sqrt{6} \frac{\hbar}{2e} I_c(T). \tag{2.31}$$

Equation 2.29 is the free energy barrier found by LAMH [17] (Equation 2.24 above). Equation 2.30 is an alternative formulation [37] which uses T_c and $\xi(0)$ as fitting parameters, leaving R_N and L to be directly measured. Equation 2.31 (also derived from Equation 2.29) [37] takes a different approach, parameterising $\Delta F(T)$ in terms of the critical current I_c instead of the coherence length.

Equation 2.14 earlier gave the upper limit on quasi-one-dimensionality of a wire to be $d_{max} \approx 4.44\xi(T)$. In many of the experiments for which TAPS fits are found [29, 30, 34] the transverse dimensions of the superconducting wires exceed $\xi(T)$ (the limit in which the Little and LAMH models were formulated), but remain within the bound d_{max}.

Additionally, there is experimental evidence that the LAMH model is only applicable for wires above a given size. Zgirski and coworkers [33] used Ar^+ ion sputtering to gradually reduce the effective cross-section σ of Al nanowires and observed a reasonable fit to LAMH for wires with a smallest transverse dimension $\sqrt{\sigma} \geq 15$nm. Below this, the $R(T)$ curve developed a "resistive tail" at lower temperatures which is inconsistent with any TAPS model, and was attributed to QPSs (see Section 2.3.5).

In recent years, the Little model has made a resurgence for several reasons. Bae and coworkers [34] used the Little model for proving the presence of TAPS in MoGe and Al nanowires due to the narrow temperature window that the LAMH model is applicable in [36]. On the other hand, the LAMH model was used in Ref. [30], which examined short, wide constrictions ($\sim$ 100nm long and a few times wider than the coherence length) in MoGe films and observed both a transition attributed to the BKT phase transition (see Section 2.7.2) in the adjacent 2D thin film, and a TAPS effect localised

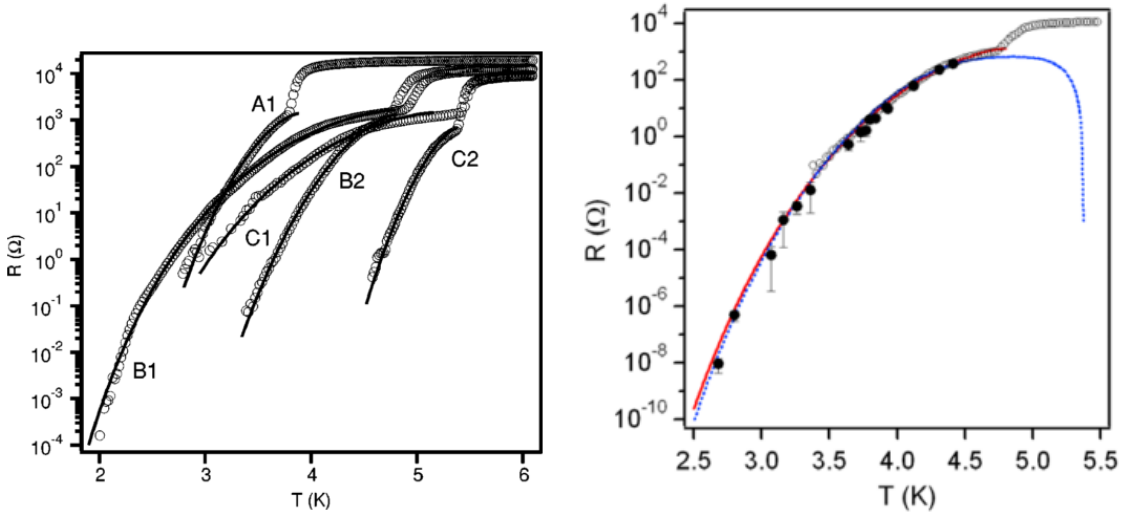

Figure 2.9: (a) Low-bias resistance for five different samples with bridges. Solid lines are fits to the "bridge" (Little) phase slip model [30]. (b) $R(T)$ for sample B2. The solid (red) and dashed (blue) curves give the best fits generated by the Little (equation 2.18) and LAMH (equation 2.19) formulae respectively [22].

in the bridge (Figure 2.9(a)). To accomodate the 2D geometry of the bridge within the LAMH model, the pre-exponential factor of Equation 2.19 was modified, resulting in the same equation (2.18) as for the Little model. Figure 2.9(b) shows fits of both the LAMH model and the Little model, with the latter giving a better fit.

In the previous section it was mentioned that $V(I)$ data could be used to determine the presence of phase slips in a sample by fitting the equation $dV/dI = R(T)\cosh(I/I_0)$ to dV/dI vs I curves at different temperatures, and extrapolating the resistance at zero bias current to be fitted to the $R(T)$ equation for the TAPS model. The filled boxes in Figure 2.9(b) were obtained by this method, and correspond well to the directly-measured data (open circles).

One can note that a single phase slip event is analogous to the normal core of an isolated vortex crossing the wire perpendicular to the direction of current flow, because both have the condition that $\psi(x) = 0$ be satisfied at some point [22]. For a discussion of vortices, see Section 2.7.

2.3.5 Quantum Phase Slips

The TAPS mechanism described above is driven by thermal fluctuations in the superconducting wire which provide the energy required to surpass the free energy barrier and transition from one subensemble to another. However, there is another way to circumvent this energy barrier - by quantum-mechanically tunneling through it. Phase slips resulting from this process are known as Quantum Phase Slips (QPSs).

Giordano's model of QPSs [38] suggests that at low temperatures there is a contribution to the resistance of the superconducting wire from Macroscopic Quantum Tunneling (MQT) of the order parameter through the free energy barrier. While at the time no quantitative model of MQT for one-dimensional superconductors existed, the general theory of MQT had been well-established in other systems. Beginning from the general MQT tunneling rate

$$\Gamma_{MQT} = A' \exp\left(-B'/\hbar\right) \tag{2.32}$$

(where A' and B' are general parameters), an expression for the resistance due to one-dimensional MQT can be derived. However, a heuristic argument shows that the resulting equation for the resistance is equivalent to replacing the thermal temperature fluctuation energy scale $k_B T$ in the LAMH model with the quantum energy fluctuation scale $k_B T_Q = \hbar/\tau_{GL} = (8/\pi)k_B(T - T_c)$. Thus the contribution to the resistance of the superconducting wire from the Giordano-model of QPS can be given as

$$R_G(T) = BR_Q \left(\frac{\hbar\Omega_G(T)}{k_B T_Q}\right) \exp\left[-\frac{a\Delta F(T)}{k_B T_Q}\right], \tag{2.33}$$

where B and a are extra adjustable parameters of order unity (from general MQT theory), and

$$\Omega_G(T) = \frac{L}{\xi(T)} \left(\frac{k_B T_Q}{\hbar}\right) \sqrt{\frac{\Delta F(T)}{k_B T_Q}} \tag{2.34}$$

is the quantum attempt frequency. The energy barrier $\Delta F(T)$ is just Equation 2.21. The resistance contributions from TAPS and QPS are added in series, since both mechanisms contribute to the total rate of phase slip events. Considering effects from both TAPS and QPS, the overall resistance of a one-dimensional superconducting wire can be expressed as [5]

$$R^{-1} = \left(R_{LAMH}(T) + R_G(T)\right)^{-1} + R_N^{-1}. \tag{2.35}$$

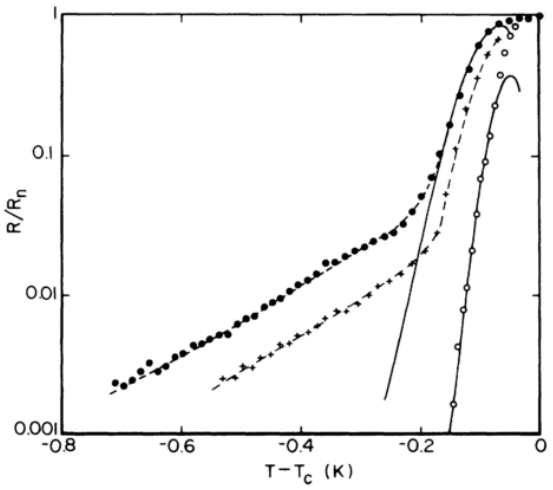

Figure 2.10: Resistance, normalised by the normal state value, as a function of temperature for three In wires. The solid curves are fits to the LAMH model (Equation 2.19), while the dashed curves are fits to Equation 2.35 [38].

R_N is the parallel conduction path through the normal conducting electrons.

As described in Section 2.3.3, TAPSs result in a broadening of the superconducting transition, because the rate of phase slips is dependent on the temperature and drops off rapidly as the temperature decreases. On the other hand, QPSs are used to explain "resistive tails" where the measured resistance of the wire does not go entirely to zero as $T \to 0$, or where there is resistance above what would be expected from TAPSs alone.

Figure 2.10 shows data taken from observations of thin In and PbIn wires [38], with both a pure LAMH fit and a fit combining TAPSs with the Giordano QPS model. The additional contribution from QPSs clearly accounts for the tails in the narrower wires which the TAPS model does not explain. However, it is emphasised in Ref. [38] that this is not conclusive proof of QPSs, and that the results are only consistent with a QPS model; other mechanisms could be causing the effect. Subsequent literature also makes this point. The resistive tail associated with QPSs is generally only observed in very narrow samples, and as such it has been proposed that weak links due to the granularity of the samples could be causing the effect (arising from isolated granular islands, similar to the explanation given for the superresistive effects outlined in Section 2.2); no consensus has been reached as yet.

The Giordano model predicts a higher rate of QPS compared to the TAPS rate at temperatures below $T^* = 0.718T_c$ [39]. This agrees with recent observations by Altomare [40]. Fits to $R(T)$ data from homogeneous, nongranular MoGe wires [41] have indicated that QPS is dominant at $T \sim 0.3T_c$, where TAPS is expected to be exponentially suppressed (as per equation 2.19); similar fits to $R(T)$ data from long Al nanowires [40] indicate QPS dominance below $0.5T_c$.

2.3.6 Alternative QPS models

The Giordano model provides a decent qualitative explanation of QPSs and has been the standard model of QPSs for several decades. However, the fact that it is based on a purely qualitative form of one-dimentional MQT means that its accuracy is limited. In recent years, several alternative theoretical models have been proposed which aim to give a more quantitative explanation of QPSs.

The GZQPS model [42] is a detailed microscopic quantum mechanical theory of QPSs. It focuses on relatively short wires, motivated in part by observations on short (0.1-0.2 μm), narrow (3-5nm) uniform MoGe nanowires [16]. The Golubev-Zaikin-model QPS contribution to the resistance of a superconducting wire is

$$R_{GZQPS}(T) = BR_Q S_{QPS}(T) \frac{L}{\xi(T)} \exp[-S_{QPS}(T)], \tag{2.36}$$

where

$$S_{QPS}(T) = A \frac{R_Q}{R_N} \frac{L}{\xi(T)} \tag{2.37}$$

is the effective action and B and A are adjustable parameters.

The KQPS model [43] was developed by considering vortex tunneling across a very narrow (a few tens of nanometers) thin film. In this regime the vortex tunnels the entire width of the film, and is similar to QPSs in a genuinely one-dimensional wire. This model predicts that even in the QPS regime the resistance can drop sharply as the temperature decreases (akin to TAPS), and is valid when the QPS rate is low [34].

A key difference between KQPS and earlier models is in the energy barrier to the phase slip event. Earlier QPS models considered quantum tunneling through the thermally-activated free energy barrier from the LAMH theory, which is the energy required to suppress the order parameter over a region of the coherence length and create a phase slip core (as discussed in Section 2.3.2). The activation energy for KQPS,

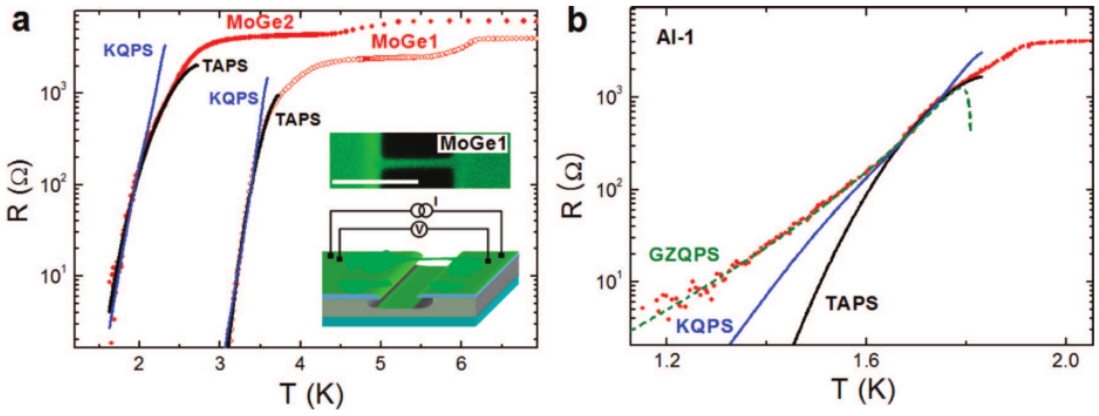

Figure 2.11: (a) $R(T)$ curves of two $Mo_{76}Ge_{24}$ nanowires. The solid black line on each $R(T)$ curve is the best fit produced by the Little-model (Equation 2.18) using the fitting parameters T_c, L and σ. The solid blue lines are obtained from the KQPS model (Equation 2.38). (b) $R(T)$ curve of an Al nanowire. The dashed green curve is the prediction of the GZQPS model (Equation 2.36) using the fitting parameters T_c, R_N, L, B and A. The solid black and solid blue lines are the same as in (a). [34]

on the other hand, is just that of the initial tunneling state, which is considerably lower in energy.

The Khlebnikov-model QPS resistance contribution is

$$R_{KQPS}(T) = R_N \exp\left[-\frac{\pi^2 R_Q \Delta(T)}{4R_N T}\tanh\left(\frac{\Delta(T)}{2T}\right)\right], \tag{2.38}$$

where $\Delta(T)$ is the BCS superconducting energy gap.

Specific experimental evidence for either of the above models is lacking, which is not entirely surprising given they are relatively recent. Ref. [42] used the GZQPS model to estimate typical average times within which one QPS event occurred, for ultrathin uniform MoGe nanowires studied in Ref. [16]. The typical QPS time

$$t_0 = \frac{\xi(T)}{XAS_0\Delta}\exp(AS_0) \tag{2.39}$$

is estimated for two values of A (to which it is very sensitive), but only qualitative interpretations are given for the resulting values rather than verification of the model.

Both GZQPS and KQPS were tested alongside the Little-model for TAPSs on MoGe and Al nanowires [34]. Figure 2.11 shows the resulting fits to the $R(T)$ curves. The Little model fits closest to the MoGe wire data; however, the quality of the KQPS

model fit suggests that QPSs could be the cause of resistance near T_c rather than TAPS, or potentially a thermally-assisted QPS process (a possibility also supported by fits in Ref. [36]). The GZQPS model clearly provides the best fit for the Al nanowires, implying that the resistive tail there is QPS-dominated. Interestingly, the Al wires examined have a dimater of 20-25nm, which is above the threshold determined in Ref. [33] between QPS and TAPS dominance of 15nm (mentioned in Section 2.3.4). This is interpreted by Ref. [34] to mean that the resistive tail is likely caused by a narrow spot in the Al wires acting as a weak link, increasing the probability of phase slips.

2.4 Phase slip centres

A phase slip is itself a time-dependent, transient process - once the order parameter has changed configuration and the phase has changed by 2π, the phase slip region becomes superconducting again. As discussed in Section 2.3.3, this means that the general evidence for phase slips is a non-zero, smooth (on average) resistance as a function of temperature. However, this is not always the case. Under certain circumstances it is possible to get oscillations of the order parameter at a given location, resulting in regular repeated phase slips. Such a location is known as a PSC.

2.4.1 Activation of a PSC

In a perfect, defect-less superconducting wire, the wire switches from the superconducting state to the normal state when the critical current is surpassed (the GL depairing current density). Realistically, however, the wire is not completely homogeneous; defects and constrictions in the wire will mean that I_c is not uniform through the wire, but has a minimum at some location. Therefore, as the bias current I through the superconducting wire is raised, the superconducting current I_s will eventually exceed the local critical current. This causes the local superconducting order parameter $\psi(x)$ to collapse, destroying superconductivity within some region and causing the entire bias current to be carried as a normal current I_n. However, this in turn causes I_s to drop back below I_c to zero, which allows $\psi(x)$ to reform. I_s then increases again until it exceeds I_c, repeating the cycle.

Figure 2.12 shows this time-evolution of I_s in the centre of an active PSC. The supercurrent oscillates between zero and I_c, with an average value of approximately half

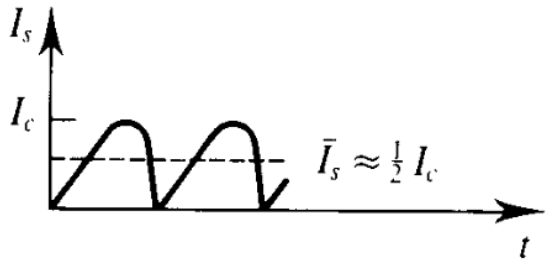

Figure 2.12: The oscillatory supercurrent in the core of the PSC, with average value $\approx I_c/2$ [5].

the critical current. The following sections give a more definite range for the average, and explain the effect that the PSC has on the resistance of the wire.

2.4.2 The SBT model of PSCs

The SBT model of PSCs [44] is a phenomenological model developed to explain the presence of steps in V(I) curves near T_c of long superconducting microbridges. The idea behind it is that each step which occurs as the bias current is increased corresponds to the appearance of a localised resistance centre across which there is a discontinuous jump in the time-averaged electrochemical potential of the superconducting pairs, $\bar{\mu}_s$.

The SBT model starts by assuming negligible departures from electrical neutrality, so that the applied current density $J = J_s + J_n$, the sum of the superconducting and normal current densities. The superconducting current density is

$$J_s = \frac{2e\hbar}{m^*}|\psi(x)|^2 q, \tag{2.40}$$

where $\psi(x) = |\psi(x)|e^{i\varphi(x)}$ and $q(x) = d\varphi/dx$. The normal current density is

$$J_n = -\frac{1}{e\rho}\frac{d\mu_n}{dx}, \tag{2.41}$$

where $\rho \approx \rho_n$ (the normal resistivity) and μ_n is the electrochemical potential of the normal electrons.

When $J_s(x) > J_c(x)$, the superconducting order parameter becomes unstable and $|\psi(x)|^2 \to 0$. As mentioned in Section 2.3.2, the suppression of the order parameter occurs quickest over a localized length $\xi(T)$, with $|\psi(x)|$ driven to zero at a point. At this point, the superconductivity is completely suppressed, and the entire current must

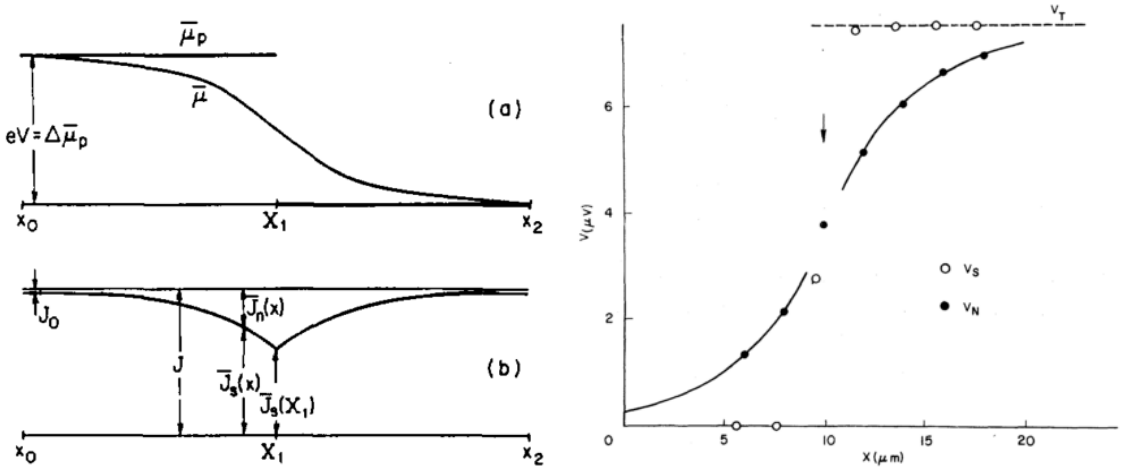

Figure 2.13: (a) (b) Time averages of (a) electrochemical potentials and (b) currents for a single PSC at X_1 ($\bar{\mu_p} \equiv \bar{\mu}_s$, $\bar{\mu} \equiv \bar{\mu}_n$) [44]. (c) Spatial variation of the quantities $V_s = \bar{\mu}_s/e$ and $V_n = \bar{\mu}_n/e$ near a phase-slip centre (arrow) in a tin strip [45].

be carried as a normal current. Thus the superconducting current is now well below the critical current, and the order parameter becomes unsuppressed. Superconductivity nucleates most readily if $q \approx 0$ locally [44].

The oscillation of $\psi(x)$ is driven by oscillations of μ_s, the electrochemical potential of the superconducting pairs. The Josephson relation $\hbar\partial\varphi/\partial t = -2\mu_s$ requires that for a cyclic steady-state situation, the time average of μ_s ($\bar{\mu}_s$) must be constant along the wire between points where phase coherence is lost (i.e. the PSC cores). Conversely, $\bar{\mu}_n$ (the time average of μ_n) must have some gradient in order to drive the normal current through the centre of the PSC (as per Equation 2.41). This is shown in Figure 2.13(a).

The different spatial variations of $\bar{\mu}_s$ and $\bar{\mu}_n$ have been confirmed experimentally by Dolan and Jackel [45]. Figure 2.13(c) shows both the superconducting potential V_s and the normal potential V_n measured at different locations through a PSC in a tin film strip.

2.4.3 Resistance of a PSC

As mentioned in the previous section, the superconducting current through the core of the PSC oscillates with time over a region of about the coherence length $\xi(T)$ - the region where the phase slips occur. The periodic phase slips create an imbalance

of normal electrons (non-equilibrium quasiparticles) in the PSC, and it takes time for these normal electrons to "dissipate" and become superconducting again [5]. The distance over which the normal electrons can diffuse before re-pairing is given by the quasiparticle diffusion length [44]

$$\Lambda \sim \sqrt{l l_2}, \tag{2.42}$$

where l is the ordinary mean free path and $l_2 = v_F \tau_2$ is the mean free path for inelastic scattering. Hence, within a region of 2Λ surrounding the core of the PSC the supercurrent is partially suppressed, and the remainder of the bias current is carried through the PSC as a normal current (see Figure 2.13(b)). Usually $\Lambda \gg \xi(T)$, meaning that while there are time-dependent processes within the PSC core, the overall conductive behaviour of the PSC region can be considered as a time-independent process. The average superconducting current through the PSC can be given as $I_s = \beta I_c$ where $0.5 \leq \beta \leq 0.65$ [44], giving a normal current through the PSC of

$$I_n = I - I_s = I - \beta I_c. \tag{2.43}$$

So the contribution to the differential resistance of the wire from the PSC is simply the normal resistance of a wire of resistivity ρ, cross-sectional area A and length 2Λ:

$$\frac{dV}{dI} = \frac{2\Lambda\rho}{A}. \tag{2.44}$$

Since the requirement for creation of a PSC is that the supercurrent (not the bias current) exceeds the critical current, there is a limit placed on how close two PSCs may be. Once a PSC develops at one location along the wire, the suppressed supercurrent within the region 2Λ around it makes the development of a second PSC within that region unlikely. In this way, the PSCs will tend to space themselves out along the wire. Hence the quantity $(L/2\Lambda)$ gives an estimate of the number of independent locations that PSCs can occur along the wire (c.f. (L/ξ) for phase slips). Theoretical calculations have shown that in a completely uniform filament, steps appear with increasing bias current such that there occur about $(L/2\Lambda)$ steps between I_c and $2I_c$ [46]. Inhomogeneity is therefore not a requirement of PSC formation; nevertheless, realistic wires do contain defects, and these remain the most likely formation points for PSCs.

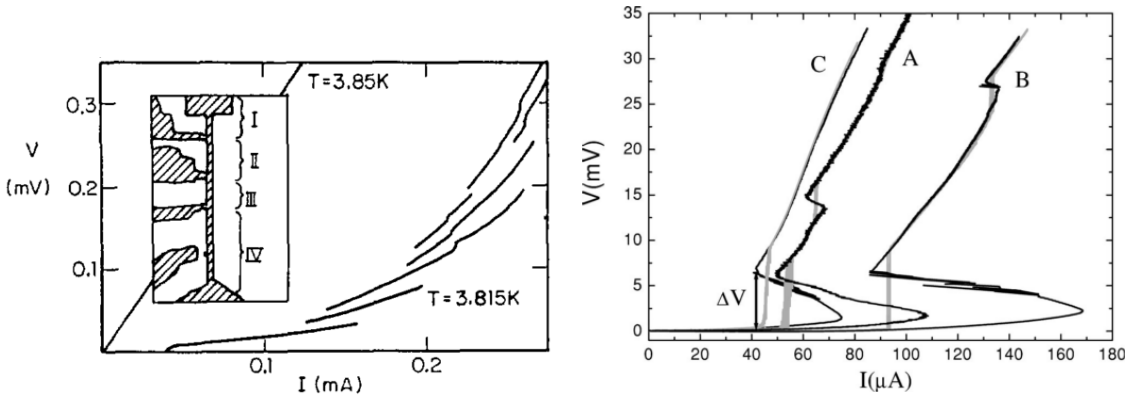

Figure 2.14: (a) Total voltage vs. current at fixed temperature. Inset shows voltage leads for localised voltage measurements along the 4μm by 140μm bridge. [44] (b) Current-voltage characteristics of three samples in the current (grey curves) and voltage (black curves) driven regimes. The low current residual voltage was subtracted from the experimental data. [48]

2.4.4 Observations

As discussed in Section 2.4.3, a PSC contributes a finite resistance to a superconducting wire. However, the PSC only comes into existence when the superconducting current exceeds the local critical current, and so below this current, there is no contribution to the overall resistance. Therefore, the presence of PSCs in a sample can be deduced from the observation of voltage steps in the V(I) data. Each step corresponds to a specific PSC becoming active as the bias current exceeds the local critical current of the superconducting wire. Experiments on tin microbridges [44], tin whisker crystals [47] and Pb nanowires [48, 49] have confirmed this behaviour.

Figure 2.14(a) shows $V(I)$ data from the tin microbridges [44]. The inset of the figure shows the sample geometry used to measure the data; the multiple-lead configuration enabled measurements to prove that the various steps in the $V(I)$ characteristics were localised to particular sections of the superconducting wire. The current at which the steps are observed decreases as the temperature is increased, consistent with the local critical current being inversely related to the temperature.

$V(I)$ data from the single Pb nanowires [48] is shown in Figure 2.14(b). There are clear voltage steps in the current-biased measurements, and the magnitudes of these steps are very close across different samples - this is consistent with the SBT model

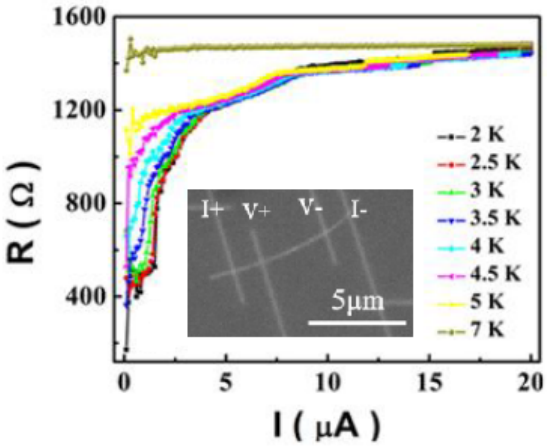

Figure 2.15: Resistance vs current of a 55nm Pb nanowire at different temperatures. Inset is the SEM image of the four-electrode measurement setup [49].

above, with the differences in the $I(V)$ characteristics between the samples being due to differences in imperfections. There is also evidence that the PSCs behave differently under voltage-bias, resulting in an S-shaped curve; this behaviour is not discussed here as no $I(V)$ curves were measured for the samples examined in Chapter 4.

Figure 2.15 shows R(I) data obtained from individual single-crystal Pb nanowires [49]. The steps in the data are attributed to weak spots in the wire acting as PSCs; the explanation given is that the proximity of the Pt electrodes (see inset image) weakens the superconductivity of the Pb nanowires, enhancing the PSCs.

PSCs are very similar to hotspots (see Section 2.5) in that they cause a discrete contribution to the resistance of the wire. The phase slip process results in localised dissipation of energy, which causes a local temperature rise. If the bias current through the PSC is high enough, the power being dissipated can heat the wire enough to turn the PSC into a fully-normal spreading hotspot. This creates curvature in the $V(I)$ graphs; as the bias current is increased and PSCs with higher critical currents are activated, the first few PSCs formed will have large normal currents passing through them and be heating the surrounding wire, creating a non-linear contribution to the overall resistance alongside the steps from later PSCs.

Figure 2.16(a) shows the $V(I)$ curve for a single PSC; the effect of heating in the PSC is clear. The SBT model fit is shown both excluding and including heating effects,

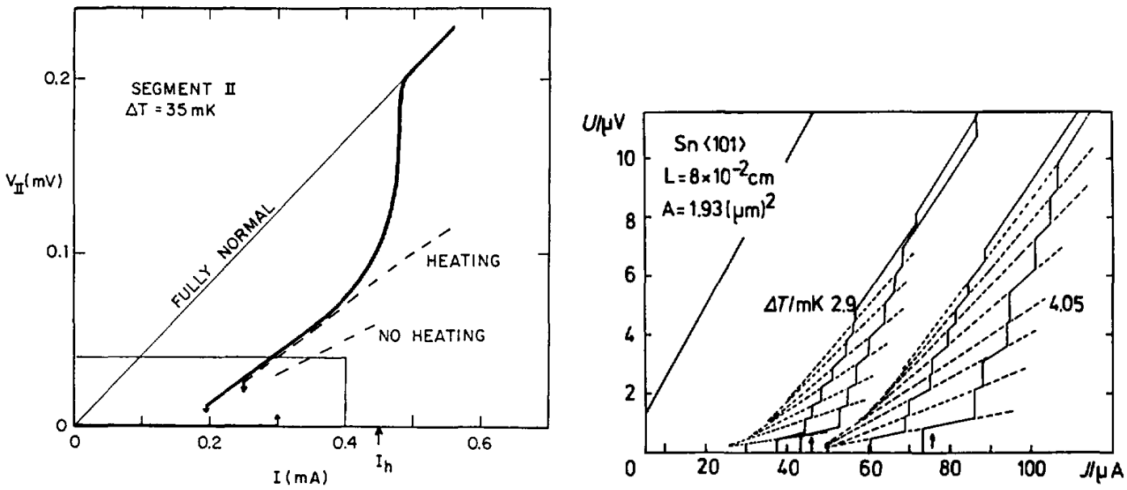

Figure 2.16: (a) Heating effects in a PSC for large ΔT. The solid line is the experimental I-V curve of segment II (see Figure 2.14(a) inset). The dashed curves are the SBT PSC theory with and without corrections for heating, using $2\Lambda = 14\mu$m for best fit to the heating curve. I_h (arrow) is the theoretical value for the current that can sustain a large normal hotspot. [44] (b) Current-voltage characteristics for tin whisker crystals [47].

with the latter providing a clear improvement of fit. The SBT model predicts hysteresis in the $V(I)$ data when hotspot characteristics are added, but the experimental data shows hysteresis beyond what the hotspot model explains; SBT postulate [44] that PSCs could explain the additional hysteresis. Figure 2.16(b) shows $V(I)$ characteristics for tin whisker crystals, which exhibit ideal PSC behaviour [47]. There is considerable hysteresis observed between increasing and decreasing $|I|$, despite the fact that heating effect were calculated to be quite small due to low dissipation and good thermal conductivity.

2.5 Hotspots

A hotspot is a region in a superconducting wire where the local temperature has increased above the critical temperature and the wire is in the normal state. A hotspot forms when the superconducting current exceeds a critical current at some point in the wire and thermal dissipation occurs, heating the surrounding area of the wire. The hotspot will then spread until the heating within it is balanced by the cooling from the

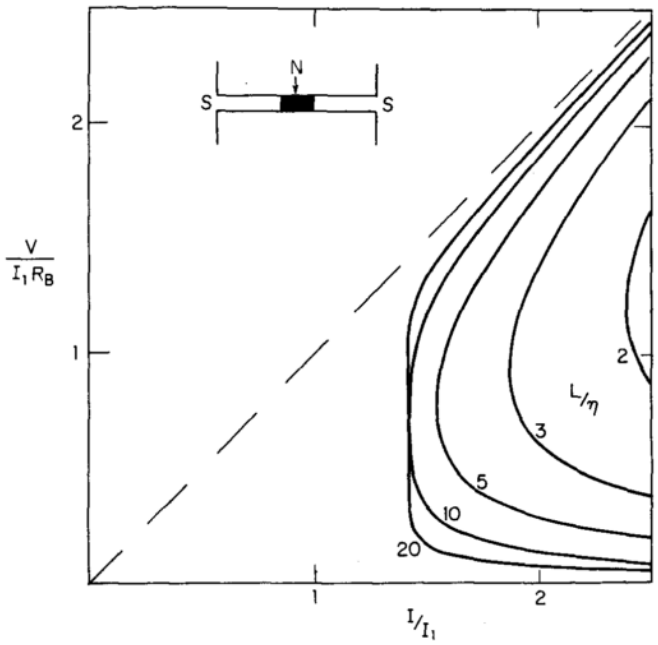

Figure 2.17: Theoretical I-V characteristics for the SBT model of hotspots in long microbridges. $I_1 = I_h$ defined in Equation 2.46 and $R_B = \rho L/Wd$. The inset shows the geometry assumed. [50]

surroundings.

The SBT model of hotspots [50] was proposed as an explanation for effects observed in superconducting microbridges. In the model, a hotspot is described as a balance between Joule heating per unit area of the microbridge and surface transfer of heat per unit area to the surrounding environment, with the size of the hotspot depending on the applied voltage.

The inset of Figure 2.17 shows a long microbridge of width W and thickness d. For this geometry, the hotspot is localised within the wire; heat is generated in the normal-state hotspot region and removed via conduction through the wire to the wide films at either end, and to the substrate. The region contributing to the overall resistance is a well-defined segment of normal-state film which spans the width of the wire, so the resistance of the hotspot is simply given by

$$R = 2x_0\rho/Wd, \tag{2.45}$$

where x_0 is the "radius" of the hotspot.

The current required to generate enough heat to balance surface heat transfer from a hotspot is given by

$$I_h = \sqrt{\frac{2\alpha W^2 T_c d}{\rho}}(1-t)^{1/2}, \tag{2.46}$$

where $t = T_{ambient}/T_c$ is the reduced temperature, α is the heat transfer coefficient per unit area of the substrate and ρ is the resistivity of the normal region. An assumption is made that the large films at either end of the microbridge are approximately at ambient temperature due to the increased surface area.

I_h is generally independent of the voltage, and hence of the size of the hotspot. However, in the bridges considered by SBT, there are two regimes where this is not the case. The current increases at low voltages because as the size of the hotspot gets small compared to the characteristic thermal healing length,

$$\eta = \sqrt{\frac{Kd}{\alpha}} \tag{2.47}$$

(K being the thermal conductivity of the film), the cooling efficiency increases. Likewise, for high voltages the hotspot increases in size and the boundary between the normal and superconducting regions of the wire approaches the ends of the bridge, increasing the cooling efficiency due to the proximity of the boundary to the wide film (which was assumed to be at ambient temperature). This theoretical behaviour is shown in Figure 2.17.

Short microbridges (for which both the length L and width $W \ll \eta$) are considered separately in the SBT model, because the assumption of the wide pads being at ambient temperature no longer holds - the hotspot "spills out" into the pads, as shown in the inset of Figure 2.18. The current required to maintain the hotspot now becomes

$$I_h = \sqrt{\frac{Kd^2 T_c}{\rho}}(1-t)^{1/2}, \tag{2.48}$$

and the resistance of the hotspot is

$$R(r_0) = \frac{\rho}{d}\left[\frac{L}{W} + \frac{1}{2} + \frac{2}{\pi}\ln\left(\frac{2r_0}{W}\right)\right], \tag{2.49}$$

i.e. the sum of the normal-state resistance of the bridge and the resistance contribution from the heated region in the pads.

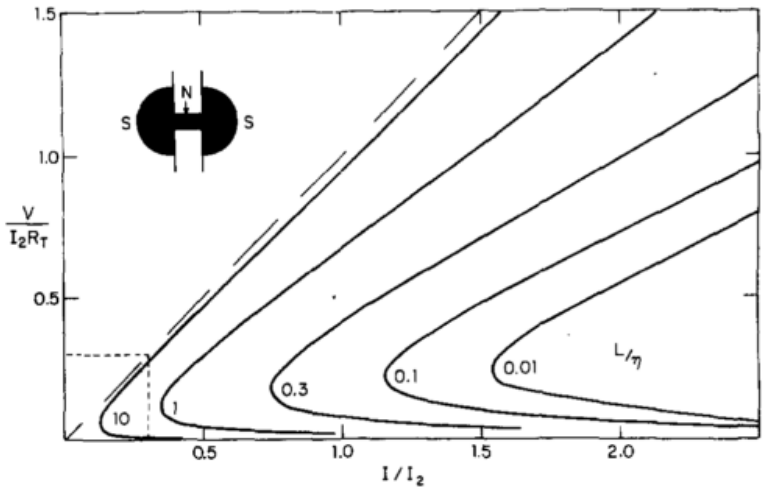

Figure 2.18: Theoretical I-V characteristics for the SBT model of hotspots in short microbridges. $I_2 = I_h$ defined in Equation 2.48 and R_T is calculated from Equation 2.49 with $r_0 = 1$cm. The lower left corner, suitably scaled, corresponds to Figure 2.17. The inset shows the geometry assumed for large hotspots. [50]

2.5.1 Hysteresis in I-V characteristics

One of the effects that has been observed in the I-V characteristics of a number of quasi-one-dimensional systems [50–52] is hysteresis, where the current at which resistance appears in a sample under increasing bias current does not match the current at which it disappears under decreasing bias current. Hotspots provide a consistent explanation for this, due to the difference in magnitude between the critical current I_c and the current I_h required to maintain the hotspot.

As the bias current through the sample is increased, it will remain superconducting with zero resistance (in the absence of other phenomena) until I_c is exceeded. Before then, there is no dissipation and no hotspot; above I_c, a hotspot forms due to thermal dissipation. If $I_h < I_c$, the bias current can then be decreased below I_c without superconductivity reforming in the normal-state region. Figure 2.19 shows $V(I)$ data for a short tin microbridge; the hysteretic behaviour is indicated by arrows along the current axis.

For conditions where $I_c < I_h$ (generally near T_c), or in cases where dissipation is low, hotspots cannot explain hysteresis in I-V characteristics. One possible source that has been suggested are PSCs (see Section 2.4).

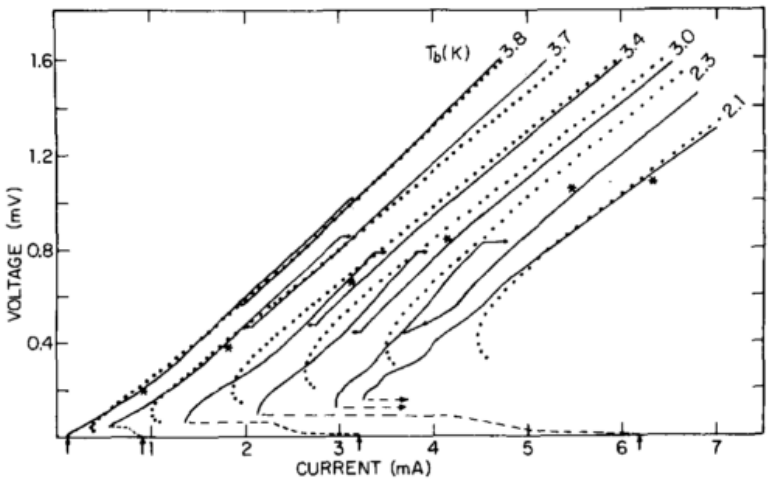

Figure 2.19: I-V characteristics for a short microbridge as a function of temperature. The dotted curves give the fit from SBT hotspot theory. The asterisks indicate the energy-gap voltage $2\Delta(T_b)/e$. [50]

2.6 Shapiro steps

Shapiro steps (SSs) are steps that occur in V(I) data when microwave radiation is applied to a superconducting sample. The steps are sections of relatively constant voltage (as opposed to PSCs where the steps are discrete increases in the voltage).

Figure 2.20(1) shows SSs as first observed by Shapiro in $Al/Al_2O_3/Sn$ "wires" (which were closer to two-dimensional than one-dimensional) [53].

Cuevas and coworkers [55] examined a superconducting point contact and showed that SSs arise due to the interplay between the ac Josephson current components and the microwave signal, and appear at voltages

$$V = \frac{m}{n}\frac{\hbar\omega_r}{2e}, \tag{2.50}$$

where m and n are integers, and ω_r is the radiation frequency. The $n = 1$ case corresponds to harmonic Shapiro steps found in tunnel junctions [53], while $n \neq 1$ corresponds to subharmonic Shapiro steps; these are a signature of the ac Josephson junction effect [55].

Generally, SSs are expected to occur when microwave radiation is externally applied to a sample. However, recent experiments have indicated that this is not always the case, though microwave radiation is still involved. Non-standard external sources have

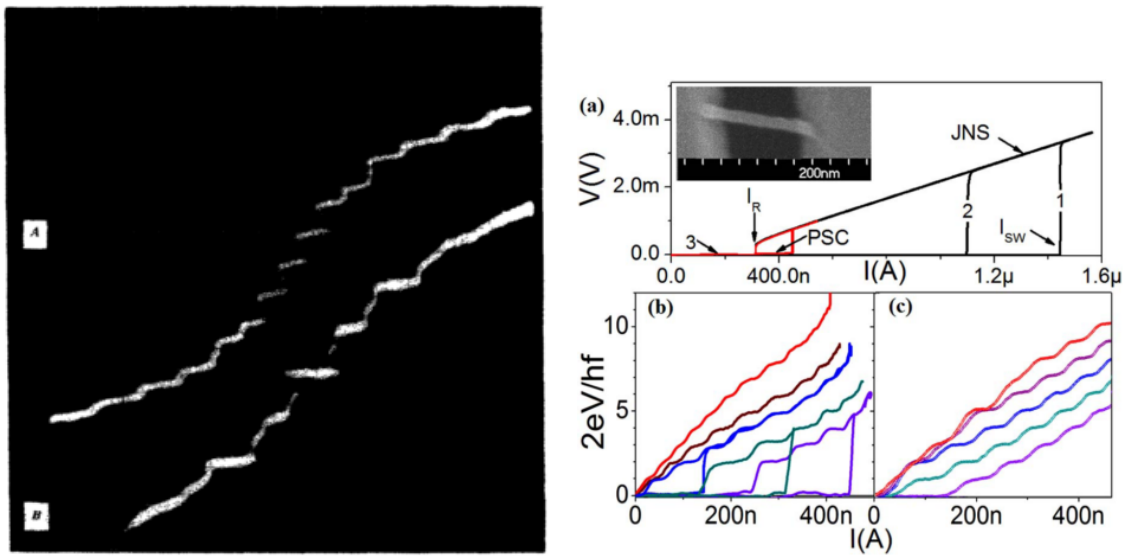

Figure 2.20: (1) Microwave power at 9300 Mc/sec (A) and 24850 Mc/sec (B) produces many zero-slope regions spaced at $hv/2e$ or hv/e. For A, $hv/e = 38.5\mu$V, and for B, 103μV. For A, vertical scale is 58.8μV/cm, horizontal scale is 67 nA/cm; for B, vertical scale is 50μV/cm, horizontal scale is 50μA/cm [53]. (2) (a) Positive bias, V(I), curves taken at $T = 290$mK with the switching current, I_{sw}, return current, I_R, JNS, and PSC regimes indicated with arrows. Curve 1 (black) is measured at zero MW power and curves 2 (black) and 3 (red) are measured at -31 and -21 dBm output MW powers at 3 GHz frequency. (b) Normalized voltage, eV/hf vs. I curves for the PSC regime in sample A for applied MW powers decreasing from top to bottom curves. These curves end where the wire switches to JNS. (c) Numerical simulations of fractional Shapiro steps; the simulated curves show a similar shape to the experimental ones [54].

been successfully utilised - for example, Ref. [56] used a voltage-biased junction as a microwave source to induce SSs in a Josephson junction a few μm away, though steps were was only observed for $0.9T_c \leq T \leq 0.99T_c$. In some systems, a controlled source is not even necessary. SSs were observed in Au nanowires between superconducting electrodes [57] and were attributed to the interplay between ac Josephson current and a superconducting minigap δ which characterises the proximity induced superconductivity in the Au wire (rather than the superconducting gap Δ of the electrodes). The microwave radiation required for SSs comes from the excitation of quasiparticles in low-lying Andreev bound states (ABSs). Microwave radiation is emitted by a quantum jump of quasiparticles from the ABSs above $+\delta$ to the ABSs below $-\delta$, and has a

frequency $\omega_r = 2\delta/\hbar$.

There are no instances known to the author where SSs were observed in the absence of any source (internal or external) of microwave radiation.

2.7 Vortices

Phase slips are the result of the superconducting order parameter going to zero at some point along a quasi-one-dimensional superconducting wire. For superconductors which are closer to quasi-two-dimensional, the phase slip phenomenon is not observed, mainly because if the order parameter is zero at some location and a local region of the superconductor becomes normal, superconducting current can just flow around these points - the long-range superconductivity is not broken. However, such points of suppressed superconductivity do still occur in two-dimensional films, and have a noticeable effect on the overall conductivity.

Vortices occur in a superconducting film where the superconductivity is suppressed by a magnetic flux through the film. They are vortices of current that circle the point where a quantised unit of magnetic flux penetrates the superconductor. As will be described below, the presence of vortices in a superconducting film can give rise to resistance through movement of the vortices (known as flux-flow), and even in the absence of an external magnetic field a non-zero resistance can be observed; this is caused by a phase transition which can be observed experimentally.

2.7.1 Isolated vortices

As described in Section 2.1.3, type-II superconductors have two critical fields H_{c1} and H_{c2}, and for field strengths between them there exists a mixed or Schubnikov state. In this phase, magnetic field can penetrate the superconductor in the form of quantised vortices - small regions within the superconductor which become normal as the order parameter is suppressed to zero by the penetrating field; current vortices flows around these points.

Figure 2.21 shows the basic structure of a vortex in terms of the penetrating magnetic field and the magnitude of the superconducting order parameter. $\kappa = \lambda/\xi$ is the GL parameter, and type-II superconductors have $\kappa > 1/\sqrt{2}$. As was the case for

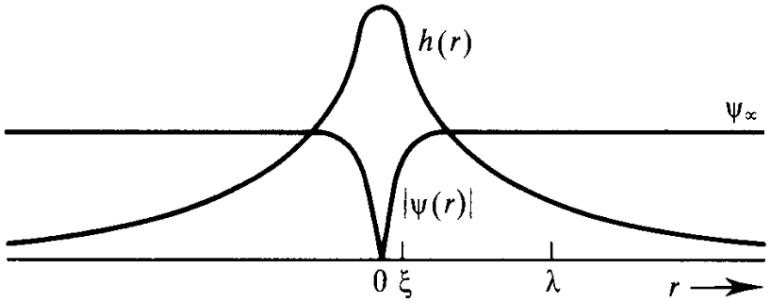

Figure 2.21: Structure of an isolated Abrikosov vortex in a material with $\kappa \approx 8$. The maximum value of the penetrating magnetic field $h(r)$ is approximately $2H_{c1}$ [5].

phase slips (Section 2.3.2) and PSCs (Section 2.4.2), the order parameter becomes suppressed over a core region of around the coherence length $\xi(T)$, and the magnetic flux is strongest within this region. Vortices interact with each other with a logarithmic potential over a scale less than the transverse penetration depth (the characteristic length over which a two-dimensional superconducting system screens perpendicular magnetic fields),

$$\lambda_{\perp} = \lambda_{eff}/d, \tag{2.51}$$

where λ_{eff} is the effective penetration depth of a dirty superconducting material in the bulk.

Each vortex carries a quantum of magnetic flux $\Phi_0 = hc/2e = 2.07\times10^{-15}$Wb. This quantisation arises from the requirement that the superconducting order parameter be single-valued throughout the superconductor. Therefore, after circling once around the vortex the phase of the order parameter is restricted to changing only by an integer multiple of 2π (for reasons similar to those discussed in Section 2.3.2 for phase slips); the current flowing around the vortex is thus quantised, and so is the magnetic flux through the centre of the vortex.

When an external bias current is applied across a sample, the superconducting current will in general avoid any normal regions and instead flow through the surrounding superconducting regions. This remains true for stationary vortices, but not for free ones. A vortex will experience a Lorentz force $J \times \Phi_0/c$ caused by the interaction between the magnetic flux quantum passing through it and the superconducting current. If no other forces are constraining the vortex to a particular location ("pinning" it),

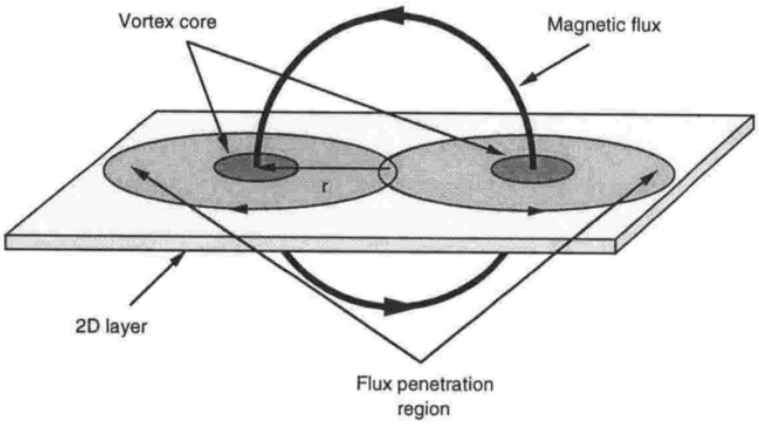

Figure 2.22: A thermally created vortex-antivortex pair bound together to form a vortex loop of radius r threading through the superconducting layer [58].

the vortex will move with some velocity v perpendicular to the current. The Maxwell equations imply that there is an electric field associated with a moving magnetic field; in the case of the magnetic flux through a vortex core, the electric field will be parallel to the applied current. This causes current to flow through the normal core of the vortex, which results in a resistive voltage that is linearly dependent on the applied current [5].

2.7.2 The BKT zero-field phase transition

As described above, a magnetic field passing through a two-dimensional superconducting film becomes quantised into vortices. However, it is possible to have vortices without an externally-applied magnetic field - thermal fluctuations can create pairs of vortices in the film.

Figure 2.22 shows a thermally created pair of vortices in a two-dimensional superconducting film. They manifest as a small self-contained loop of magnetic flux which circles through the thin film. The vortices form where the magnetic field penetrates the film, and so have opposite signs due to the opposite directions of the magnetic field through them; the overall magnetisation of the superconducting film is unchanged by the presence of the vortex pair. As with the isolated vortices described above, the interaction between the vortex-antivortex pairs has a logarithmic dependence on distance.

At zero temperature there are no thermal fluctuations, and hence no vortex pairs. As the temperature is increased, pairs of vortices will be created which are bound together tightly in a Berezinskii phase [59, 60]. At some point though the temperature will be great enough that the vortex pairs which are furthest apart start to unbind. A pair of free vortices has greater entropy than a pair of bound vortices because of the greater multiplicity of states in the film which can be independently occupied, so vortex unbinding is entropically favourable. But a single free vortex has a higher energy than a bound vortex, which is the reason that thermal fluctuations do not produce free vortices preferentially over bound ones. Hence the vortex unbinding will only occur when the thermal fluctuations in the system exceed the required energy increase from a bound vortex to a free one. This transition is known as the BKT phase transition. The phase boundary has a sharply-defined temperature which is defined implicitly as [61]

$$T_{BKT} = \frac{\Phi_0^2}{8\pi k_B \mu_0 \lambda_\perp(T_{BKT})}. \tag{2.52}$$

As mentioned in Section 2.7.1, an applied bias current exerts a Lorentz force on a free vortex, resulting in flux-flow dissipation which contributes to the resistance of the film. However, a bound vortex-antivortex pair experiences an equal and opposite force on the two vortices - there is no net Lorentz force, and so no contribution to the overall resistance. Resistance does occur at temperatures below T_{BKT} though; bound pairs can be dissociated through a combination of thermal fluctuations and the applied current. In fact, even at very small currents there are always some vortex pairs that are broken, meaning that the "true" critical current of a two-dimensional superconductor is zero [62]. The rate at which the bound pairs dissociate is proportional to $\exp(-U/k_BT)$, where U is inversely proportional to both the magnitude of the current and the separation of the vortex pair [58]. This means that the voltage increases as

$$V \propto I^{\alpha(T)}, \tag{2.53}$$

namely a power law. α decreases as the temperature increases; for temperatures just below the BKT transition temperature, $\alpha(T_{BKT}) = 3$ [62].

Above T_{BKT} there are free vortices present in the superconducting film, which give a linear contribution to the resistance (as mentioned above). At temperatures just above T_{BKT} the density of free vortices is low, and so the linear voltage increase occurs only

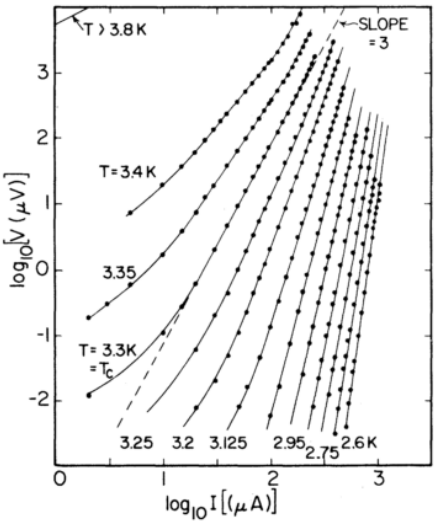

Figure 2.23: Low-temperature I-V curves on a log-log plot, for various fixed temperatures. The dashed line with slope = 3 corresponds to T_{BKT} [62].

at low currents, while the aforementioned dissociation of vortices dominates the free vortex density at high currents, causing the power law increase. As the temperature is raised further above T_{BKT} the zero-current density of free vortices increases, which causes the linear voltage relationship to dominate at a higher range of currents.

Knowing these behaviours, the presence of a BKT phase transition in a superconducting two-dimensional system can be determined by examining V(I) curves at different temperatures - in the low bias-current region, there is a sharp transition from power law behaviour to linear behaviour as the temperature increases past T_{BKT}. Figure 2.23 shows $V(I)$ curves for ultrathin (100Å) quench-condensed films of an alloy of Hg and Xe. As the temperature increases, the value of α decreases; as the boundary of $\alpha = 3$ is crossed, the low-current region of the curve begins to show a clear deviation towards a linear relation of $\alpha = 1$.

The transition can also be observed in $R(T)$ curves. Above T_{BKT} the resistance of a superconducting film is given by the Halperin Nelson (HN) formula [63, 64]

$$R_{HN} = 10.8 b R_{n,f} \exp\left[-2\sqrt{b\frac{T_c - T_{BKT}}{T - T_{BKT}}}\right], \tag{2.54}$$

where $R_{n,f}$ is the normal state resistance per square of the film and b is a tunable constant. This model does not account for behaviour below T_{BKT}, where it predicts

zero resistance.

The BKT phase transition has been predicted to occur in many two-dimensional systems, such as superfluids and melting solids as well as superconductors. Within the latter, the BKT transition has been observed in systems such as quench-condensed films [62], granular films [65] and amorphous films [30, 66].

2.8 Relationships between the phenomena

The various phenomena described above - phase slips (Section 2.3), phase slip centres (Section 2.4), hotspots (Section 2.5), Shapiro steps (Section 2.6) and vortices (Section 2.7) - are quite closely related, as has been mentioned in part during the discussion of each.

Both phase slips and vortices are manifestations of the superconducting order parameter being suppressed at some point within the superconductor - the difference between them is primarily the dimensionality of the superconducting sample. The flux-flow process which gives rise to resistance in two-dimensional films consists of vortices moving across the film perpendicular to the direction of current flow. If the width of the film is reduced towards the quasi-one-dimensional limit, eventually a single vortex would span the film, and so a vortex crossing the film would momentarily break the phase coherence and suppress the superconducting order parameter to zero; this is equivalent to a single phase slip.

Phase slips are a random stochastic process and can occur anywhere along a one-dimensional wire, with the net rate along the entire wire giving the overall resistance; PSCs localise phase slips to a single location, causing a potential difference at that point, but leaving the remainder of the wire unaffected.

PSCs activate when the local superconducting current is exceeded; if the bias current is increased far above this point, the normal current passing through the PSC can be great enough that the heat being dissipated can turn it into a fully-normal spreading hotspot [44].

2.9 Percolation theory

All of the theories discussed in this chapter so far have modeled simple one- and two-dimensional systems, and the models fit well to experimental data for similar systems (e.g. quasi-one-dimensional whiskers or nanowires, uniform micro-bridges, quasi-two-dimensional thin films). However, the samples that will be prepared and measured in this research are by no means simple; as will be described in Section 3.1, they are networks of lead clusters deposited at random on a substrate.

One would at first glance be inclined to believe that no meaningful data could be obtained from such samples, but it turns out that while the individual samples themselves are unique in terms of their exact morphology, their overall characteristics are suprisingly well-defined. Systems like these are commonly described in terms of percolation theory.

Percolation theory [67, 68] is a mathematical theory which describes disordered systems in which the disorder is quantified by random variations in the degree of connectivity of the system. The literature generally refers to groups of connected sub-units within a system as "clusters"; to distinguish these from the individual lead nanoclusters used in this research, the groups of connected sub-units will be referred to henceforth as "islands".

The core idea behind percolation theory is that the connectivity of a system can be categorised in terms of the presence of an infinite spanning island, or (in the case of a finite system) an island which spans from one side of the system to the other. The presence of such an island is linked to the "coverage" p of the system. If $p = 0$ defines one extreme where all sub-units in the system are completely isolated (so there is no spanning island), and $p = 1$ defines the other extreme where all sub-units are connected to the maximum number of neighbouring sub-units (so a spanning island exists), then there is a critical coverage p_c which defines the cross-over between a spanning island existing or not in the system.

One of the simplest percolating systems is a square lattice of "sites", where occupied sites are connected to form islands if they are adjacent horizontally or vertically; p gives the fraction of occupied sites, and $1-p$ gives the fraction of vacant sites. This is known as site percolation, and is a form of lattice percolation (where the percolating elements can only occupy positions in a well-defined lattice). It has been shown that an infinite

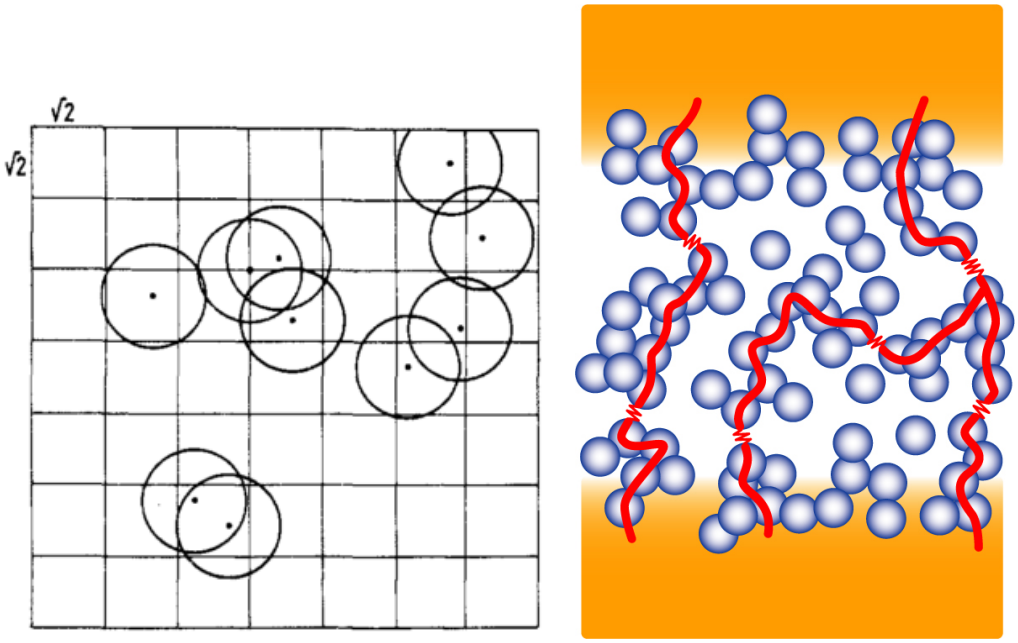

Figure 2.24: (a) Typical configuration of ten discs situated in a $\sqrt{2}L \times \sqrt{2}L$ area with $L = 7$ at a concentration below the percolation threshold [69]. (b) Diagram of a percolating film between two electrical contacts. The film is just below the percolation threshold; there is no spanning island, but conduction pathways (shown in red) still exist.

spanning island will exist in the system when the fraction of occupied sites in the system exceeds [68]

$$p_c = 0.593. \tag{2.55}$$

Lattice percolation can describe a variety of regular systems, but is unsuitable for systems with less constraints on the locations of the sub-units. A more general form of percolation, known as continuum percolation, describes percolation in systems where the sub-units can take any position; an example of this is a two-dimensional percolating system consisting of overlapping, non-interacting discs (Figure 2.24(a)). In this situation, the coverage is expressed as a fractional coverage ρ of the total system area, and the critical coverage is [69]

$$\rho_c = 0.68. \tag{2.56}$$

For percolating systems in a two-dimensional space where the size of the percolating sub-units is much smaller than the overall system size, the system itself can be thought

of as having an intermediate dimensionality between 1 and 2 - while large individual islands would still technically be two-dimensional, on the scale of the entire sample the percolating pathways are closer to one-dimensional.

The samples in this research (described in Section 3.1) can be approximated by the two-dimensional non-interacting disc model. However, if quantitative analysis of the critical onsets were to be performed then a correction would need to be made - the clusters are three-dimensional objects and can be stacked, so as the coverage increases the probability of a cluster landing above the first layer of clusters increases. Therefore, a distinction must be made between the total coverage ρ_T and the surface coverage of the first layer of clusters ρ_1; these are related by [70]

$$\rho_T = -\ln(1 - \rho_1), \tag{2.57}$$

i.e. ρ_T can increase beyond 1, while $0 \leq \rho_1 \leq 1$.

In real films, a spanning island does not need to exist in order for conduction to be possible. Figure 2.24(b) shows a diagram of a simple percolating film between two electrical contacts. Classically a spanning island would be required to have conduction; in reality, a current can pass through the sample due to quantum tunneling of electrons between adjacent islands in the percolating film.

3

Experimental setup

In Section 3.1 the samples themselves are described. The cluster deposition setup used to prepare the samples is described in Section 3.2, and the beam profile is covered in Section 3.4. The sample deposition and analysis process is described in Section 3.5, and in Section 3.6 the characterisation of the cluster beam is presented.

3.1 Sample structure

The samples studied in this research consist of random percolating networks of Pb nanoclusters deposited onto a silicon nitride substrate between gold electrodes. An overview of percolation theory was given in Section 2.9; the key idea used here is that a potential difference is applied across the electrodes, and then clusters are deposited randomly onto the substrate until a current begins to flow through the sample. Unlike pure percolation theory, conduction begins before a spanning island forms, due to quantum tunneling of electrons between adjacent islands in the sample.

Figure 3.1(a) shows the substrate and the contact pad layout used in this research. Two large gold pads on either side of the substrate form the contacts to the measurement circuitry. The pads are connected to a 200μm wide gold wire which is broken in the middle by a 100μm gap; the percolating film that is studied forms across this gap. This is a standard design that has been previously used in the group.

The individual 10mm $\times$ 10mm substrate chips were prepared on (and cleaved from) a 3" silicon nitride wafer. The contacts were placed on the surface via evaporation, and were defined using the physical mask shown in Figure 3.1(b) - the mask was placed

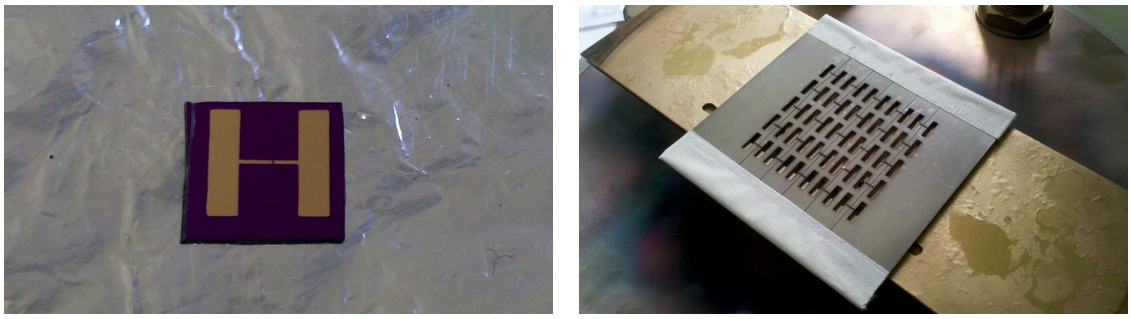

Figure 3.1: (a) The substrate and contact pad layout. (b) The physical mask used to evaporate the contacts onto the substrates.

with the wires directly against the wafer to ensure that the gap between the contacts was the most sharply-defined feature.

The evaporation itself was performed in an Edwards Auto 306 thermal evaporator loaded with NiCr and Au. After mounting the wafer, the evaporator would be left to pump down overnight to ensure a good base pressure. 5nm of NiCr would then evaporated onto the surface of the wafer to form an adhesion layer, followed by 45nm of Au to form the contacts.

3.2 Equipment setup

Figure 3.2 shows the experimental setup. The main apparatus consists of three parts:

- The main cluster deposition system which generates the clusters for use in sample deposition [71].
- A Janis Research SVT400 cryostat in the deposition chamber; the samples can be electrically measured via wires connected to a vacuum feed-through, and several thermocouples and a heater enable the temperature of the samples to be monitored and controlled (using a Cryo-Con Model 32 cryogenic temperature controller).
- The electronic circuitry, which provides monitoring of the samples during deposition and measurements.

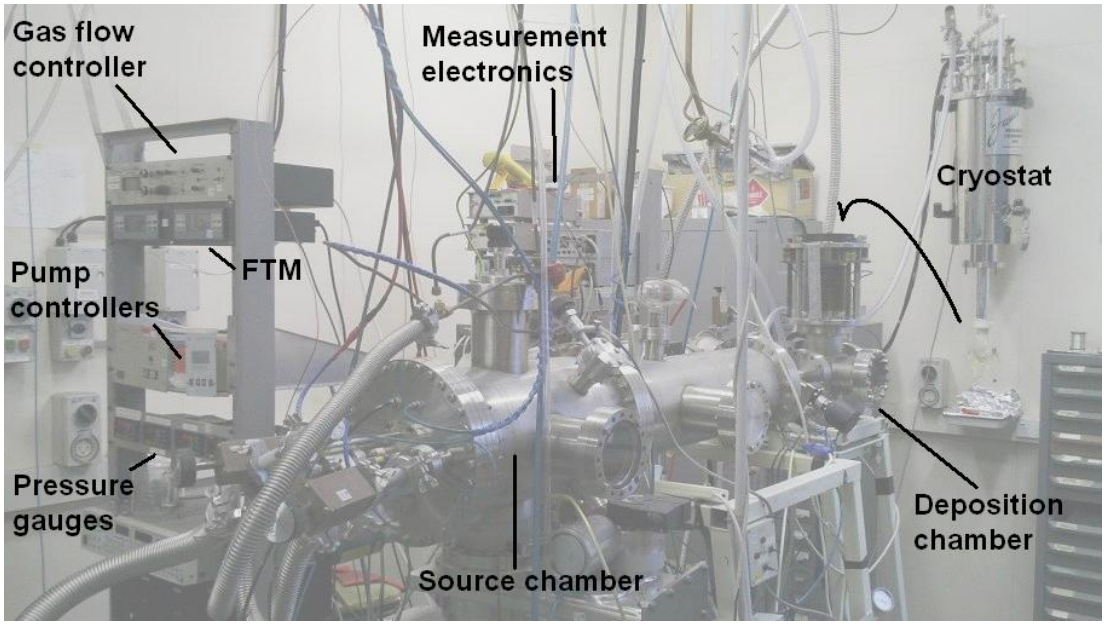

Figure 3.2: The experimental setup.

The clusters were created via inert gas aggregation. This is a process whereby metal is evaporated (using the crucible in Figure 3.3(b)) and then condensed by a stream of cool gas. This results in two phases: a light gas/metal mixture, and pure metal nanoclusters which condense out from the mixture and are tens of nanometers in size.

Figure 3.3(a) shows the internal layout of the cluster source; in addition to the source chamber, there are several subsequent chambers separated by a nozzle and two skimmers [71]. The combination of the gas flow into the source chamber and the pressure differential of the subsequent chambers creates a flow of gas that accelerates the clusters into a beam. The nozzle contributes to the formation of the clusters into a uniform beam as well as enabling a pressure difference between the source and pumping chambers to be generated, while the skimmers select the heavier clusters rather than the lighter gas/cluster mixture which is pumped away. The cluster beam generation process is sensitive to several parameters, which are described in more detail in Section 3.4.

The beam generated by the cluster source passes into the deposition chamber, where it is deposited onto substrates mounted on the cold finger of the cryostat. The sample

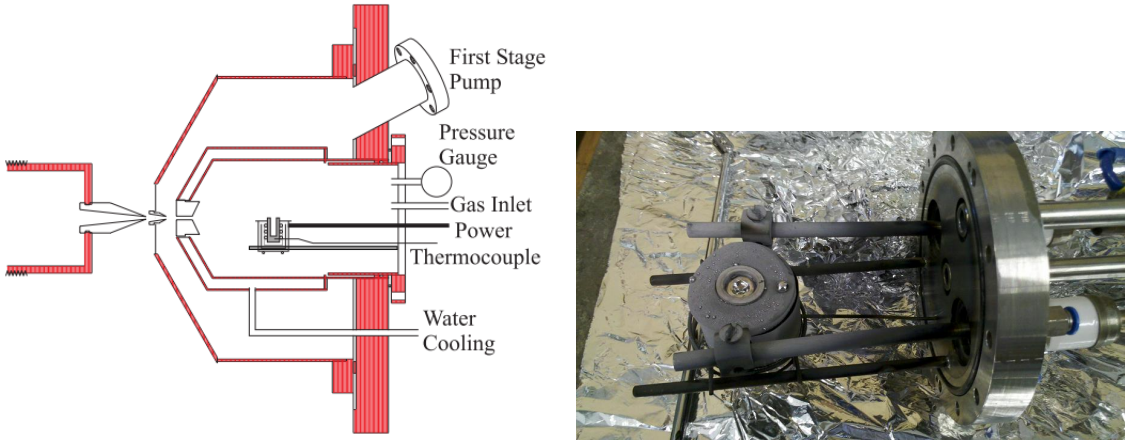

Figure 3.3: (a) Schematic and nozzle placement for the inert gas aggregation source [72]. (b) The crucible from the source chamber.

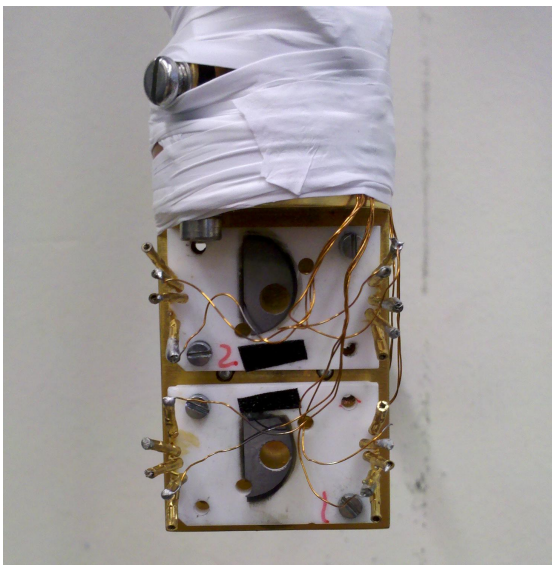

Figure 3.4: The sample holders on the cold finger of the cryostat.

holder is shown in Figure 3.4 and provides two positions for mounting substrates; contact pins make electrical contact to the gold contact pads on the substrates, while the hole in the centre allows clusters to be deposited on the substrate. To the surface of the sample mounts, a third bare silicon nitride chip was usually attached with carbon tape in order to measure the cluster sizes (see Section 3.6).

A typical system run went as follows:

1. Clean substrates were mounted on the cryostat and their electrical connections checked.
2. The cryostat was mounted in the deposition chamber.
3. Water cooling for the system was turned on.
4. The source and deposition chambers were pumped down.
5. Once the source chamber was at low pressure, the crucible was heated up towards 780°C.
6. At around 600°C, the gas flow was turned on.
7. The cluster beam rate was measured and allowed to stabilise.
8. The samples were deposited.
9. The crucible heater was turned off and allowed to cool.
10. Once below 90°C, the source chamber was shut down.
11. The cryostat was cooled down overnight and the samples measured over the subsequent days.

If the samples were going to be deposited at low temperature, the cryostat was instead mounted and pumped down the previous day and then cooled overnight.

3.3 Measurement circuitry setup

The primary method of insight into the characteristic behaviour of the samples was through their conductive properties. The conductance between the sample contacts was monitored during deposition, and both R(T) and V(I) measurements were made on the samples after deposition.

Figure 3.5(a) gives the electronic setup used to monitor the samples during deposition and to make some of the $R(T)$ measurements. A custom-built voltage ramp box was used to provide either a constant dc voltage (for monitoring the samples during

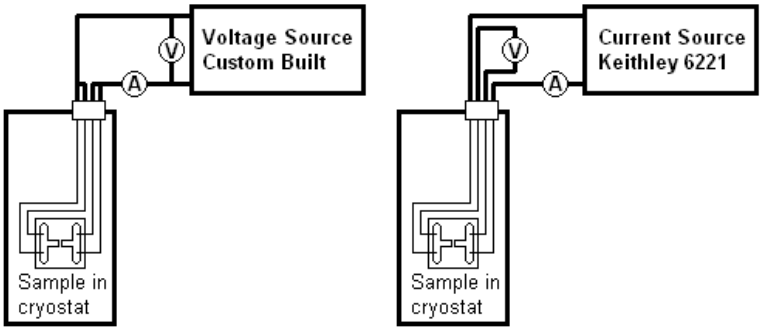

Figure 3.5: Circuit diagrams for (a) voltage-biased two-point measurements, and (b) current-biased four-point measurements.

deposition and as a bias for early $R(T)$ measurements) or a triangle-wave voltage ramp (used to induce changes in the samples), and the applied voltage was measured with a Keithley 2000 Multimeter. The current through the sample was measured with a Keithley 6514 System Electrometer. The resistance was calculated from the measured current and voltage. To protect the samples from electrostatic effects from people moving around near the experimental setup, all connections were made using the inner core of shielded coaxial cables, and the outer shield connections of the cables were all connected to a common ground.

Figure 3.5(b) gives the modified setup used to make $I(V)$ measurements and most of the $R(T)$ measurements. In this configuration, a Keithley 6221 Current Source was used to apply a bias current, and a Keithley 2182A Nanovoltmeter measured the potential drop across the samples.

Data acquisition was performed with LabVIEW, connected to the Keithley boxes and the temperature controller via GPIB. While the current source did have capabilities for automated current ramping and differential resistance measurements, the control available over the automated features was limited, and so the current ramping was implemented in code.

3.4 Beam profile

In order to obtain useful results, the method of producing samples needed to be both reliable and repeatable. This is highly dependent on the clusters arriving in the depo-

sition chamber.

Obtaining a uniform cluster beam profile was one of the hardest things to achieve. There are several different parameters that affect the beam profile and composition.

1. the shape and size of the nozzles.
2. the temperature of the source metal.
3. the composition of the gas.
4. the rate of gas flow into the source chamber.
5. the rate of pumping on the various stages of the system.

To reduce the complexity of the problem, several of these variables were held constant for the duration of the research. The rate of pumping was the hardest variable to quantatively control, and so the various pumps in the system were left to always pump at maximum capacity, and valves between the pumps and the chambers were left fully open during operation. The composition of the gas was also left constant; the experimental setup had the capacity to flow both argon and helium at any ratio desired, but for these experiments no helium was used. (In fact, the helium line was blocked off partway through the research as part of an effort to prevent oxygen leaking into the system - the effect of oxidation on the samples will be discussed in Section 4.1.)

The beam profile could be measured at two locations along the beam path - in the middle of the mass selection chamber, and in the deposition chamber itself. In the deposition chamber, a large offcut of silicon nitride or silicon oxide was attached to the sample mount; once the system was operating this was then exposed to the cluster beam for an extended period of time, creating a thick cluster film on the substrate which gave an indication of the relative intensity of the beam as a function of position across the beam spot.

Measuring the beam profile in the mass selection chamber was trickier, due to there being no way to shut off the cluster beam before that stage. This meant that the sample point had to be movable so that the beam could be selectively sampled. To achieve this, a linear translator was added with a metal mount on the end. A silicon oxide wafer was attached to the mount while the system was shut down and could be

Figure 3.6: Beam profiles obtained for (a) the set of nozzles used in the research, and (b) an alternative set of nozzles.

opened up, and then once the system was running, the wafer was raised into the path of the beam for an extended period of time to create a deposition pattern, which could then be studied once the system was completely shut down and vented. The downside of this process was that the beam profile could only be sampled in the mass selection chamber once per run, and the minimum turn-around time is about five hours.

Figure 3.6 shows two beam profiles obtained for different sets of nozzles (but the same skimmer) - a "butterfly" pattern with two lobes, and a crescent pattern. Numerous combinations of source temperature and gas flow rate were tested to try and effect a change on the beam profile, but the only change occured when the nozzles were swapped out. Eventually, the beam profile in Figure 3.6(a) was used, and the alignment of the deposition chamber was altered so that the lower right lobe coincided with the sample holder.

3.5 Experimental procedure

3.5.1 Sample deposition

To deposit a sample, the source/deposition gate valve was closed to block the cluster beam, and then the cryostat/sample finger assembly was lowered down into position, so that the substrate to be deposited on would be in the path of the beam. A small (generally 30mV) potential was applied across the substrate contacts - this was large enough that a noticeable current increase occurs upon onset, but small enough that the sample would not be damaged. The voltage, current and temperature of the sample

were recorded throughout. Deposition itself was started by opening the source/deposition gate valve, and would proceed until an onset of current through the sample was observed. The deposition would generally continue for anywhere from a few seconds up to a few minutes after onset, depending on the desired target properties of the sample, after which the source/deposition gate valve would be closed.

After deposition was complete, the sample would be monitored for at least fifteen minutes, to ensure its stability and record how the conductance of the sample evolved over time. In cases where the sample broke shortly after ending deposition (predominantly a single set of samples - see Section 4.1), subsequent short depositions were performed to reconnect the sample.

Several of the deposition parameters were recorded:

- T_{Dep} - the temperature of the substrate that the clusters were deposited onto. This was generally either ambient room temperature ($\sim$ 300K) or a low temperature above the bulk T_c of lead (10K was chosen).

- *Rate* - the rate at which clusters arrived in the deposition chamber, in terms of the equivalent film thickness per second. This was measured with a Film Thickness Monitor (FTM), which measures the accumulating mass on a quartz crystal by changes in the vibrational frequency of the crystal.

- t_{Dep} - the length of time for which clusters were deposited on the substrate. Combined with the rate, the deposited thickness of lead could be determined.

3.5.2 Measurement of cluster beam rate

It was not possible to measure the cluster beam rate during deposition, because the beam would be blocked by the substrate. To get around this, the cluster rate was checked with the FTM crystal both before and after a deposition, and the average of the two was taken as the rate during deposition. This required that the cluster beam was reasonably stable, so after the system was started (but before any depositions were done) the beam rate was monitored over a length of time to both allow the beam to stabilise and check that there were no long-period fluctuations or oscillations in the beam rate.

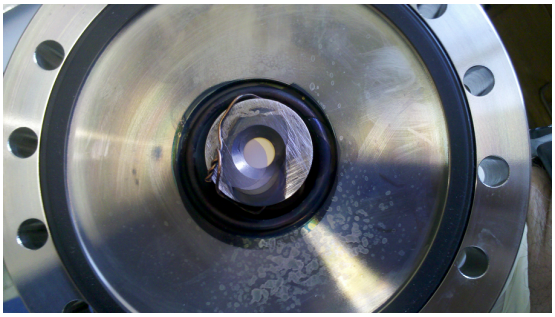

Figure 3.7: The FTM crystal used to measure the deposition rate. The imperfect coverage of the crystal is clear.

Figure 3.7 shows the FTM used to measure the beam rate. Due to the alignment required to get a stable, close-to-uniform beam to make samples with (as described in Section 3.4), the FTM crystal was not completely covered by the cluster beam - this meant that the rates displayed by the FTM, and any thicknesses calculated from them, would be incorrect.

However, if an assumption is made that the beam is uniform, then the imperfect coverage can be corrected: the rate measured by the FTM is dependent on the change in mass of the crystal, which in turn is dependent on the change in volume of added material. So covering the entire area A of the crystal to a thickness d is equivalent to covering half of the area with double the thickness - A and d are inversely proportional. Therefore, the actual thickness of material deposited d_{adj} can be determined using

$$d_{adj} = \frac{A_t}{A_c} d, \tag{3.1}$$

where A_t/A_c is the ratio of total crystal area to covered area. This ratio was determined to be 1.48 from Figure 3.7.

3.5.3 Sample measurement

A variety of electrical measurements were made on the samples after deposition. $R(T)$ curves were generally measured first, because heating and cooling the samples between 2K and 8K had a lower chance of destroying the samples than voltage or current ramps. After that, $V(I)$ curves were measured at various temperatures to map out the behaviour of the samples. For samples that were measured over several days, both

$R(T)$ and $V(I)$ measurements were subsequently repeated to observe the evolution of the sample characteristics. Finally, some samples were subjected to voltage ramps with the aim of intentionally causing the samples to change behaviour. The $R(T)$ and $V(I)$ measurements are presented in Sections 4.3 and 4.4 respectively.

Once electrical measurements were completed, the samples were warmed up, unmounted and then imaged with a Scanning Electron Microscope (SEM). Early films were imaged in a Raith 150 SEM, which had good contrast and enabled critical conduction pathways within some of the films to be observed (e.g. Figures 3.8(a) and 4.2(a)), even though lead is not as good a conductor at room temperature as other metals. The Raith 150 was found however to have poor resolution in the 100k magnification range which was required for cluster characterisation (see next section), so all further images (including all images of the samples to be presented in Chapter 4 were taken with a JEOL 7000F Field Emission-SEM. The morphologies of the samples could be examined in detail and subsequently categorised; Section 4.1 presents the observations.

Initially, the SEM images were not always an accurate view of the samples; coalescence of the clusters, which was negligible at low temperatures, would cause the samples to change as they were warmed up (evidence of this will be given in Section 4.3.2). To mitigate this, the samples were warmed up quickly after the completion of measurements by introducing a small amount of dry helium into the system after the cryogens had boiled off - this meant that there was considerably less time for the samples to coalescence during the warm-up. An alternative method that could potentially protect the sample morphology better would be to introduce a small amount of oxygen into the deposition chamber early on during the warm-up process - the lead clusters would then oxidise, which would inhibit coalescence (as is shown in Section 4.2). Once the samples were above 280K and were vented to air, the lead clusters became oxidised, inhibiting any further coalescence.

3.6 Cluster characterisation

One of the advantages of a cluster generation setup like this is that there is a wide potential range for the size of the clusters being generated. However, it is also an additional parameter - different behaviours would be expected in films consisting of

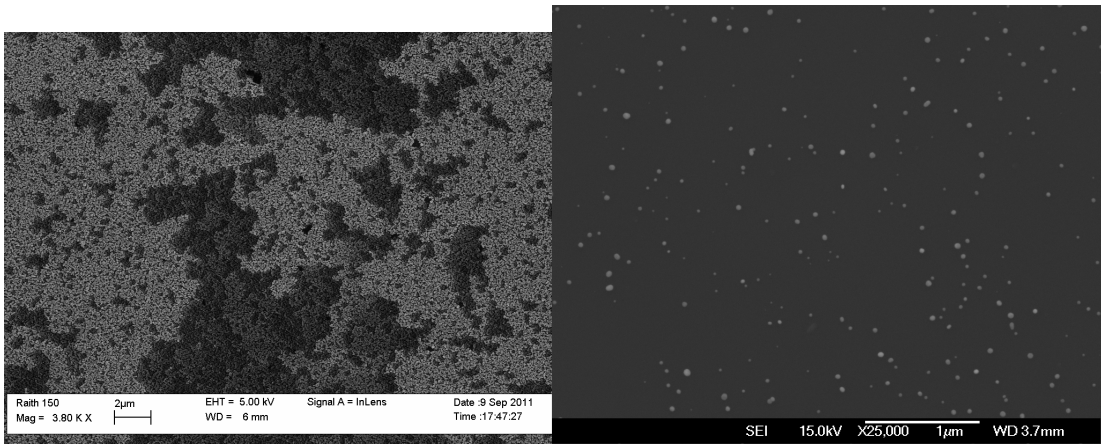

Figure 3.8: SEM images showing (a) a critical conduction pathway through a film, and (b) a low-coverage chip with individual clusters at a magnification of 25k.

different cluster sizes. For samples such as the ones described in Section 3.1 which are created statistically, it is crucial to know that the clusters being deposited are consistent between sample runs, and so being able to measure the cluster size on each individual run is important.

To measure the clusters being produced by the source, a small bare silicon nitride chip was attached to the sample mount alongside the substrates to be deposited on; this chip was then exposed to the cluster beam for two or three seconds to obtain a very sparse film of clusters. Figure 3.8(b) shows an example SEM image of a low-coverage chip; on which individual clusters are clearly visible. Numerous such images were taken of the low-coverage chips at zoom levels of 100k which provided a suitable balance between the number of clusters per image, the accuracy of measurement of individual clusters and the clarity of the image.

From the SEM images of the low-coverage chips, the spread in diameter of the clusters could be determined from the area of the clusters (and assuming circular clusters). Figure 3.9 shows example histograms generated from the obtained cluster images. For the source conditions used in this research, the clusters deposited on the samples were on average between 30nm and 50nm in diameter, though the total spread was $\sim 10 - 80$nm. This distribution was consistent throughout this research.

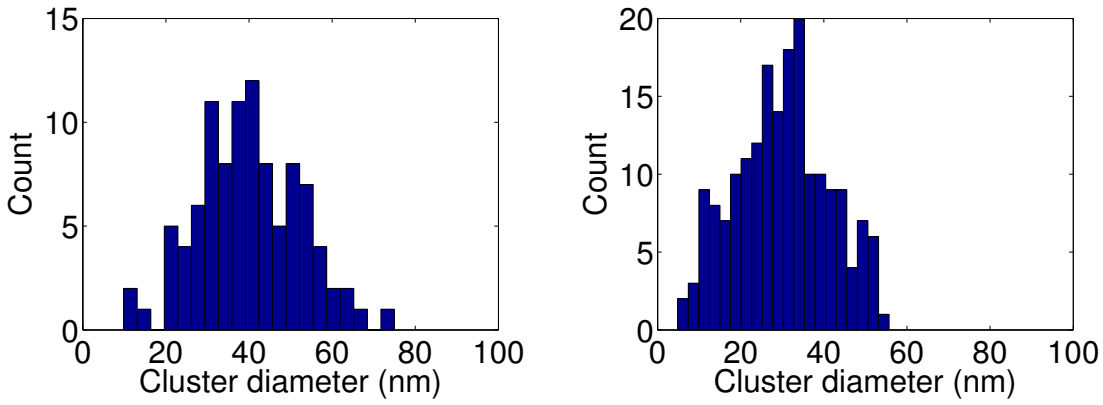

Figure 3.9: Example cluster diameter distributions (measured two months apart).

4

Experimental results

In this chapter, results obtained from experiments described in Section 3.5 are presented. Section 4.1 gives an overview of the samples that were created. Measurements of the onset of resistance during sample deposition are covered in Section 4.2. The $R(T)$ measurements performed on the samples are examined in Section 4.3, and the $V(I)$ curves in Section 4.4. Finally, the presented $R(T)$ and $V(I)$ data is analysed and discussed in Section 4.5.

4.1 Sample overview

Eleven samples with reliable datasets for both $R(T)$ and $V(I)$ measurements were obtained over the course of this research. Two additional samples (S4 and S7) have reliable $R(T)$ data. The samples were grouped into four different categories based on both known parameters from the sample deposition, and subsequent observations of characteristics, behaviour and morphology. Table 4.1 outlines and categorises the samples; the deposition condition parameters are defined in Section 3.5.1.

The primary delineation between sample groups is the temperature that they were deposited at. The first two groups of samples were deposited at room temperature ($\sim$ 300K), where coalescence has a large effect on the morphology. The second two groups were deposited at 10K, and coalescence was found to be negligible over the timescales of deposition. Figure 4.1 shows SEM images of samples deposited at both temperatures, and the morphology difference is clear. Samples deposited at 10K show much more granularity, with the individual clusters remaining distinct; the room-

	Deposition conditions					Initial sample properties				
Sample	T_{Dep}	Rate (Å/s)	t_{Dep} (s)	d (nm)	d_{adj} (nm)	R_N (Ω)	R(2K) (Ω)	T_c (K)	Bias	Behaviour
S1	RT	0.42	389	16.3	24.3	18.9 M	19.8 M	5.5	30 mV	SI
						11.6 k	2 k	5.58	30 mV	SC
S2	RT	0.34	364	12.4	18.4	1.2 k	217	6.4	30 mV	SC
S3	RT	0.3	419	12.6	18.7	47 k	32.8 k	6.66	30 mV	SC
S4	RT	0.236	721	17.0	25.3	353	182	6.65	30 mV	SC
S5	RT	0.16	450	7.2	10.7	132	6	6.68	100 nA	SC
S6	RT	0.259	1041	27.0	40.0	53.5	4	6.15	300 nA	SC
S7	RT	0.244	1144	27.9	41.4	92	5	6.0	500 nA	SC
S8	LT	0.271	1227	33.3	49.4	4.8 k	3.5	5.26	500 nA	SC
S9	LT	0.335	450	15.1	22.4	18.3 k	134	6.41	500 nA	SC
S10	LT	0.274	1285	35.2	52.3	70.45 k	7.75 k	5.63	500 nA	SC
S11	LT	0.26	737	19.2	28.4	885 k	925 k	6.08	60 nA	QR
S12	LT	0.391	950	37.1	55.1	7.3 M	9.2 M	6.0	5 nA	SI
S13	LT	0.39	1040	40.6	60.2	27 M	50 M	6.0	1 nA	SI

Table 4.1: Deposition conditions for the various samples, and initial sample characteristics (RT = room temperature ($\sim$ 300K), LT = low temperature (10K), SC = superconducting, QR = quasi-re-entrant, SI = superinsulating). $d_{adj} = 1.48d$ is adjusted for the imperfect coverage of the FTM crystal by the cluster beam (see Section 3.5.2).

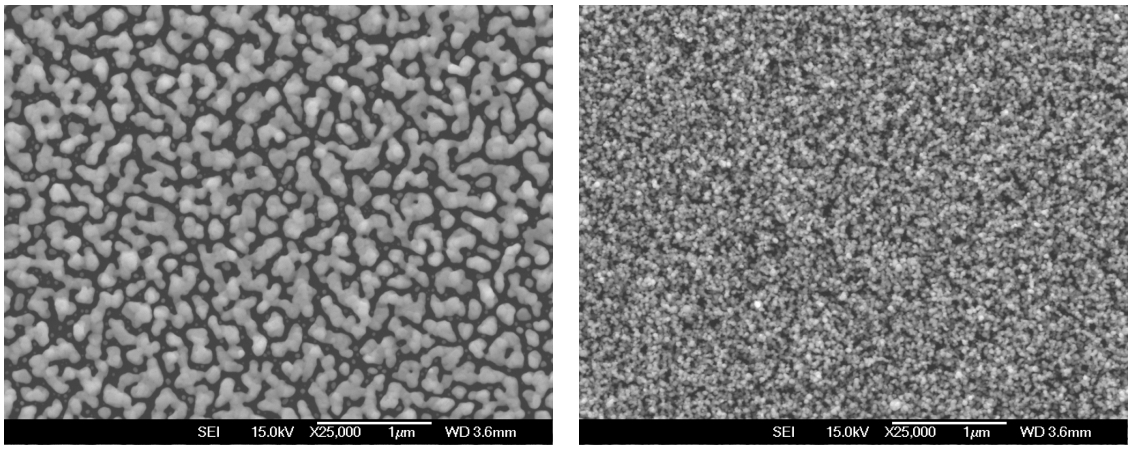

Figure 4.1: SEM images of samples (a) S6 from group 2, and (b) S8 from group 3.

temperature samples have undergone extensive coalescence, with the predominant feature being the islands rather than individual clusters. As noted in Section 3.5.3, the morphologies observed in the SEM images might not be completely accurate due to the possibility of coalescence during warming.

One of the main effects that coalescence has on the samples is to change the amount of material that needs to be deposited to reach onset. Without appreciable coalescence the clusters remain where they land, and so the onset of conductance is purely dependent on the two-dimensional film coverage of the sample exceeding some critical coverage (see Section 2.9 on percolation theory). On the other hand, coalescence of deposited clusters leads to a "beading up" effect where the coalesced islands tend to pull away from each other and become thicker, meaning that a higher amount of deposited material is required for the islands to connect and span the sample.

A second delineator is the level of oxidation. The clusters can be oxidised both in the source chamber and after landing in the deposition chamber. The first group of samples in Table 4.1 were deposited in the presence of an atmospheric leak, whereas for the subsequent sample groups the leak was removed. Figure 4.2 shows SEM images for the first sample group; compared to groups 2 and 3 (Figure 4.1), the first sample group more closely resembles the 10K-deposited samples. Coalescence is much lower in the first group of samples, due to the clusters being oxidised before they reached the deposition chamber; the oxide shell impedes the coalescence of the clusters.

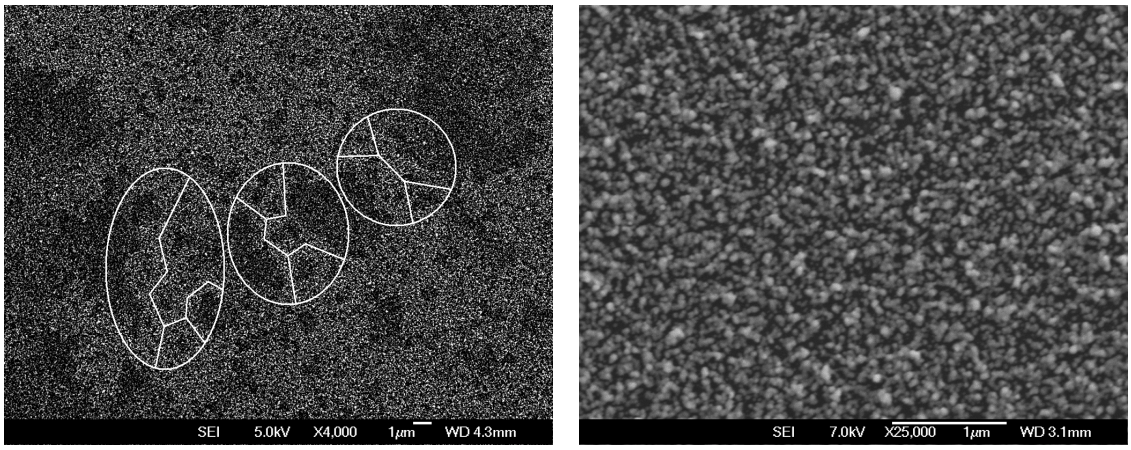

Figure 4.2: SEM images of group 1 samples (a) S1 and (b) S2. Three conduction pathways are visible in (a) (indicated in white).

Finally, the initial sample behaviour can be used to delineate sample groups. For the fourth group of samples, deposition was stopped soon after onset while the resistance was still high; these samples initially showed either quasireentrant or superinsulating behaviour (described in detail below), with the resistance increasing below T_c. All other groups of samples were superconducting to some degree after deposition.

4.2 Onset data

Valuable information can be obtained from the behaviour of the current through a sample during deposition (which was conducted with an applied potential bias of 30mV across the substrate). Figures 4.3 to 4.6 show examples of the onset behaviour for samples from the four different groups. There are several different behaviours evident across the sample groups in the post-deposition period. The onset graphs are plotted in terms of the conductance of the sample in units of the quantum conductance $G_0 = 2e^2/h$; these units are useful in nanoscale systems where quantum conductance may be relevant, as the conductance of a single quantum channel is $1G_0$ (assuming ballistic transport through the channel) [73].

Onset data from group 1 is shown in Figure 4.3. Samples onset to a conductance on the order of a few G_0 before deposition was halted. Post-deposition, the conductance steadily decreased but eventually tailed off to a stable value; this was interspersed with

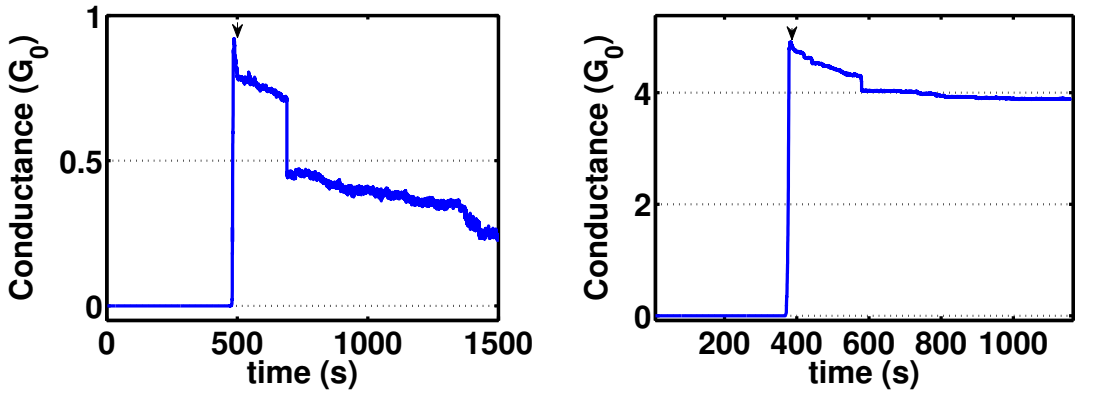

Figure 4.3: Onset of conductance for samples (a) S1 and (b) S2 from group 1. The arrows indicate when deposition was stopped.

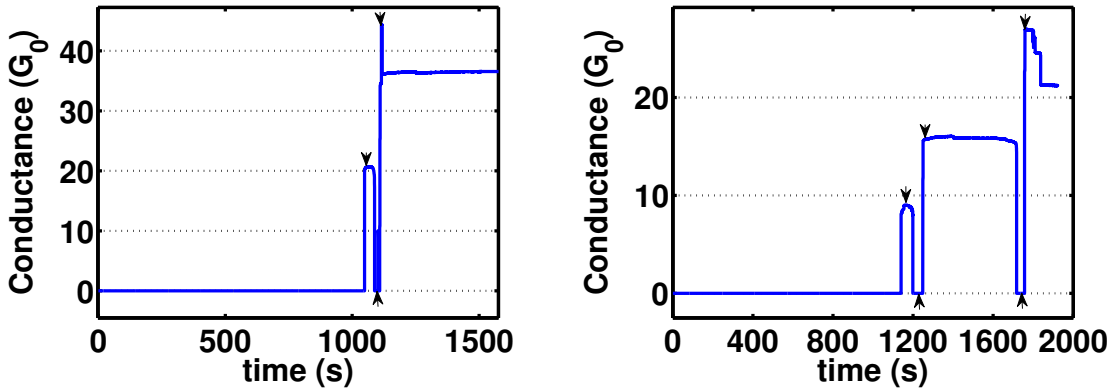

Figure 4.4: Onset of conductance for samples (a) S6 and (b) S7 from group 2. The arrows pointing down indicate when deposition was stopped; arrows pointing up indicate when deposition was restarted after a previous stop.

large discrete jumps to lower conductances. The group 2 samples (Figure 4.4) onset to large conductances (tens of G_0). They were also inherently unstable, and often broke within seconds or minutes of stopping deposition.

Figure 4.5 shows onset data from group 3, the first 10K group. Samples in this group were the most stable after deposition, showing very little deviation from the resistance at which deposition was halted. The group 4 samples were also reasonably stable after deposition (Figure 4.6). These samples were stopped at much lower conductances than

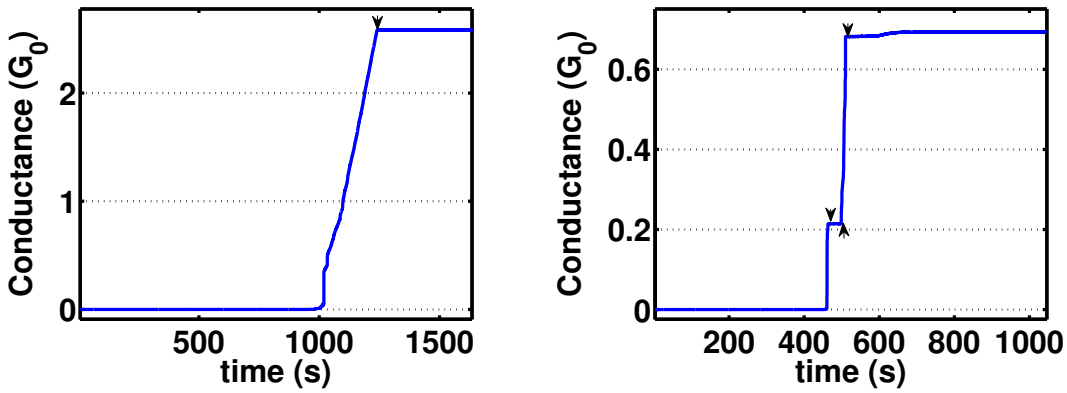

Figure 4.5: Onset of conductance for samples (a) S8 and (b) S9 from group 3. The arrows pointing down indicate when deposition was stopped; arrows pointing up indicate when deposition was restarted after a previous stop.

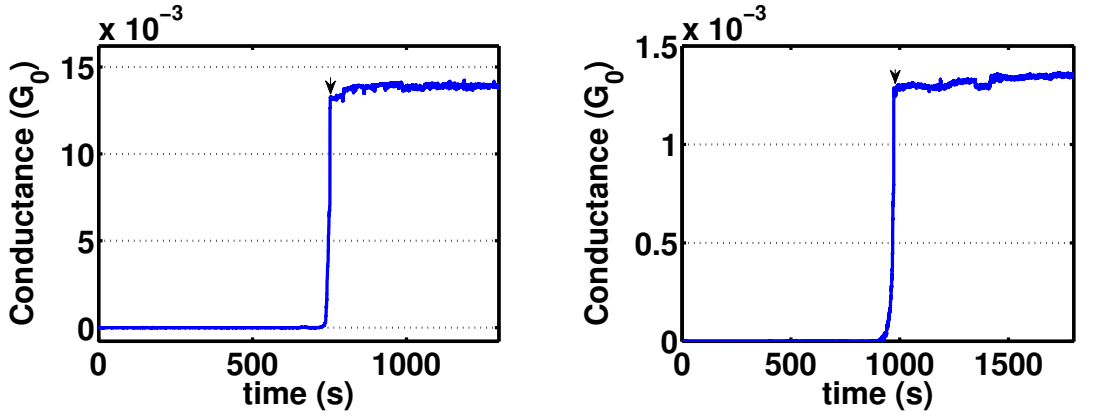

Figure 4.6: Onset of conductance for samples (a) S11 and (b) S12 from group 4. The arrows indicate when deposition was stopped.

the group 3 samples (by about a factor of 1000 in general).

The four groups described above exhibited varying onset behaviours, but the effects can be explained in terms of two factors - coalescence of the clusters within the samples, and oxidation of the clusters.

The high level of instability in the group 2 samples is consistent with the observed morphology of the samples (Figure 4.1(a)) - the "beading up" of the islands tends to pull them apart from each other, meaning that the connections between the islands will

become progressively thinner. The group 2 sample breakages are due to the "beading up" causing some critical connection between the islands to pull apart and break, or simply the fact that the cross-sectional area of some connection becomes small enough that localised Joule heating occurs, melting the connection.

Both 10K sample groups (3 + 4) exhibited high stability and minimal steps in conductance after deposition. The most obvious explanation for this is the lack of thermal energy and negligible (on a timescale of hours) coalescence; the clusters then remain where they land and the connections through the sample are the "necks" between clusters where they touch.

The samples in group 1 fell somewhat in the middle of the other groups in terms of onset characteristics - there is clearly some level of coalescence or cluster movement causing the decrease in conductivity, but the samples do stabilise after some time. This behaviour seems consistent with the idea that there are two competing factors affecting the resistance of the group 1 samples. Referring back to Figures 4.1 and 4.2, the group 1 samples were deposited both at room temperature and in the presence of oxygen. So while the rate of coalescence of pure lead clusters is high at room temperature (as shown in the group 2 samples), oxidation makes the individual clusters more stable, resulting in very little overall coalescence during sample deposition.

Figures 4.7 to 4.10 are magnified plots of the onset of conduction through to just after deposition was stopped, with conductance generally plotted on a log scale. Here also the different behaviours of the four groups are apparent.

The onsets for the group 1 samples (Figure 4.7) occur over a few tens of seconds (during the actual experiment, there was a delay of around six to ten seconds between noticing the onset and halting deposition). There are several large conductance jumps within the onset curves - these are likely caused when deposition of another cluster creates a new conduction pathway through the sample.

Figure 4.8 shows the magnified onsets from the samples in group 2. The samples onset almost instantly - the conductance increased by over six orders of magnitude within a few seconds. During the period between initial onset and the end of deposition there are discrete jumps in both directions (amidst the general trend of increasing conductance expected from continued deposition).

The onsets for the 10K samples from group 3 (Figure 4.9) are much more gradual than the room-temperature samples - for example, a conductance increase from $10^{-6}G_0$

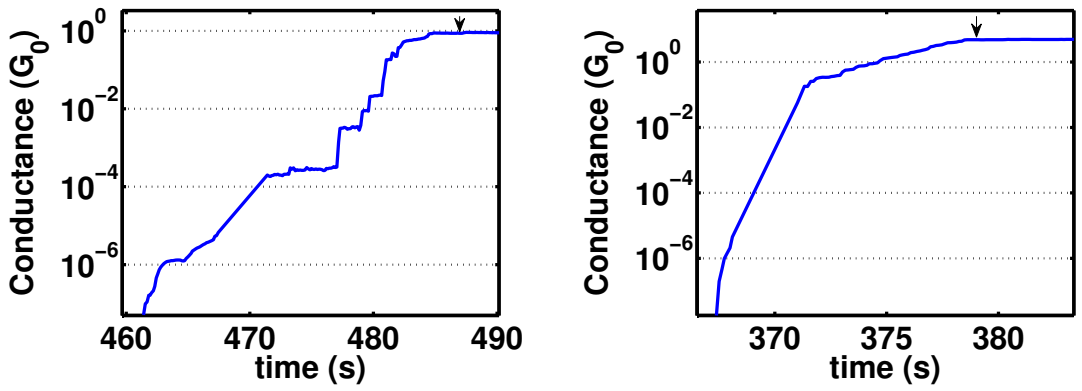

Figure 4.7: Magnified log-plots showing the onset of conductance for group 1 samples (a) S1 and (b) S2. The arrows indicate when deposition was stopped.

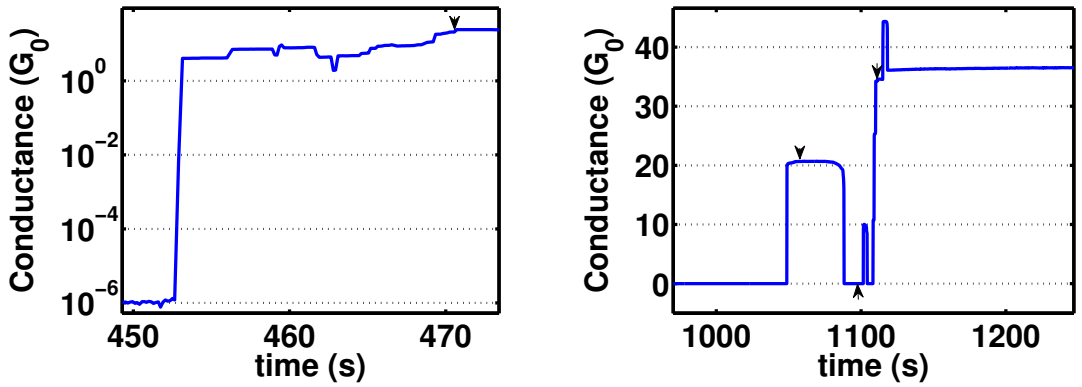

Figure 4.8: Magnified log-plots showing the onset of conductance for group 2 samples (a) S5 and (b) S6. The arrows pointing down indicate when deposition was stopped; arrows pointing up indicate when deposition was restarted after a previous stop.

to $10^{-4}G_0$ took 5 seconds for sample S1 from group 1, but 13 seconds for sample S9 from group 3. There are clear steps in the conductance similar to group 1, but the group 3 samples eventually enter a regime where the conductance increases very smoothly. Additionally, earlier on during the group 3 onsets more smaller conductance steps are visible than for the room-temperature group 1 samples (the group 2 samples onset so rapidly that no steps were visible at all).

Deposition of the group 4 samples was intentionally halted at a lower conductance

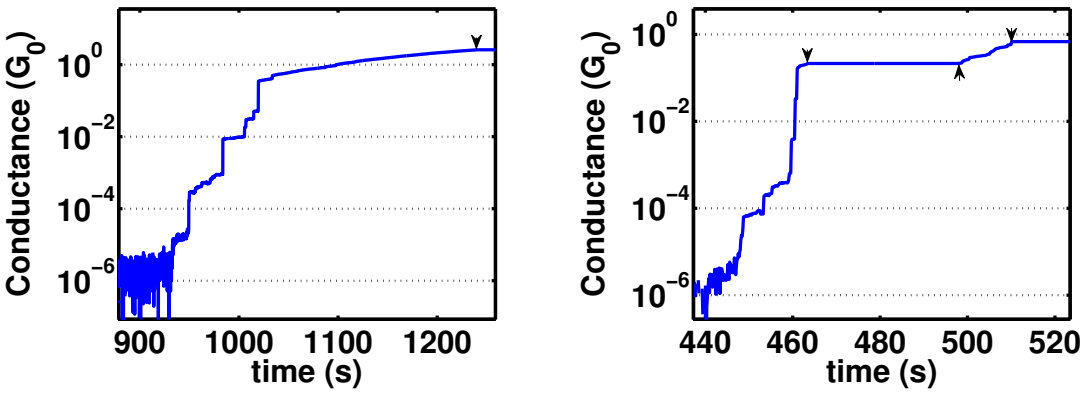

Figure 4.9: Magnified log-plots showing the onset of conductance for group 3 samples (a) S8 and (b) S9. The arrows pointing down indicate when deposition was stopped; arrows pointing up indicate when deposition was restarted after a previous stop.

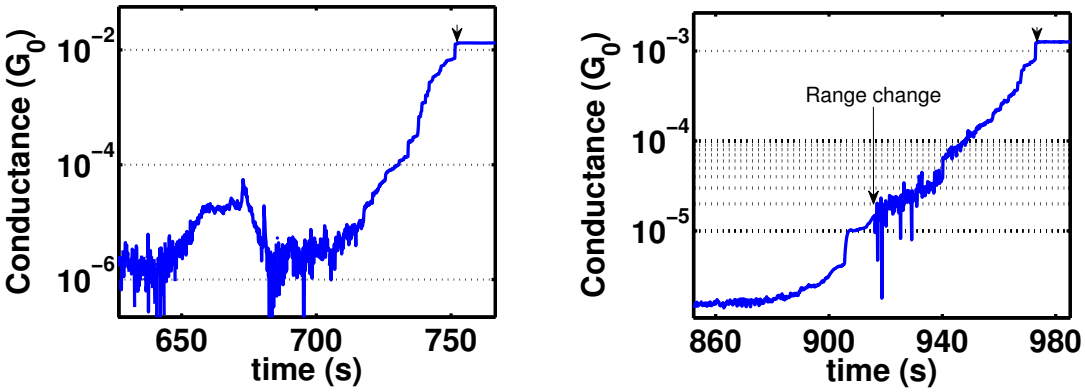

Figure 4.10: Magnified log-plots showing the onset of conductance for group 4 samples (a) S11 and (b) S12. The arrows indicate when deposition was stopped. The "range change" label points out when the current meter range was increased (and accuracy of measurement decreased), creating noise.

than the group 3 samples, in order to obtain different characteristic behaviour (as will be described in the next section). Figure 4.10 shows the onsets for some of the group 4 samples; the onset rates were similar to the early stages of the group 3 samples (ignoring the large discrete steps in conductance which occur randomly).

The behaviour observed in the magnified onset curves are consistent with the expla-

nations proposed for the overall curves. The negligible coalescence for the 10K samples explains both the relatively smooth onset curves and the presence of small steps - without the clusters being drawn away into islands, the samples are much closer to percolating systems, for which such behaviour is expected.

The rapid onset of conductance for group 2 is again consistent with a high level of coalescence. The islands formed by the clusters tend to keep isolated while reaching sizes many times greater than the size of the incident clusters; thus when a pathway does form between islands, the average cross-sectional area of the path is already very high, so the initial onset condutance will follow suit.

The post-onset curves for group 1 support a model where the expected room-temperature coalescence of clusters (as seen in group 2) is greatly slowed by oxidation of the clusters. The "islands" in the group 1 samples have a higher degree of coalescence than those in groups 3 and 4, but nowhere near that of group 2; this gives rise to the observed intermediate behaviour.

The presence of more small steps in the group 3 samples compared to those in group 1 is likely due to the difference between an intrinsically low coalescence rate in the group 3 samples (due to the substrate being at 10K), and an artificially low coalescence rate in the group 1 samples (due to oxidation). In the group 3 samples, deposited clusters would have an immediate effect on the local conductivity due to the additional lead-lead connections; the oxidised clusters deposited on the group 1 samples would at first be insulated from the rest of the sample by the oxide shell (which has a much lower conductivity than pure lead [74]) and their contribution to the conductivity would slowly increase as the clusters coalesced and pure lead necks formed.

Although the major focus of this thesis is on samples which are close to or above the percolation threshold (and hence have reached onset), it is interesting to note that the region before onset is not devoid of features. Figure 4.11 is a log-scale plot of the deposition conductance before onset for one of the 10K samples (sample S12). About half-way before onset occured, there is a noticeable increase in the conductance of the sample. This behaviour was not observed in samples from the other groups because the range the current meter was operating on (when depositing those samples) was too high to detect such small changes. If the onset of conductance is assumed to occur at the theoretical coverage of $\rho_c = 0.68$ then the increase in pre-onset conductance occurs at $\rho \approx 0.30$ (assuming that the coverage increases linearly with time).

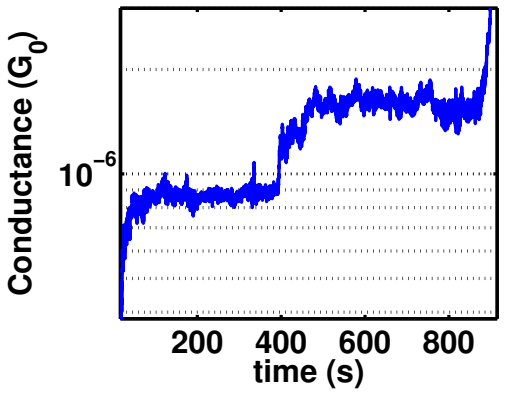

Figure 4.11: Magnified plot of the pre-onset conductance for sample S12.

4.3 $R(T)$ data

4.3.1 Initial behaviour after deposition

Samples created in the experimental setup described in the previous chapter change and degrade over time. The system does not operate at UHV pressures, and so the small quantity of air in the system oxidises the samples (on a timescale of days). Additionally, as described in previous sections, the sample morphologies change over time due to coalescence of the clusters, though this is slowed both in the presence of oxidation and at low temperatures. Consequentially, the initial measurements taken just after deposition will correlate more closely to the deposition conditions and onset data than later data sets.

The initial sample properties in Table 4.1 were taken from the initial $R(T)$ data. The critical temperature T_c is defined (both here and below) as the temperature of the inflexion point of the $R(T)$ curve. The normal-state resistance R_N is defined as the resistance above T_c, and is generally measured at $\sim 7 - 8$K. Two sets of initial sample properties are given for sample S1; this is because the sample showed superresistive behaviour in the first $R(T)$ measurement made after cool-down, but the following measurement (and all subsequent measurements) showed superconductive behaviour, so S1 was classed as a superconducting sample.

Figures 4.12-4.16 show $R(T)$ curves from the four different sample groups. The measurements for groups 3 and 4 were made within an hour of deposition, because

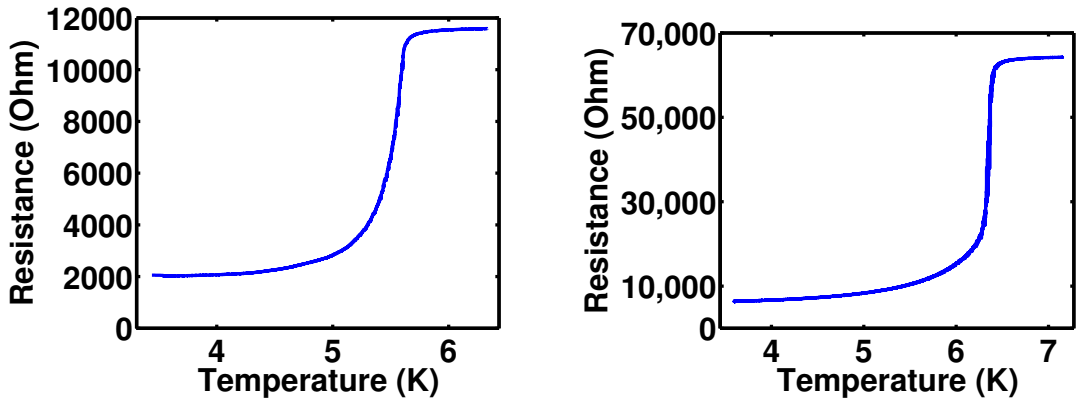

Figure 4.12: $R(T)$ graphs for samples (a) S1 and (b) S2 from group 1, with an applied bias of (a) 30mV and (b) 470nA.

the samples were already at 10K. However groups 1 and 2 were deposited at room temperature, and there was a period of around 20 hours (during which the samples were cooled down to superconducting temperatures) before $R(T)$ measurements could be made. There are general differences in character of the curves across the groups.

$R(T)$ graphs from the first group of samples are shown in Figure 4.12. Interestingly these samples do not show the superconducting behaviour expected from bulk superconductors - the samples have no sharp resistance change at the superconducting transition. Instead the samples exhibit large resistive tails below T_c which flatten off below $\sim 0.7T_c$ to large non-zero resistances.

Figure 4.13 shows $R(T)$ graphs for sample S5 from group 2 at two different bias currents. This sample shows a resistive tail similar to that observed for the group 1 samples, but the resistance range here is orders of magnitude lower, reaching 6Ω at the lowest-measured temperature. The two resistance curves both show instabilities, though they appear to be suppressed on the curve measured at higher bias current. Similar instabilities were observed in the $R(T)$ curves for sample S4.

Figure 4.14 shows $R(T)$ graphs for samples S6 and S7. The resistive tails observed previously do not appear here; instead, the sample resistances decrease to $\sim 2\Omega$ by $0.95T_c$. However zero resistance is still not reached, and instead the resistance increases again to $\sim 4\Omega$ before levelling off, forming a "resistive dip" just below T_c.

Both resistance dips just below T_c (Figure 4.15(a)) and low temperature resistive

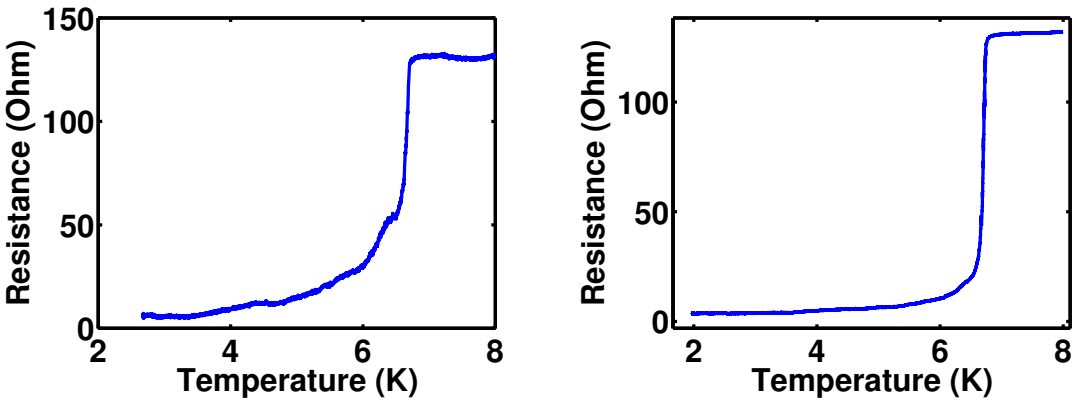

Figure 4.13: $R(T)$ graphs for sample S5 from group 2, with an applied bias of (a) 100nA and (b) 500nA.

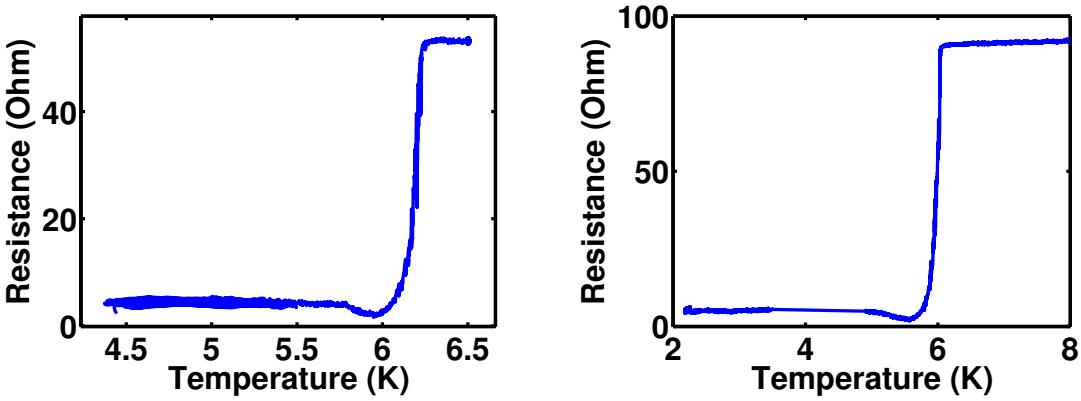

Figure 4.14: $R(T)$ graphs for samples (a) S6 and (b) S7 from group 2, with an applied bias of (a) 300nA and (b) 500nA.

tails (Figure 4.15(b)) are observed in the third group of samples. Qualitatively, the curves match the observations from the first two groups - the shapes of Figure 4.12(b) and Figure 4.15(b) are very similar, as are Figure 4.14(b) and Figure 4.15(a). The scales of the curves are not similar however; the ratios between the normal-state resistance and the low-temperature resistance for the group 3 samples are ~ 9, ~ 137 and ~ 1400, compared to $\sim 1.4 - 20$ for groups 1 and 2.

As stated in the previous section, the depositions on the fourth group of samples were halted at lower conductances than the group 3 samples. As such, the group 4

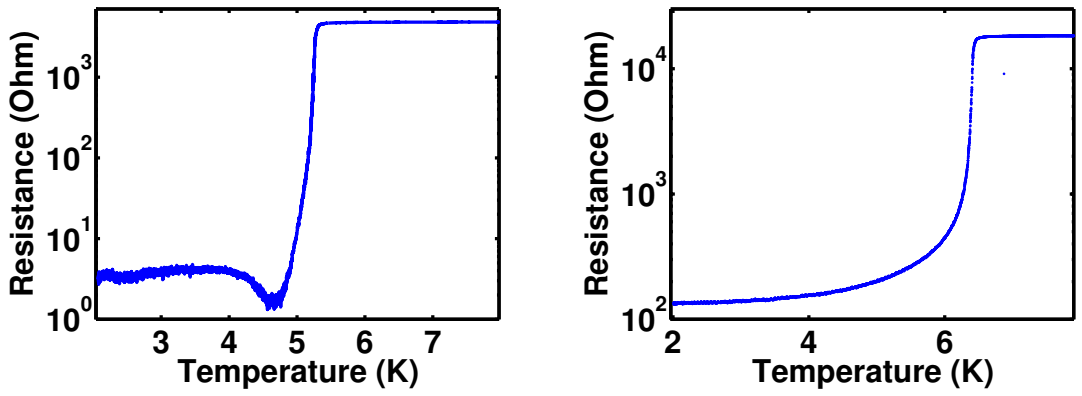

Figure 4.15: Initial $R(T)$ graphs for samples (a) S8 and (b) S9 from group 3, with an applied bias of 500nA.

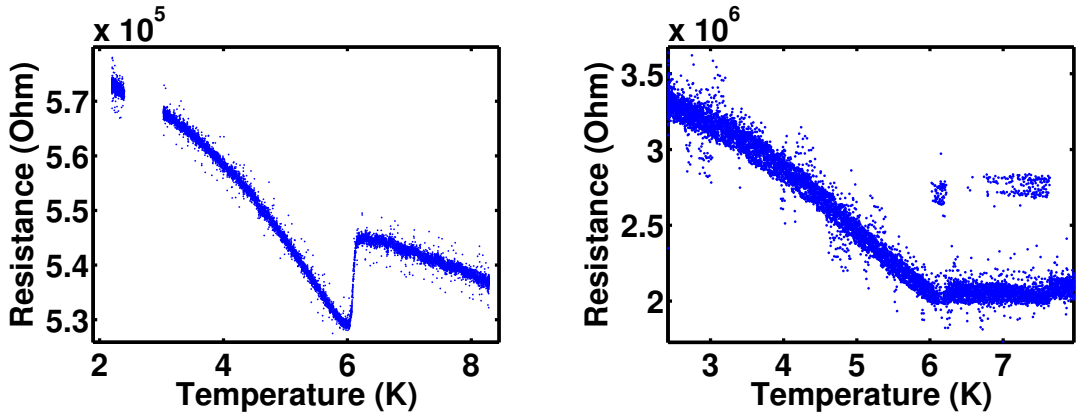

Figure 4.16: Initial $R(T)$ graphs for samples (a) S11 and (b) S12 from group 4, with an applied bias of (a) 60nA and (b) 5nA.

samples all had much higher normal-state resistances. They also all exhibited superresistive behaviour - the resistance at low temperatures was higher than the normal-state resistance, and a transition at T_c was still visible. While the resistance of some samples only increased below T_c (Figure 4.16(b)), others first exhibited a dip in resistance below T_c before beginning to increase (Figure 4.16(a)).

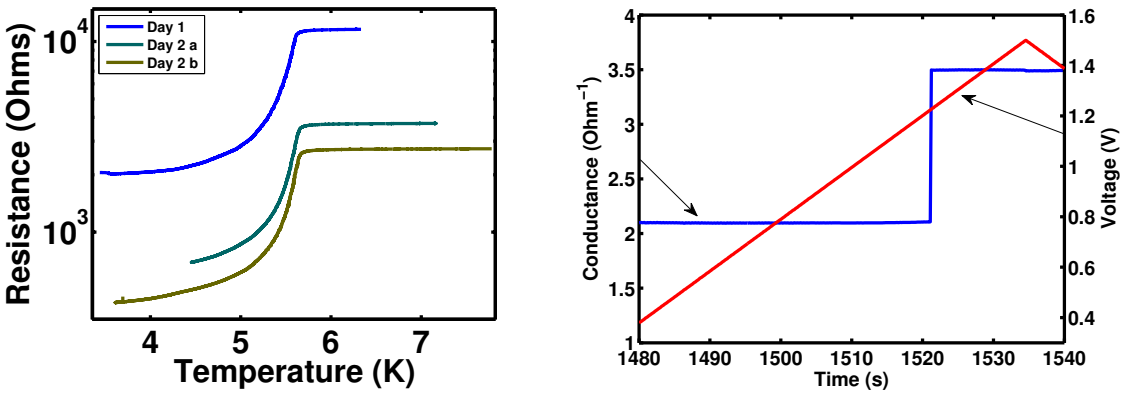

Figure 4.17: (a) Progressive changes in the $R(T)$ curves for sample S1 from group 1. (b) The voltage ramp which caused the first jump in resistance.

4.3.2 Evolution of sample characteristics

While some of the samples were stable enough after deposition to exhibit the same $R(T)$ behaviour throughout subsequent measurement over several days, many of the samples underwent irreversible changes during that time. Some changes were bias-driven, caused by temporarily applying a large bias to the sample; others were due to progressive coalescence of the samples over time. There were also changes in $R(T)$ that could be induced by varying the bias current without altering the sample structure. Examples of all three situations are given below.

Figure 4.17(a) shows $R(T)$ curves measured on sample S1 at different times over two days. The temperature of the sample reached a maximum of only 14.5K overnight, but the normal-state resistance of the sample had dropped from its initial value of 11.6kΩ (taken from above T_c on the Day 1 curve in Figure 4.17(a)) to 6.2kΩ the next morning. Before each of the two temperature curves on day 2, a progressive voltage ramp was applied to the sample to attempt to change the behaviour; a jump to 3.7kΩ was observed at 1.2V (Figure 4.17(b)), and then later a jump to 2.7kΩ at 0.65V (after ramps up to 5V). The applied voltages caused decreases in the resistance, but barely any shift in the critical temperature. Additionally, the behaviour below T_c remained unchanged and the shape of the $R(T)$ curves did not change on the log plot.

Figure 4.18 shows $R(T)$ curves from samples S8 and S9 taken over several days to examine the effect of post-deposition coalescence on sample behaviour. Between day

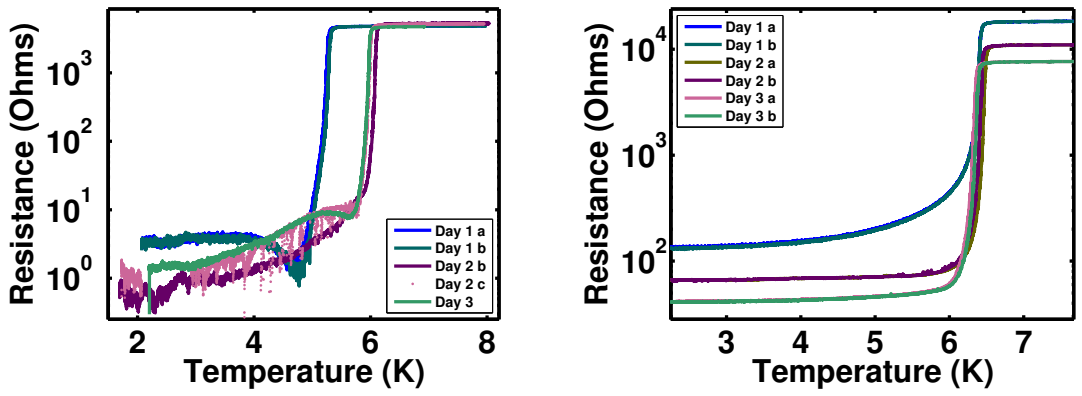

Figure 4.18: Changes to $R(T)$ behaviour over the three-day measurement period for samples (a) S8 and (b) S9 from group 3. All measurements were made with a bias current of 500nA.

1 and day 2 the samples reached a temperature of 89.3K, and between day 2 and day 3 they reached 199K. There are clear differences across the three-day measurement window.

Sample S8 maintained the same normal-state resistance across the entire measurement period, but there was a large shift in critical temperature between the first and second days of measurement. The behaviour below T_c also varied, evolving from a resistive dip to a resistive tail, and then a combination of both on the last day. Sample S9 on the other hand showed very little change in T_c, and instead exhibited a decrease in both normal-state and low-temperature resistance. The resistive tail also flattened out and the superconducting transition became sharper, though a non-zero resistance at low temperature was still observed. The origin of these effects will be discussed in Section 4.5.1.

In addition to the above irreversible changes, reversible variations in the $R(T)$ curves were observed. Figure 4.19 shows, as a function of applied bias current, changes to the conducting characteristics of sample S12. $R(T)$ curves were taken at bias currents starting at 10nA and increasing up to 200μA. There is a clear evolution of the sample characteristics, from superresistive behaviour at low currents to superconductive behaviour at the highest measured current. $R(I)$ curves from S12 will be shown in Figure 4.26 which clearly show the reversibility of this current-induced resistance evolution.

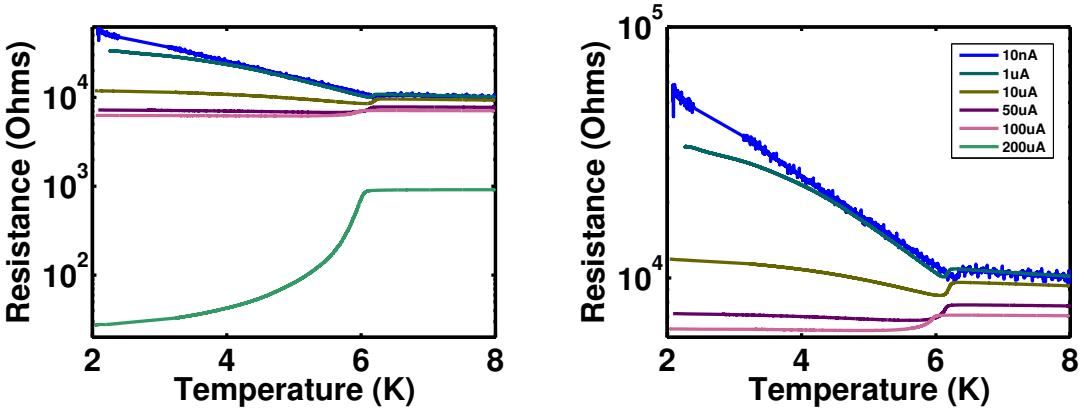

Figure 4.19: Changes to $R(T)$ behaviour as a function of applied bias current for sample S12 from group 4, on two different scales.

None of the measured $R(T)$ curves show an absence of a transition, implying that the critical current I_c of the sample has not been reached.

4.4 $V(I)$ data

In addition to the resistance versus temperature measurements of the previous section, $V(I)$ data was also collected for many of the samples studied. Each set of measurements gives a different view into the processes going on within the samples, and so both are equally important. The majority of the data was collected by ramping the current in a triangle wave pattern, starting from zero and increasing towards a positive limiting current, then down through zero to the maximum negative current, and back to zero. For clarity, the figures below predominantly show only the down ramp data (from highest positive current to highest negative current) - the up ramp data is almost always identical (after an appropriate reversal of current polarity).

4.4.1 $R(I)$ graphs

While the raw data measured is voltage data rather than differential resistance data, plotting $R = V/I$ against the bias current helps glean valuable insight into the behaviour of the samples. Figure 4.20 shows $V(I)$ curves from sample S3, measured at varying temperatures below T_c - even on a log-log scale, the major features are not

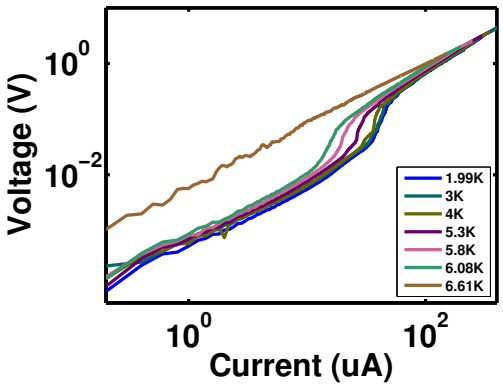

Figure 4.20: $V(I)$ curves at various temperatures for sample S3 from group 1.

noticeable. Figure 4.21(c) shows the corresponding $R(I)$ curves from sample S3; several features are much more prominent. The first observation that can be made is that there is a clear global I_c for the sample which decreases as the sample temperature increases, and above which the current follows a well-defined curve at all measured temperatures; this is consistent with the $R(T)$ behaviour discussed in Section 4.3 and the overall critical current I_c of the sample becoming smaller as the temperature is increased towards T_c. There are several other, more interesting features:

- *Non-zero intercept* - Figure 4.21(d) shows the low-current region of the $R(I)$ curve, and the resistance does not go to zero at zero applied current for any temperature. This agrees with the observed $R(T)$ behaviour.

- *A "resistive shoulder"* - for increasing $|I|$, the general trend is for the resistance to increase very slowly for a period, then rapidly increase, and then slowly until the sample fully transitions to the normal state (Figure 4.21(c)). This behaviour persists as the temperature increases towards T_c.

- *Non-linear smooth steps* - The resistance does not increase uniformly as $|I|$ increases, but evolves through gradual rolls or "steps" (Figure 4.21(d)). These steps only seem to appear at low $|I|$; they also become less prominent and eventually disappear as the temperature increases towards T_c.

- *Discrete steps* - Not to be confused with the above smooth steps, there are noticeable discrete jumps in the resistance as $|I|$ increases. These do not occur at

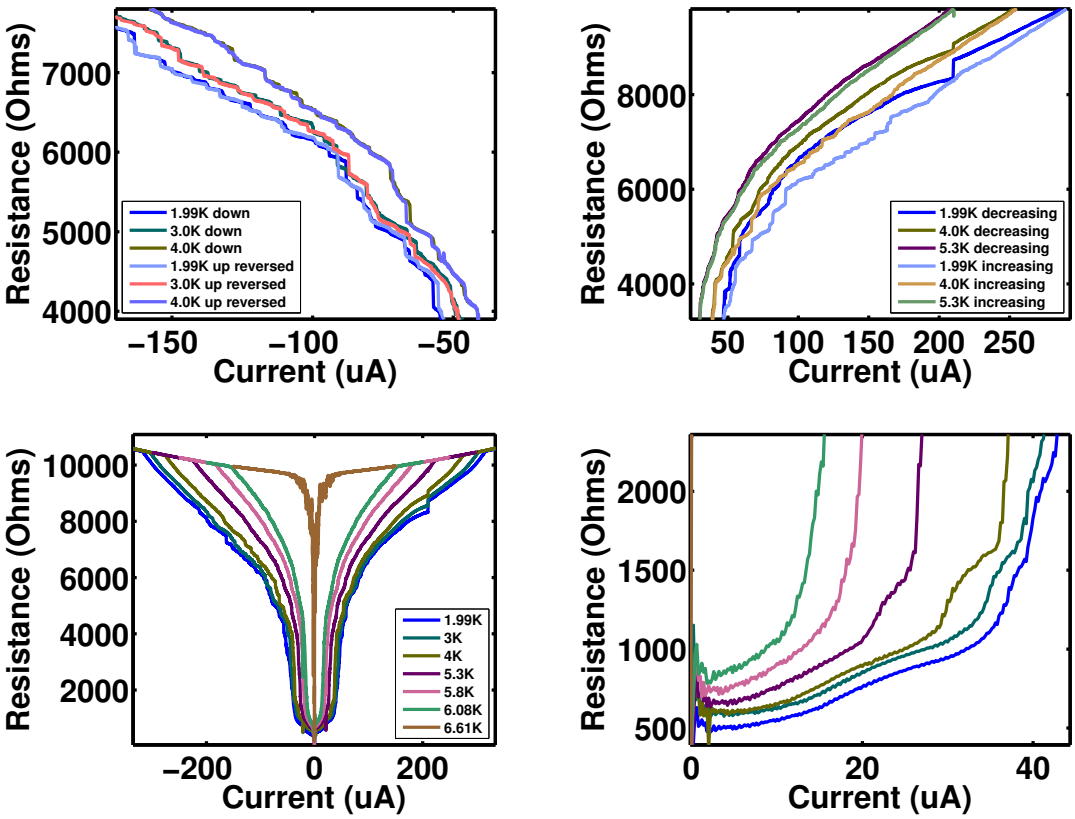

Figure 4.21: $R(I)$ curves at various temperatures for sample S3 from group 1, showing (a) discrete steps repeatable on increasing $|I|$, (b) hysteresis between increasing and decreasing $|I|$, (c) an overall view and (d) smooth steps at low I. The large discrete jump in all current curves at 200μA is not real, but an artifact caused by the current meter changing range.

low currents, but become apparent further away from zero bias. Figure 4.21(a) shows a section of the $R(I)$ curves with both up and down ramps plotted; the currents for the up ramp (consisting of the two triangle-wave sections from zero to highest positive current, and highest negative current to zero) have been multiplied by -1 to account for the polarity difference. Some of the larger discrete steps can be identified across multiple temperatures, while others (in particular the smaller steps) show no such correlation. There is, however, a clear correlation between the up and down ramps, indicating that most of the steps are caused by repeatable phenomena rather than being random noise. Smooth and discrete

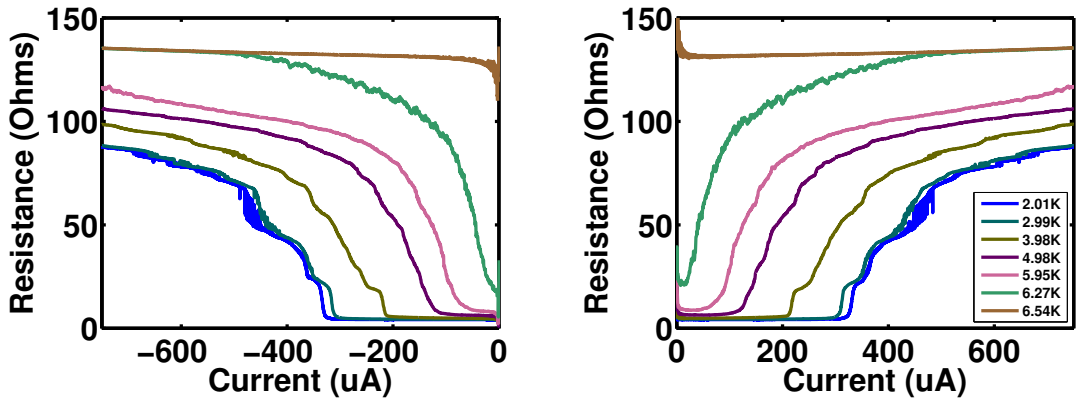

Figure 4.22: $R(I)$ curves (down current ramp shown) at various temperatures for sample S5 from group 2.

steps will be discussed in detail in Section 4.5.3.3.

- *Hysteresis* - There is a noticeable difference in the shape of the current curve depending on whether the magnitude of the bias current is increasing from zero or decreasing towards zero. Figure 4.21(b) shows a section of the $R(I)$ curves with both up and down ramps plotted, and the hysteresis is clear; when $|I|$ is decreasing, the resistance evolution is much smoother than when $|I|$ is increasing. The resistance also tends to be higher on the down ramp than the up ramp. Hysteresis will be discussed in detail in Section 4.5.3.2.

Figure 4.22 shows $R(I)$ curves at different temperatures for sample S5 from group 2. The characteristics observed above for a group 1 sample are also apparent here, though there are notable differences. The smooth "steps" are much more pronounced, though they still disappear as the temperature increases. The current range over which the resistance changes is also considerably larger; this is consistent with the view established in Section 4.1 that the superconducting pathways in the group 2 samples have much larger cross-sectional areas, and hence higher critical currents across the sample. Discrete stepping is not as noticeable in this sample, though the lower normal-state resistance of $\sim 130\Omega$ precludes resistance jumps of tens or hundreds of ohms (such as were observed in sample S3).

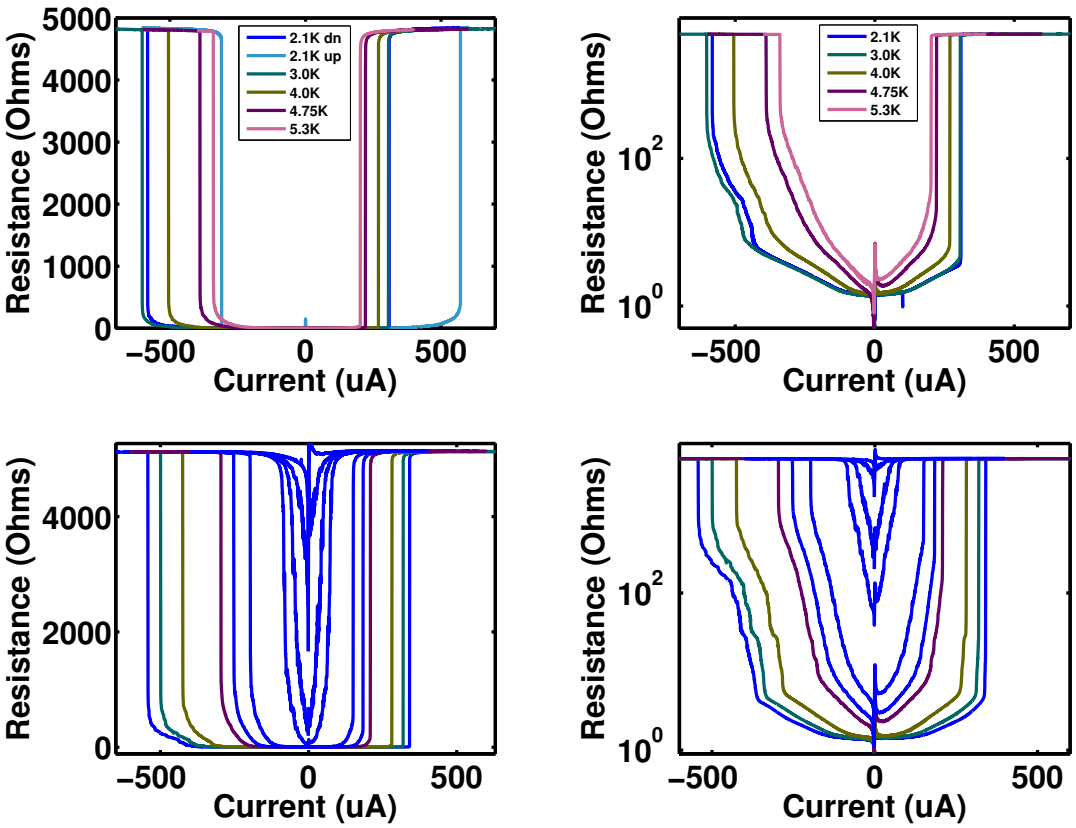

Figure 4.23: $R(I)$ curves (down current ramp shown) at various temperatures for sample S8 on (a) (b) day 1 and (c) (d) day 2 of measurement, plotted on (a) (c) normal and (b) (d) log scale. The 2.1K up current ramp is shown in (a) to emphasise the hysteresis.

Figure 4.23 shows $R(I)$ curves for sample S8 from group 3. This sample appears to exhibit very different behaviour from the first two groups - there is huge hysteresis between increasing and decreasing $|I|$. The bias current required to put the entire sample into the normal state (on increasing $|I|$) is approximately double the current at which the normal state transitions back to superconducting (on decreasing $|I|$), and the transition from one to the other appears very sharp. However, for regions of the $R(I)$ curve where the sample is not completely in the normal state (visible on log-scale plots such as Figures 4.23(b) and 4.23(d)), characteristics can be identified that are common with the prior two sample groups:

- *The presence of a shoulder* - while obscured on decreasing $|I|$, the slow-fast-slow

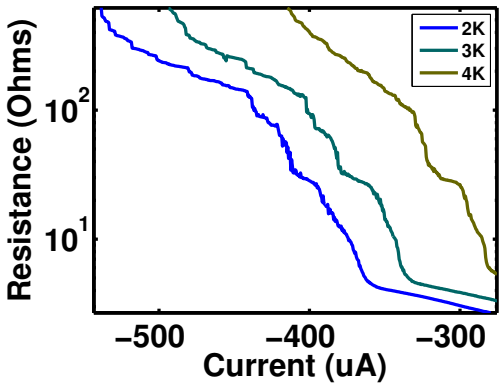

Figure 4.24: Magnified plot of Figure 4.23(d) showing stepping in the region of increasing $|I|$.

resistance evolution is apparent for increasing $|I|$, at least until the rapid transition to the normal state. The effect seems to disappear in the day 1 measurements with increasing T, but does not do so for the day 2 measurements.

- *Smooth steps* - the lower half of Figure 4.24 shows the smooth steps observed in the first two groups, and Figure 4.23(d) shows that the steps also disappear on increasing temperature.

- *Discrete steps* - as shown in the upper half of Figure 4.24, in the low resistance regimes there is still instability and discrete steps, some of which can be correlated across the different temperatures.

Figure 4.25 shows $R(I)$ curves for sample S11 from the fourth group. The behaviour here is clearly different from anything in the previous three groups. The resistance peaks around zero current, and smoothly tails off towards the normal-state resistance as $|I|$ increases. The zero-bias resistance also decreases towards the normal-state resistance as the temperature is increased (which is consistent with the $R(T)$ curves observed for group 4. No steps of any kind are observed.

One interesting feature is that there is a cross-over of the $R(I)$ curves at about $|20|$ nA - for bias currents below this current, the resistance purely decreases towards the normal-state resistance as the temperature increases, whereas above this current the resistance decreases below the normal-state resistance and then increases again as

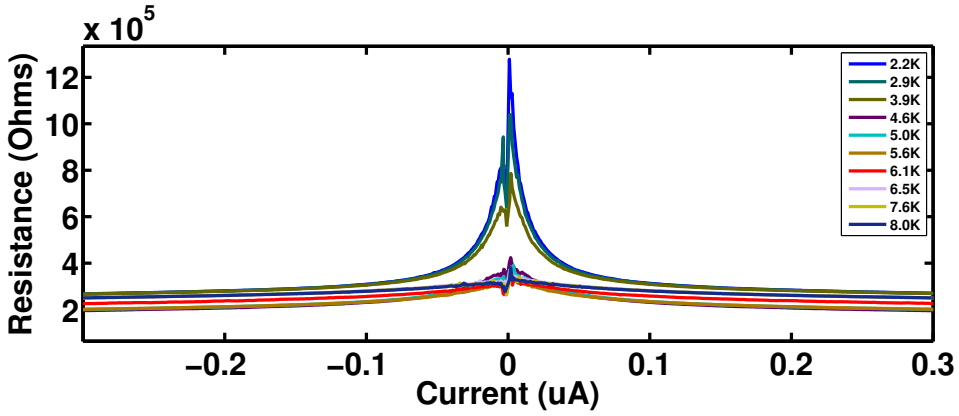

Figure 4.25: $R(I)$ curves (down current ramp shown) at various temperatures for sample S11 on day 2.

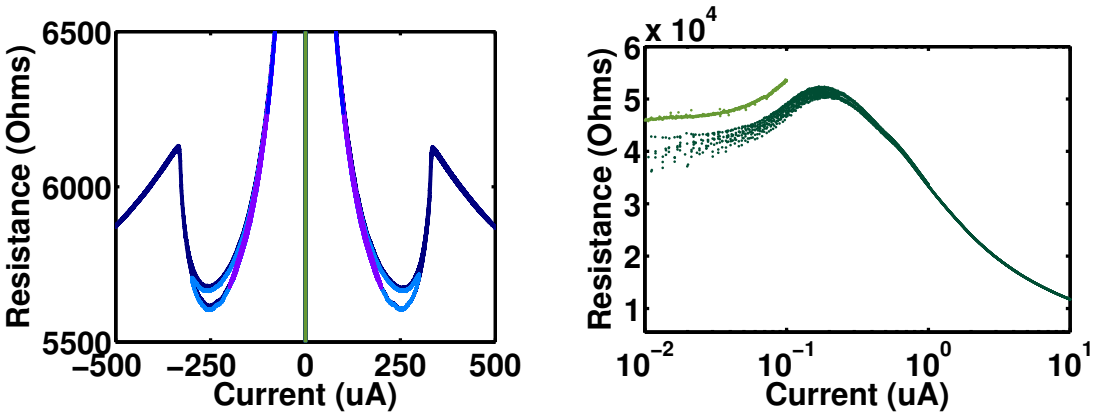

Figure 4.26: Multiple $R(I)$ curves at 3.05K for sample S12 on day 2; (b) depicts the central region of (a). The light green curve in (b) was measured more slowly, with ten times as many data points as the dark green curve over the same interval.

T is increased. This would appear to be evidence in $R(I)$ data of the "resistive dip" observed for sample S11 in Figure 4.16.

Figure 4.26 shows $R(I)$ curves for sample S12. Multiple curves were measured at the same temperature but to different maximum bias currents. The offset observed in Figure 4.26(b) between the light and dark green curves is an artifact of the sample temperature differing slightly between measurement runs. There appears to be a resistance plateau very close to zero bias current, with a resistance increase at slightly

higher currents.

As $|I|$ is increased further, there is a clear drop in the resistance of the sample before it recovers and then transitions to the normal state as the critical current is surpassed (Figure 4.26(a)). This behaviour matches the evolution of the sample S12 $R(T)$ curves exhibited in Figure 4.19. As with sample S11, no steps of any kind are observed. However, there is evident hysteresis in Figure 4.26(a). The dark blue and light blue curves exhibit a higher resistance on decreasing $|I|$ than on increasing $|I|$; no hysteresis is observed in the purple curve, suggesting that there is a minimum current required to observe the hysteresis.

4.5 Analysis and discussion

The onset data for the four sample groups was discussed in the previous section, and the interesting features were shown to be consistent with the different morphologies of the samples due to the interplay between the rate of coalescence of the clusters, and their level of oxidation.

The $R(T)$ and $V(I)$ measurements exhibited a number of interesting features which have yet to be discussed. Several questions arise from the above examination of the data:

- Why do the samples nearly all have non-zero resistances at low temperatures?
- Why are there differences in the low-temperature $R(T)$ characteristics?
- What causes the discrete steps? Why do they not occur at low currents?
- What causes the smooth steps? How are they different from the discrete steps?
- Why are there varying degrees of hysteresis? Why is there hysteresis at all?

The following sections will attempt to provide answers to these questions by a building a cohesive picture involving several of the models from Chapter 2 to explain the above observations.

4.5.1 $R(T)$ discussion

Resistances predicted by quasi-one-dimensional models will tend to be larger than the corresponding measured resistances - this is because there are often multiple parallel pathways through the samples. For example, in Figure 4.2(a) three such pathways are discernible for sample S1; potentially there could have been more, but no other pathways were observed in the SEM images (though possible coalescence of the sample during warming could have caused pathways to break). So even if each individual pathway is treated as quasi-one-dimensional, any resistance contribution from a particular pathway will be observed in parallel with other paths. While this would affect the observed resistance in any measurement, it would be more noticeable in the $R(I)$ curves where phenomena localised to specific individual pathways and dependent on the applied current are observed (like the smooth and discrete steps, which will be discussed further in Section 4.5.3.3).

A wide range of $R(T)$ behaviours were observed across the four sample groups, and in some cases within the groups.

The resistive tails observed in the group 1 samples appear consistent with those which are exhibited in the literature and attributed to phase slips [33, 34]. The resistance decrease below T_c is much more gradual than would be expected for a pure TAPS models (Sections 2.3.2 and 2.3.3), leading to the conclusion that QPSs are also present. Fits to several phase slip models in the following section will show that phase slips are consistent with the observed data.

Given the amount of material that was deposited in order to obtain stable samples in group 2, the samples would be expected to be closer to bulk superconducting behaviour. However, this is not entirely the case. The samples do have lower resistances below T_c than the group 1 samples, but they also have lower normal-state resistances; the latter is consistent with the higher degree of coalescence in the group 2 samples, as the cross-sectional area of the conducting pathways will be larger.

The cause of the instabilities observed in samples S4 and S5 (Figure 4.13) is unknown, as none of the models previously discussed exhibit that behaviour. One potential reason could be that the critical temperature within those particular samples differed with location, and the instabilities are in fact different regions of the sample progressively becoming superconducting; this could in turn be caused by inhomogeneities

within the cluster beam or the deposited film. The instabilities were only observed in two samples however - the other group 2 samples produced in the same manner showed no such effects. Given the statistical nature of sample production, reproducing such behaviour intentionally would prove difficult.

Samples S6 and S7 from group 2 (Figure 4.14)) exhibited a very low ($\sim 4\Omega$) residual resistance at low temperatures, which might have been written off as an offset due to the electronic setup. However, as mentioned previously it is not uniform - there is a noticeable dip in the resistivity just below T_c (down to $\sim 2\Omega$). Such a dip would not occur if the flat resistance below T_c was purely caused by an undesired series resistance in the measurement circuit.

The $R(T)$ behaviour of groups 3 and 4 is consistent with the superresistive behaviour discussed in Section 2.2. In particular, the resistive dips observed in the group 4 samples are akin to the behaviour labeled in the literature as quasi-re-entrant [10]. The literature is unclear as to the cause of this behaviour; the commonly-cited view [10, 13] is that there is localised pairing of electrons within individual islands, but no global phase coherence of the superconducting order parameter. As islands of connected clusters begin to form during deposition, conductivity results from quantum-tunneling of electrons between islands; as the coverage increases and more islands join up, the majority of conduction occurs through physical connections across the sample.

Whether quasi-re-entrant behaviour can explain the resistive dips observed in groups 2 and 3 is unclear. Certainly a resistive dip at such a low fraction of the normal-state resistance has not been mentioned in the literature - generally the dips are observed when the non-zero resistance close to 0K is at least half of the normal-state resistance [10, 12]. By contrast, the dips observed here occur in samples with resistances at 2K of $0.1R_N$ or less. As mentioned above, non-zero resistances below T_c are often attributed to phase slips and so it could be proposed that the dip results from an interplay between TAPSs and QPSs where there is minimum in an intermediate region - the TAPS rate has a maximum very close to T_c and is zero at 0K, while the QPS rate is non-zero at 0K. In the following section, fits to the phase slip models will be shown which give qualitative support to this proposition.

Irreversible changes to the $R(T)$ curves for samples S8 and S9 were observed when the samples were allowed to warm overnight. Assuming that phase slips were the cause of the observed non-zero resistance in the superconducting regime, the decreases in the

resistance of sample S9 can be explained by gradual coalescence within the sample as it warmed up overnight, widening the necks between islands which would both raise the normal-state resistance and decrease the likelihood of phase slips occuring there (relative to other regions in the film). The increase in T_c observed in sample S8 is not as easy to explain, but could potentially be interpreted as coalescence-driven morphology changes shifting the film slightly closer to bulk behaviour. Such morphology changes might also explain the change in $R(T)$ characteristics below T_c for sample S8.

4.5.2 $R(T)$ fits

In this section, some of the theoretical models covered in Chapter 2 are fitted to the obtained $R(T)$ graphs. The following models were chosen to be fitted:

- *Phase slips*
  - *TAPSs*
    - Little - Equation 2.18
    - LAMH - Equation 2.19
  - *QPSs*
    - GZQPS - Equation 2.36
    - KQPS - Equation 2.38
- *Vortices* - the BKT transition can be fitted to $R(T)$ data via the HN formula (Equation 2.54).

Fitting of theoretical models to $R(T)$ data was done using the Matlab curve fitting toolbox. In order to obtain fitting parameters that had some physical meaning, the

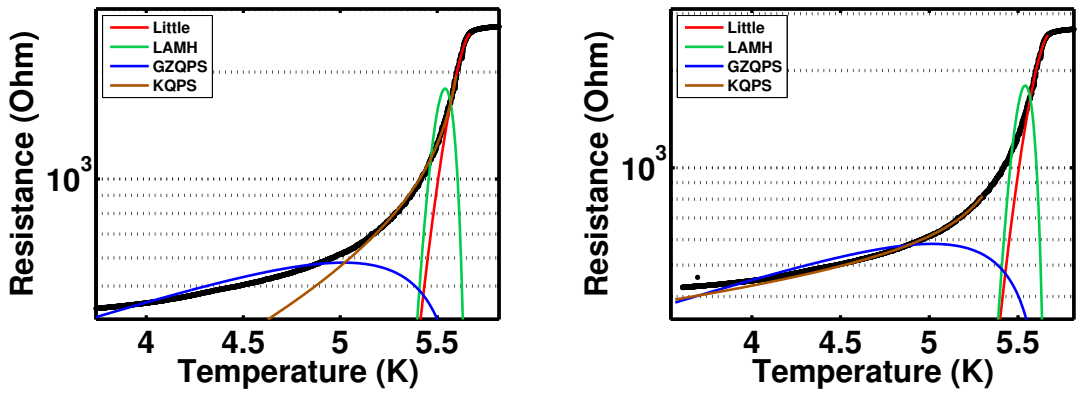

Figure 4.27: Fits to $R(T)$ data for sample S1. The KQPS fit differs between the graphs.

phase slip models were expanded and rearranged to give the equations

$$R_{Little}(T) = R_N \exp\left[-\left(\frac{\sqrt{2}\pi h}{12e^{\gamma}e^{*2}}\right)\frac{l}{R_N}\frac{(1-t)^{3/2}}{t}\right], \tag{4.1}$$

$$R_{LAMH}(T) = \left(\frac{h}{e^{*3}}\sqrt{\frac{\sqrt{2}h}{3e^{\gamma}\pi}}\right)\sqrt{\frac{l^3}{R_N}}\frac{(1-t)^{9/4}}{t(3/2)}\exp\left[-\left(\frac{\sqrt{2}\pi h}{12e^{\gamma}e^{*2}}\right)\frac{l}{R_N}\frac{(1-t)^{3/2}}{t}\right], \tag{4.2}$$

$$R_{GZQPS}(T) = (ABR_Q^2)\frac{l^2}{R_N}(1-t)\exp\left[-(AR_Q)\frac{l}{R_N}(1-t)^{1/2}\right], \tag{4.3}$$

$$R_{KQPS}(T) = R_N \exp\left[-\frac{3.878\times10^{-19}}{R_N}\frac{(1-t)^{1/2}}{t}\tanh\left(1.217\times10^{-23}\frac{(1-t)^{1/2}}{t}\right)\right], \tag{4.4}$$

where $l = L/\xi(0)$ and $t = T/T_c$. R_N and l were used as automated fitting parameters, with T_c manually chosen and fitted. The parameters $A = 3$ and $B = 5.1$ were chosen for the GZQPS model following Ref. [34].

Figure 4.27 shows fits of the Little, LAMH, GZQPS and KQPS models of phase slips to $R(T)$ data from sample S1. The Little model fits well over a small range near T_c but deviates strongly further away - this is expected, as the sample has a very strong resistive tail below T_c which TAPSs does not predict. The LAMH and GZQPS models are harder to obtain fits to.

Interestingly, the KQPS model provides a good fit in Figure 4.27(a) from close to T_c down to $0.9T_c$. The model is applicable in regimes where the QPS rate is low, so

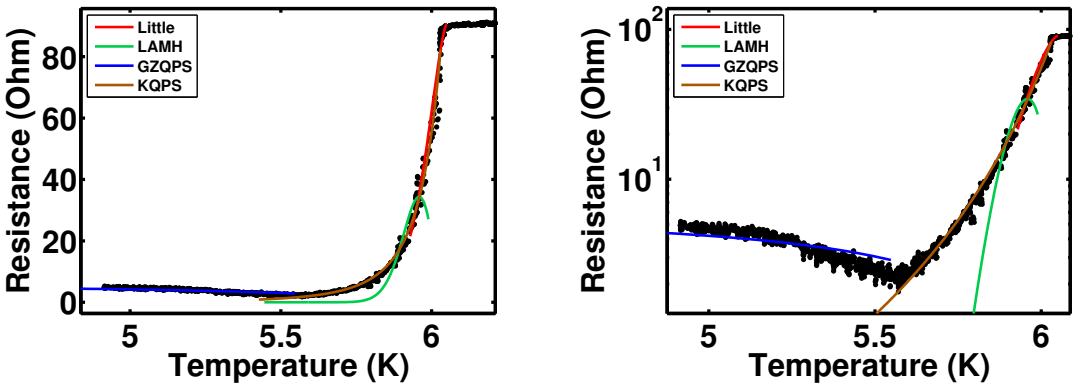

Figure 4.28: Fits to $R(T)$ data for sample S7, plotted on a (a) normal and (b) log scale.

it is not implausible that such a model could explain the resistance here. However it too predicts a smaller tail than is observed. The fit in this figure was obtained using a fitting parameter of $T_c = 5.6K$, which appears close to the true value. If this value is relaxed to $T_c = 5.3$, the fit in Figure 4.27(b) is obtained; in this case, the KQPS model predicts a tail much closer to what is observed.

Figure 4.28 shows phase slip model fits to $R(T)$ data from sample S7. Once again, the Little and KQPS models provide the best fits to the data. The GZQPS model also begins to match the curvature at low temperatures, and a better fit could potentially be obtained with a more accurate fitting mechanism. It is therefore possible that QPSs explain the low-temperature non-zero resistance; the dip in resistance that is observed in a number of the samples could then be due to a balance between the TAPS and QPS rates, with a minimum resistance occuring at a temperature where both rates are low.

Figure 4.29 shows phase slip model fits to the quasi-re-entrant $R(T)$ data from sample S11. While the region close to T_c is again fitted well by the Little and KQPS models, the GZQPS model alone cannot match the more or less linear $R(T)$ dependence of the low-temperature resistance. Given that the the TAPS and QPS rates are additive, and following Equation 2.35, two combined fits are made by adding the resistance contributions from the Little and GZQPS models (Figure 4.29(a)), and the GZQPS and KQPS models (Figure 4.29(b)). The Little/GZQPS combined fit shows a clear improvement over the pure GZQPS fit, but still fails to match the observed curvature. By contrast, the combined GZQPS/KQPS model fits the low-temperature resistance

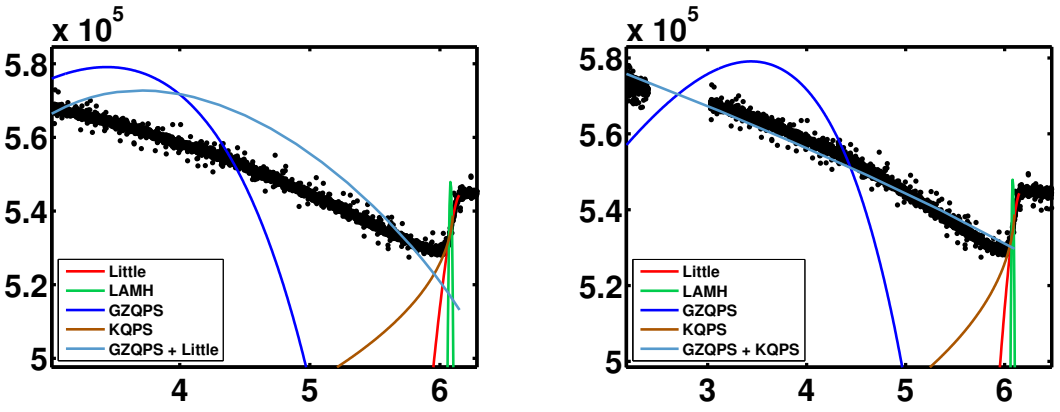

Figure 4.29: Fits to $R(T)$ data for sample S11. The combined fit differs between the graphs.

much more closely. While this is not conclusive proof that QPSs is the cause of the quasi-re-entrant behaviour, it shows that QPSs is consistent with such behaviour.

As mentioned previously, the literature explanation [10, 13] is that there is a lack of global phase coherence through the sample due to the absence of a spanning island and proliferation of tunneling gaps between adjacent islands, and these tunneling gaps act as Josephson junction weak links. The systems examined in the experimental literature with regard to superresistive and quasi-re-entrant effects are generally "discontinuous films " [10, 12], which are very granular - a common theoretical model used to approximate such films is a two-dimensional array of Josephson junctions [15]. This picture is not necessarily incompatible with phase slips; non-zero resistances in ultrathin nanowires have been attributed to QPSs [16]. The granular disconnected films are very different to the smooth homogeneous nanowires in terms of morphology, and so it could be speculated that the films studied here have an intermediate behaviour due to their intermediate connectivity.

In addition to the phase slip fits above, the $R(T)$ curves can be examined for evidence of a BKT transition. Figure 4.30 shows an example fit of the HN formula to an $R(T)$ curve for sample S5. The best fit was obtained for $T_{BKT} = T_c = 6.725$K - i.e. when the BKT transition coincides with the superconducting transition. Other $R(T)$ curves provided similar fits to the HN formula, suggesting that the observed transitions in the $R(T)$ curves were all superconducting transitions rather than BKT transitions.

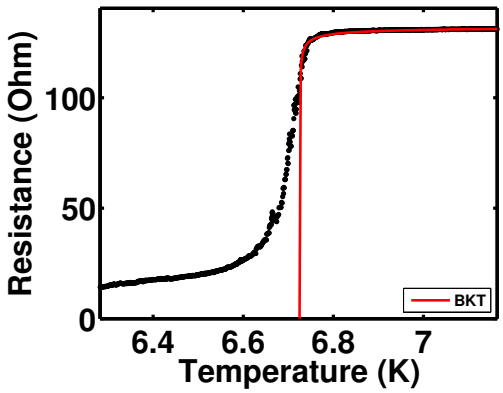

Figure 4.30: BKT fit to $R(T)$ data for sample S5.

Section 4.5.3.1 below covers this further.

4.5.3 $V(I)$ analysis

Several of the theoretical models examined in Chapter 2 predict observable effects in $V(I)$ or $R(I)$ data:

- Phase slip centres
- Hotspots
- Vortices
- Shapiro steps

Shapiro steps can reasonably be ruled out as causing any of the observed effects - none of the data groups examined show any sign of regularly spaced voltage plateaus. Additionally, there is no obvious source of microwave radiation.

4.5.3.1 Vortices

While the presence of hotspots and PSCs can be inferred by examining the various steps and discrete transitions in the $V(I)$ data (see Sections 4.5.3.2 and 4.5.3.3 respectively), the presence of vortices can be inferred by fitting curves to the low-current regions of the $V(I)$ data which do not exhibit such discontinuities.

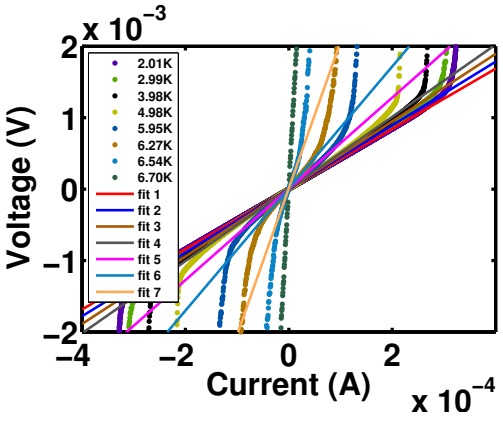

Figure 4.31: Linear fits to low-current $V(I)$ data for sample S5 from group 2.

T (K)	Slope	Intercept	R-square
2.01	4.215	4.704e-007	1
2.99	4.455	2.109e-006	1
3.98	4.727	2.607e-006	0.9997
4.98	5.05	2.11e-006	0.9996
5.95	6.388	3.56e-006	0.9999
6.27	8.547	7.504e-006	0.9999
6.54	20.49	1.226e-005	0.9991

Table 4.2: Parameters for the linear fits in Figure 4.31

The presence of a BKT transition can be determined by examining the low-current region of $V(I)$ curves; as described in Section 2.7.2, a power-law behaviour is expected below T_{BKT} with an exponent $\alpha \geq 3$, while above T_{BKT} linear behaviour is expected (equivalent to a power law with $\alpha = 1$). Therefore, a clear change in the calculated exponent for power-law fits would be observed.

Figure 4.31 shows linear fits to the low-current regime of sample S5. The fitting was done using the Matlab curve fitting toolbox. Power-law fits were also made resulting in exponents very close to 1, but the fits were of lower quality (the R values for all linear fits were above 0.999). There is clearly no evidence of a BKT transition, as the linear fits are equivalent to a power-law fit with an exponent of 1, and a BKT transition would manifest in the low-current $V(I)$ data as an increase to exponents above 3 as the temperature decreased below T_{BKT}.

The above fits suggest that any BKT transition in the film would have to occur below the measured temperatures, since there is no indication of an exponent higher than 3 in the measured range. While this is not inconsistent with BKT theory (as T_{BKT} can be well below T_c [58]) the $R(T)$ fits (such as Figure 4.30) indicate that T_{BKT} is very close to T_c, and the majority of the temperature range would be below the BKT transition; these two viewpoints are clearly incompatible. Thus, no clear experimental signature of vortices is observed in the percolating films.

Does it make sense that vortices would not form? BKT transitions are a 2D phenomenon, whereas the percolating films considered here have a dimensionality between

1 and 2. It could be argued that vortices (whether due to an external magnetic field or thermally-created magnetic loops) would be less likely to form in a superconducting percolating film - given the incomplete surface coverage, the magnetic field would be more likely to penetrate the unoccupied regions surrounding the islands rather than suppressing the superconductivity within the islands themselves. It was mentioned in Section 2.8 that vortex flux-flow in two-dimensional systems are equivalent to phase slips in one-dimensional systems; hence an alternative possibility is that vortices do form in the percolating samples, but the flux-flow of vortices across the sample manifests as a contribution to the phase slip rate.

4.5.3.2 Hysteresis

Samples in both group 1 and group 3 exhibited hysteresis in the $R(I)$ curves shown in Section 4.4.1 (Figures 4.21(b) and 4.23(a)). The observed hysteresis between increasing and decreasing $|I|$ in the $R(I)$ curves fits qualitatively to a picture where a hotspot forms at some point on increasing $|I|$ (either from a PSC or from the local critical current being exceeded in some region), after which the hotspot maintains the sample in the normal state until $|I|$ decreases below the minimum hotspot current I_h.

As mentioned in Section 2.5, there are two different approximations for I_h depending on whether the wire the hotspot forms on is "long" (Figure 2.17) or "short" (Figure 2.18). The percolating samples created in this research would be better described by the "short" model, with the "wire" being the necks between adjacent islands. By taking the SBT hotspot model for "short" wires (Equation 2.48) and using values of I_h determined from the $R(I)$ curves such as in Figure 4.23, estimates for the thickness of the junction causing the hotspot can be obtained.

Table 4.3(a) shows the theoretical wire thicknesses that would result in values of I_h corresponding to the sudden drops in resistance observed in the down ramp for sample S8 in Figure 4.23(d). The sizes appear consistent with the morphology of sample S8 (Figure 4.1(b)), with the critical points being the necks between pairs of clusters.

Table 4.3(b) shows the same calculations for the currents where hysteresis ends on the down ramps of Sample S3. The hysteresis here is not nearly as prominent as for the group 3 samples - even though the hysteresis is visible over a 200μA range, the up and down ramps differ at most by 500Ω (for the lowest temperature). The predicted critical neck thicknesses are very small, indicating that the hysteresis is likely

(a)

T (K)	I_h (μA)	d (nm)
2.01	340.9	13.1
3.05	319.4	14.3
4.07	281.4	15.5
5.07	208.9	16.6
5.28	184.3	16.7
5.51	150.9	16.5

(b)

T (K)	I_h (μA)	d (nm)
1.99	47.4	1.7
3.03	56.4	2.3
4.17	53.2	2.6
5.27	57.4	3.7

Table 4.3: Theoretical wire thicknesses predicted to give the minimum hotspot currents observed for samples (a) S8 from group 3 (Figure 4.23) ($T_c = 6.0$K) and (b) S3 from group 1 (Figure 4.21) ($T_c = 6.66$K), using the "short" wire approximation with $K = 35.3\text{Wm}^{-1}\text{K}^{-1}$ and $\rho = 208\Omega$nm.

caused by one or more small, localised hotspots rather than a single global hotspot; the thermal spreading of the hotspots could be inhibited by the lead oxide, which has a much lower thermal conductivity (between $0.6\text{Wm}^{-1}\text{K}^{-1}$ and $4.3\text{Wm}^{-1}\text{K}^{-1}$) and much higher electrical resistivity ($10 - 15\Omega$cm) [74].

None of the group 2 samples showed any hysteresis. A potential reason for this is their high degree of coalescence; the thermal conductance of the films with large islands is greater than that of the less coalesced films because of the larger cross-sectional area of the connections, meaning that a much larger current is required to sustain the hotspot. For example, a thickness of 100nm results in $I_h = 2.26$mA at $0.5T_c$, far higher than the bias currents applied to the group 2 samples.

There was some hysteresis evident in some of the group 4 samples (as shown in Figure 4.26). Unlike groups 1 and 3, there are no clearly-defined critical currents or minimum hotspot currents; however, the fact that the hysteresis only occurs on the highest current ramps implies that it is still likely caused by hotspots. The critical current would therefore lie somewhere between 200μA and 300μA, while the minimum hotspot current would be about 150μA (where the up and down ramp curves "recombine"). The theoretical thickness corresponding to $I_h = 150\mu$A (using $T = 3.05$K and $T_c = 6.08$K) is 6.6nm, which is just under half the diameter predicted for the group 3 samples; this appears consistent with the fact that the coverage is much lower and the islands further apart, so any critical necks between them would have a smaller

minimum diameter.

4.5.3.3 Smooth and discrete steps

As mentioned in Section 4.4, a variety of steps were observed in the $R(I)$ curves. The steps can be split into two categories: discrete jumps in resistance (see e.g. Figure 4.21(a)), and smoother steps which develop over a few μA (e.g. Figure 4.21(d)).

An observation universal to both types of steps is that as the temperature increases, the current at which each step occurs decreases. This provides strong evidence that the steps are caused by (or related to) the bias current exceeding some local critical current in the sample - the critical current decreases to zero as the temperature is increased to T_c.

The discrete steps only seem to appear at medium to high currents in the ranges of measurement (e.g. above 50μA for sample S3). By contrast, the smooth steps are more prominent at lower currents. If the current the step occurs at is taken to be the local critical current of some neck in the sample, then the smoother steps occur in narrower necks. It could be speculated that the narrower neck leads to a broadening of the step, possibly through a difference in homogeneity of the neck; this might provide a consistent explanation for the different forms of steps in terms of a single phenomenon.

While the discrete steps are repeatable (the same steps occur in both the down and up ramps on increasing $|I|$, as shown in Figure 4.21(a)), they are not regular (the exact stepping current differs between down and up ramps). This could be due to small local temperature differences (from localised heating or an inhomogeneous temperature profile) causing a slight shift in the local critical current.

There are two phenomena that could potentially result in this behaviour: PSCs and hotspots. As described in Section 2.5, hotspots are defined by two currents - the critical current I_c required to create the hotspot, and the minimum current I_h that can maintain the hotspot. Generally $I_h < I_c$, resulting in hysteresis in the $V(I)$ curve (as discussed in Section 4.5.3.2). Localised hotspots could potentially show stepping behaviour, however, if $I_h \approx I_c$; this would mean that the hotspot would develop on increasing $|I|$ at the same magnitude at which it is extinguished on decreasing $|I|$, showing no hysteresis. However, it is unlikely that $I_h \approx I_c$ everywhere in the sample, so even if some steps are explained by this, an alternative proposal is necessary.

	Smooth		Discrete	
Sample	R_{min} (Ω)	R_{max} (Ω)	R_{min} (Ω)	R_{max} (Ω)
S1	121	260	23	156
S2	120	444	31	51
S3	103	1018	57	289
S5	1.4	22.8		
S6	0.8	2.3		
S8	6.4	40.0	4	56.1
S9	27.9	257	59	240

Table 4.4: Ranges of step sizes observed in samples from groups 1 and 2.

PSCs manifest as localised resistive segments that "switch on" when some local critical current I_c is surpassed. As such, they are perfectly suited to explain the observed steps. The resistance step caused by a single PSC in a uniform wire is (from Equation 2.44)

$$\frac{dV}{dI} = \frac{2\Lambda\rho}{A}. \tag{4.5}$$

When considering current-biased measurements, the literature shows PSCs to have a discrete step shape [44, 47, 48]. While the following analysis applies the PSC model to both forms of observed steps, it is unclear at present whether it makes sense physically to describe the smooth steps in terms of PSCs - as mentioned above, there would need to be some mechanism which caused a broadening of the discrete steps at low currents, and whether such a mechanism is possible for PSCs is currently unknown.

Table 4.4 gives the ranges of step sizes for some of the group 1, 2 and 3 samples. There is a large spread in resistance values, but some noticeable trends. The step sizes for the group 2 samples are much smaller than for the group 1 samples; this is consistent with the steps being caused by local resistive segments, as the cross-sectional area of the coalesced islands in the group 2 samples is much larger than the necks between touching clusters for the other groups. Alternatively, the cause could be an increase in effective resistivity at the narrower cluster-to-cluster necks, or more likely a combination of the two effects. The discrete steps also tend to be smaller than the smooth steps.

The group 3 samples are comparable to the group 1 samples in terms of discrete steps, but the smooth steps from group 3 are generally smaller than in group 1. This

implies that the smallest necks in the group 3 samples are larger than the smallest necks in the group 1 samples, which is at odds with their similar morphology but can be resolved by taking into account the oxide layer in the group 1 samples (covered below).

The expected step sizes due to PSCs can be compared to the observed steps by making a few assumptions about the relevant parameters. The quasiparticle diffusion length for Pb whiskers has been experimentally determined to be $2\Lambda \approx 15 - 20\mu$m [75], and the resistivity can be approximated by the bulk resistivity for lead, $\rho = 208\Omega$nm. Both of these values are expected to differ in percolating films; the resistivity would likely increase because the percolating films are much more constrained than bulk solids, while Λ would likely decrease due to the films not having the long-range uniformity that the Pb whiskers do, meaning that the quasiparticles cannot diffuse as far.

It is possible that these changes to Λ and ρ in a percolating film cancel out - as mentioned in Section 2.4.3, Λ is dependent on the ordinary mean free path and the mean free path for inelastic scattering, and the resistivity can be defined in terms of various forms of scattering [76]. The variations in cross-sectional area would not be expected to affect the mean free paths as much as the overall geometry, and so could potentially be factored out. Further theoretical analysis would be required to determine whether one value dominates over the other in magnitude.

The cross-sectional area A depends on the location of the PSC. In a percolating system such as these samples, the most likely place for a PSC to occur is at the necks between clusters, or narrow regions of the coalesced islands - the current density at these points is higher than in other regions of the sample because the cross-sectional area is smaller. Given the varying morphologies of the samples and the corresponding variability in the cross-sectional areas, there are a range of possible values for Λ. Table 4.5 gives a range of different possible neck diameters and the corresponding PSC resistance (based on the other values given above).

There is a large variance in the possible values - the predicted PSC resistance increases drastically as the cross-sectional area is decreased. However, the value used for Λ is far greater than even the sizes of the coalesced islands (as is evident from the scale bar on Figure 4.1). As discussed above, Λ will likely be much smaller in the restricted morphology of the percolating film. It appears that the resistivity is not as dominant as Λ in Equation 2.44; to give step sizes for the smaller areas comparable to

Neck diameter (nm)	Area (nm^2)	Resistance (Ω)
20	314	10593
50	1963	1695
100	7854	424

Table 4.5: Theoretical resistances for a single PSC for $\Lambda = 8\mu$m and $\rho = 208\Omega$nm.

those observed, Λ would need to decrease by several orders of magnitude more than ρ increased.

The above analysis can be applied in reverse - by taking resistance steps from the observed samples, the corresponding quasiparticle diffusion length can be estimated assuming bulk resistivity and an appropriate cross-sectional area (see below). Table 4.6 shows Λ values for median resistance steps (both smooth and discrete) taken from samples in groups 1, 2 and 3 at the lowest recorded temperatures. Neither discrete nor smooth steps were observed in the group 4 samples.

For the group 2 samples, a cross-sectional area corresponding to a diameter of 30nm was used, obtained from averaging measurements of constrictions from SEM images of the group 2 samples. The cross-sectional area for the group 1 and 3 samples was estimated to have a neck diameter of 15nm; this was chosen based on the neck diameter estimates obtained for the group 3 samples (which are morphologically similar to the group 1 samples as discussed in Section 4.1) from the hysteresis analysis in the previous section. Neck diameters could not be estimated from the SEM images of the group 1 and 3 samples because the necks could not be resolved.

The estimated values for Λ are considerably smaller than the value for Pb whiskers [75], as was predicted to be the case. The values for group 3 are on the order of the size of a cluster, which seems reasonable given the uncoalesced nature of the samples. As previously mentioned, the applicability of PSCs to smooth steps is unknown, so the fact that only smooth steps were observed for group 2 means that the smaller Λ values compared to group 3 may not be entirely meaningful - if anything, Λ would be expected to be larger in the more coalesced samples.

The estimated Λ values for group 1 are noticeably larger than the estimates for groups 2 and 3. This is not consistent with the similarity in morphology to the group 3 samples, but can be explained: the resistivity of lead oxide ($1 - 1.5 \times 10^8\Omega$nm [74]) is

		Smooth		Discrete	
Sample	T (K)	R (Ω)	Λ (nm)	R (Ω)	Λ (nm)
S1	1.98	179	304.15	86	146.13
S2	1.92	235	398.46	34.5	58.62
S3	1.99	793	1347.4	233	395.91
S5	2.01	14.3	97.19		
S6	5.59	1	6.80		
S8	2.01	19.9	33.79	15.1	25.66
S9	3.05	85.7	145.62	109.2	185.55

Table 4.6: Calculated Λ values for median step sizes from samples from groups 1 and 3 ($d = 15$nm) and group 2 ($d = 30nm$) for $\rho = 208\Omega$nm.

much larger than pure lead (208Ωnm). It is therefore unlikely that conduction will take place through the lead oxide shell that the group 1 samples have. Assuming that the "neck" between adjacent clusters consisted of a neck of pure lead with a surrounding oxide layer, the cross-sectional area of the conducting pathway would be smaller than the overall neck area, leading to lower Λ estimates for group 1.

5

Conclusion

In this thesis, a study of the superconductive and superresistive properties of thin percolating films was presented. Samples were prepared by depositing lead nanoclusters onto a substrate between two gold contacts; $R(T)$ and $V(I)$ measurements were made on the resulting films. A variety of characteristic behaviours were exhibited, ranging from discrete and smooth steps in the $V(I)$ curves to large non-zero resistances below the superconducting transition temperature (which for the last group of samples were larger than their normal-state resistances).

The results presented here show that phase slips, PSCs and hotspots are all viable candidates for explaining the observed characteristics. Further analysis is needed however with regard to which aspects of both one and two-dimensional theoretical models can be applied to percolating films with intermediate dimensionality.

The presence of vortices in these samples has been reasonably ruled out, based on the fact that none of the expected characteristics for vortices or BKT transitions have been observed. Phase slips, on the other hand, have been shown to be compatible with much of the observed behaviour.

The phase slip models were consistent with the behaviour exhibited in the $R(T)$ curves of most of the samples, including the quasi-re-entrant behaviour which was previously attributed in the literature to a decrease in global coherence of the superconducting order parameter across the samples. It is unclear whether phase slips (in particular QPSs) can physically explain superresistive behaviour; an infinite resistance at 0K would tend to imply an infinite phase slip rate. None of the samples presented

here exhibited true superresistivity but instead approached finite (if large) resistances at 0K, so no experimental conclusions specifically about superresistivity could be drawn.

It is proposed that the steps observed in the $R(I)$ curves were caused by localised PSCs forming in narrow regions within the percolating film such as the necks between adjacent clusters. The experimental literature shows PSCs manifesting as discrete steps in $R(I)$ curves, which is consistent with the discrete steps observed here but not with the smooth steps. Whether a "broadened" step could result from a PSC is unclear, and requires further thought. The hysteresis observed in the $R(I)$ curves is consistent with the formation of hotspots within the percolating film, in most cases developing from an earlier PSC.

It is clear that there is still considerable work to be done in order to fully understand the processes occuring within these random percolating networks. In the first instance, a more solid theoretical understanding of the effects of the unique geometrical constraints of percolating films on the various one and two-dimensional phenomena is required. This thesis leaves several open questions:

- How can quantities like the quasiparticle diffusion length be defined in percolating films?
- Are phase slips sufficient to explain the quasi-re-entrant behaviour exhibited by these samples?
- What is the cause of the general "shoulder" observed in the $R(I)$ curves?

This leaves plenty of scope for future work. Primarily, the preparation and analysis of more samples under a wider variety of conditions would hopefully provide further evidence of the previously-discussed phenomena. Experiments to determine the quasiparticle diffusion length and the resistivity within these films would enable a more accurate picture of PSCs in percolating films to be developed; likewise, studies of the thermal conduction properties of percolating films would place more effective bounds on the possibility of localised hotspots within the film. Additionally, by constraining the geometry of the substrate (e.g. with a PMMA mask) more controlled samples could be formed, insofar as percolating wires could potentially be created; such wires could then be directly compared to the various granular or smooth quasi-one-dimensional wires to which phase slips and PSCs are applied in the literature.

One interesting avenue to investigate would be incremental sample depositions - to halt deposition on a sample very early after onset, measure its $R(T)$ behaviour, and then continue deposition in increments (taking $R(T)$ measurements in between). This would enable a direct comparison of percolating films to the work presented on granular disconnected films in Refs [10, 12], which would provide deeper insight into how the conductivity of the sample and its characteristic behaviour changes as percolation progresses. Whether such an experiment is worthwile depends on what guarantee there is that both the cluster beam and the samples themselves would be stable on a timescale of hours. Standard continuous depositions generally take around twenty minutes, and the time from onset can be as long as five minutes in the 10K-deposited samples. However, the time required for a single $R(T)$ measurement is around twenty minutes, so each pause introduced into the deposition after onset would likely be as long as the total deposition would have taken. If the sample morphology changed appreciably during the pauses, or if the composition or distribution of the cluster beam were to differ over several hours compared to the original five minutes, then this approach would have no benefit over stopping a series of samples at different post-onset points (i.e. the procedude used in this research). Consequentially, such experiments would necessarily be conducted at low temperatures, where the effect of coalescence is low.

Acknowledgements

It has been seven years since I first set foot inside the Rutherford building as a first-year Physics student, and I want to thank the entire Department of Physics and Astronomy for giving me knowledge, support and opportunity. It is said that university makes for some of the best years of your life, and I couldn't have spent them with a more enjoyable and interesting group of people.

I would like to thank my supervisor Prof. Simon Brown for sharing his guidance, keen insight and limitless patience with me. I would also like to acknowledge past and present members of the research group, and thank in particular Dr. Shawn Fostner, Dr. David McKenzie, Amol Nande and Dr. Abdul Sattar, with whom I have greatly enjoyed working.

Additionally, I would like to thank Dr. Kristiaan Temst and Dr. Margriet Van Bael from K.U. Leuven, Belgium for allowing me to spend the first three months of my Masters with their research groups while the University of Canterbury recovered from the earthquakes. A big thank you goes to Dr. Thomas Picot, Dr. Christian Romero Vieyra and Kelly Houben for making me feel at home away from home.

Finally, I would like to thank my parents and friends for their general support, and for putting up with extensive discussions on the finer points of nanoscale physics!

Bibliography

[1] Michael Fosmire. **Superconductivity: a selective bibliography**. *Reference Services Review*, **28**(2):161–170, 2000. 1

[2] J Bardeen, L N Cooper, and J R Schrieffer. **Theory of superconductivity**. *Physical Review*, **108**(5):1175–1204, 1957. 3

[3] Leon Cooper. **Bound Electron Pairs in a Degenerate Fermi Gas**. *Physical Review*, **104**(4):1189–1190, 1956. 4

[4] Vitaly L Ginzburg and Lev D Landau. **Concerning the theory of superconductivity**. *Zurnal Çeksperimentalnoj i Teoreticeskoj Fiziki*, **20**(12):1064–1082, 1950. 5

[5] Michael Tinkham. *Introduction to superconductivity*. Dover books on physics. Dover Publications, 2004. v, vi, vii, 5, 6, 7, 8, 9, 14, 23, 28, 30, 40, 41

[6] L. P. Gor'kov. **Microscopic derivation of the Ginzburg-Landau equations in the theory of superconductivity**. *Sov. Phys. JETP*, **9**:1364, 1959. 6

[7] A A Abrikosov. **On the Magnetic Properties of Superconductors of the Second Group**. *Soviet Physics JETP*, **5**(6):1174, 1957. 8

[8] B D Josephson. **Supercurrents through barriers**. *Advances in Physics*, **14**(56):419, 1965. 8, 9

[9] P. W. Anderson. **Considerations on the flow of superfluid helium**. *Reviews of Modern Physics*, **38**(2), 1966. 9

[10] HM Jaeger, DB Haviland, BG Orr, and AM Goldman. **Onset of superconductivity in ultrathin granular metal films**. *Physical Review B*, **40**(1):182, 1989. v, 9, 10, 11, 12, 88, 92, 105

[11] R. C. Dynes, J. P. Garno, and J. M. Rowell. **Two-dimensional electrical conductivity in quench-condensed metal films**. *Physical Review Letters*, **40**(7):479–482, 1978.

[12] A. Gerber. **Low-temperature transport properties of granular Pb films below the percolation threshold**. *Journal of Physics: Condensed Matter*, **2**(41):8161–8172, 1990. 9, 12, 88, 92, 105

[13] Mingliang Tian, Nitesh Kumar, Moses H. W. Chan, and Thomas Mallouk. **Evidence of local superconductivity in granular Bi nanowires fabricated by electrodeposition**. *Physical Review B*, **78**(4):1–7, July 2008. v, 11, 88, 92

[14] Mingliang Tian, Jinguo Wang, Nitesh Kumar, Tianheng Han, Yoji Kobayashi, Ying Liu, Thomas E Mallouk, and Moses H. W. Chan. **Observation of superconductivity in granular bi nanowires fabricated by electrodeposition.** *Nano letters*, **6**(12):2773–80, December 2006. 11

[15] Valerii M. Vinokur, Tatyana I. Baturina, Mikhail V. Fistul, Aleksey Yu Mironov, Mikhail R. Baklanov, and Christoph Strunk. **Superinsulator and quantum synchronization.** *Nature*, **452**(7187):613–5, April 2008. 12, 92

[16] Alexey Bezryadin, C. N. Lau, and M. Tinkham. **Quantum suppression of superconductivity in ultrathin nanowires**. *Nature*, **404**(6781):971–4, April 2000. 12, 25, 26, 92

[17] J. S. Langer and Vinay Ambegaokar. **Intrinsic Resistive Transition in Narrow Superconducting Channels**. *Physical Review*, **164**(2):498–510, 1967. v, 13, 14, 17, 18, 21

[18] KK Likharev. **Superconducting weak links**. *Reviews of Modern Physics*, **51**(1), 1979. 13

[19] R. A. Ferrell. **Possibility of one-dimensional superconductivity**. *Physical Review Letters*, **13**(10), 1964. 13

[20] T. M. Rice. **Superconductivity in one and two dimensions**. *Physical Review*, **576**(1956):1889–1891, 1965. 13

[21] WA Little. **Decay of persistent currents in small superconductors**. *Physical Review*, **156**(2):396, 1967. v, 13, 14, 15, 16, 17

[22] Alexey Bezryadin. **Quantum suppression of superconductivity in nanowires**. *Journal of Physics: Condensed Matter*, **20**(4):043202, January 2008. vi, 13, 17, 22

[23] P. G. de Gennes. *Superconductivity of metals and alloys*. Benjamin, New York, 1966. 16

[24] D E McCumber and B I Halperin. **Time Scale of Intrinsic Resistive Fluctuations in Thin Superconducting Wires**. *Physical Review B*, **1**:1054, 1970. 17, 18, 19

[25] P. W. Anderson and A. H. Dayem. **Radio-frequency effects in superconducting thin film bridges**. *Physical Review Letters*, **13**(6):195–197, 1964. 17

[26] W. W. Webb and R. J. Warburton. **Intrinsic quantum fluctuations in uniform filamentary superconductors**. *Physical Review Letters*, **20**(9):461–465, 1968. 19, 20

[27] K. Yu. Arutyunov, D. S. Golubev, and A. D. Zaikin. **Superconductivity in one dimension**. *Physics Reports*, **464**(1-2):1–70, July 2008. 19

BIBLIOGRAPHY

[28] Dmitri Golubev and Andrei Zaikin. **Thermally activated phase slips in superconducting nanowires**. *Physical Review B*, **78**(14):1–8, October 2008. 19

[29] Jian Wang, XC Ma, Yun Qi, Shuai-hua Ji, and YS Fu. **Dissipation in an ultrathin superconducting single-crystal Pb nanobridge**. *Journal of Applied Physics*, **106**:2–5, 2009. v, 20, 21

[30] Sang Chu, Anthony Travis Bollinger, and Alexey Bezryadin. **Phase slips in superconducting films with constrictions**. *Physical Review B*, **70**(21):1–6, December 2004. vi, 19, 20, 21, 22, 44

[31] R. S. Newbower, M. R. Beasley, and M. Tinkham. **Fluctuation effects on the superconducting transition of tin whisker crystals**. *Physical Review B*, pages 864–868, 1972. 20

[32] Mingliang Tian, Jinguo Wang, James Kurtz, Ying Liu, M. Chan, Theresa Mayer, and Thomas Mallouk. **Dissipation in quasi-one-dimensional superconducting single-crystal Sn nanowires**. *Physical Review B*, **71**(10):1–7, March 2005. 20

[33] Maciek Zgirski, Karri-Pekka Riikonen, Vladimir Touboltsev, and Konstantin Arutyunov. **Size dependent breakdown of superconductivity in ultranarrow nanowires.** *Nano letters*, **5**(6):1029–33, June 2005. 20, 21, 27, 87

[34] Myung-Ho Bae, Robert C Dinsmore, Thomas Aref, Matthew Brenner, and Alexey Bezryadin. **Current-phase relationship, thermal and quantum phase slips in superconducting nanowires made on a scaffold created using adhesive tape.** *Nano letters*, **9**(5):1889–96, May 2009. vi, 20, 21, 25, 26, 27, 87, 90

[35] Anthony Travis Bollinger, A. Rogachev, and Alexey Bezryadin. **Dichotomy in short superconducting nanowires: Thermal phase slippage vs. Coulomb blockade**. *Europhysics Letters (EPL)*, **76**(3):505–511, November 2006. 20

[36] Dganit Meidan, Yuval Oreg, and Gil Refael. **Sharp Superconductor-Insulator Transition in Short Wires**. *Physical Review Letters*, **98**(18):1–4, May 2007. 20, 21, 27

[37] M. Tinkham and C. N. Lau. **Quantum limit to phase coherence in thin superconducting wires**. *Applied Physics Letters*, **80**(16):2946, 2002. 21

[38] N. Giordano. **Evidence for macroscopic quantum tunneling in one-dimensional superconductors**. *Physical Review Letters*, **61**(18):4–7, 1988. vi, 23, 24

[39] Anthony Travis Bollinger. *Superconductor-Insulator Transition in Quasi-One-Dimensional Nanowires*. PhD thesis, University of Illinois at Urbana-Champaign, 2005. 25

[40] Fabio Altomare, A. Chang, Michael Melloch, Yuguang Hong, and Charles Tu. **Evidence for Macroscopic Quantum Tunneling of Phase Slips in Long One-Dimensional Superconducting Al Wires**. *Physical Review Letters*, **97**(1):5–8, July 2006. 25

[41] C. N. Lau, N. Markovic, M. Bockrath, A. Bezryadin, and M. Tinkham. **Quantum Phase Slips in Superconducting Nanowires**. *Physical Review Letters*, **87**(21):19–22, November 2001. 25

[42] Dmitri Golubev and Andrei Zaikin. **Quantum tunneling of the order parameter in superconducting nanowires**. *Physical Review B*, **64**(1):1–14, June 2001. 25, 26

[43] S. Khlebnikov. **Quantum phase slips in a confined geometry**. *Physical Review B*, **77**(1):1–8, January 2008. 25

[44] W. J. Skocpol, M. R. Beasley, and M. Tinkham. **Phase-Slip Centers and Nonequilibrium Processes in Superconducting Tin Microbridges**. *Applied Physics*, **16**:145–167, 1974. vi, vii, 28, 29, 30, 31, 33, 44, 98

[45] G. J. Dolan and L. D. Jackel. **Voltage measurements within the nonequilibrium region near phase-slip centers**. *Physical Review Letters*, **39**(25):1628–1631, 1977. vi, 29

[46] M. Tinkham. **The Interaction of Phase-Slip Centers in Superconducting Filaments**. *Journal of Low Temperature Physics*, **35**:147–151, 1979. 30

[47] J. Meyer. *Unpublished.* PhD thesis, University of Cologne, 1973. vii, 31, 33, 98

[48] S. Michotte, S. Mátéfi-Tempfli, L. Piraux, D. Vodolazov, and F. Peeters. **Condition for the occurrence of phase slip centers in superconducting nanowires under applied current or voltage**. *Physical Review B*, **69**(9):1–12, March 2004. vi, 31, 98

[49] Jian Wang, Yi Sun, Mingliang Tian, Bangzhi Liu, and Meenakshi Singh. **Superconductivity in single crystalline Pb nanowires contacted by normal metal electrodes**. *Arxiv preprint*, pages 4–9, 2012. vi, 31, 32

[50] W. J. Skocpol, M. R. Beasley, and M. Tinkham. **Self-heating hotspots in superconducting thin-film microbridges**. *Journal of Applied Physics*, **45**(9):4054, 1974. vii, 34, 36, 37

[51] R. Tidecks and T. Werner. **Continuous change from weak to strong coupling behavior in quasi-one-dimensional superconductors**. *Journal of Low Temperature Physics*, **65**:151–184, 1986.

[52] S Adam, L Piraux, S Michotte, D Lucot, and D Mailly. **Stabilization of non-self-spreading hotspots in current- and voltage-biased superconducting NbN microstrips**. *Superconductor Science and Technology*, **22**(10):105010, October 2009. 36

[53] S. Shapiro. **Josephson currents in superconducting tunneling: The effect of microwaves and other observations**. *Physical Review Letters*, **1**(2), 1963. vii, 37, 38

[54] R. C. Dinsmore, Myung-Ho Bae, and A. Bezryadin. **Fractional order Shapiro steps in superconducting nanowires**. *Applied Physics Letters*, **93**(19):192505, 2008. vii, 38

[55] J. Cuevas, J. Heurich, a. Martín-Rodero, a. Levy Yeyati, and G. Schön. **Subharmonic Shapiro Steps and Assisted Tunneling in Superconducting Point Contacts**. *Physical Review Letters*, **88**(15):3–6, March 2002. 37

[56] I Giaever. **Detection of the ac Josephson Effect**. *Physical Review Letters*, **14**(22):904–906, 1965. 38

[57] Lin He, Jian Wang, and Moses H. W. Chan. **Shapiro Steps in the Absence of Microwave Radiation**. *Arxiv preprint*, pages 1–5, 2011. 38

[58] Benjamin John Ruck. *Vortex Dynamics and Instabilities in Ta_x Ge_{1-x}/Ge Multilayers*. PhD thesis, Victoria University Wellington, 1998. vii, 41, 42, 94

[59] V L Berezinskii. **Violation of long range order in one-dimensional and two-dimensional systems with a continuous symmetry group. I. Classical systems**. *Zhurnal Eksperimentalnoi I Teoreticheskoi Fiziki*, **59**(3):907–920, 1970. 42

[60] V L Berezinskii. **Destruction of long-range order in one-dimensional and two-dimensional systems with a continuous symmetry group. II. Quantum systems**. *Journal of Experimental and Theoretical Physics*, **61**(3):610, 1971. 42

[61] J.M. Kosterlitz and D.J. Thouless. **Ordering, metastability and phase transitions in two-dimensional systems**. *Journal of Physics C: Solid State Physics*, **6**:1181, 1973. 42

[62] AM Kadin, K. Epstein, and AM Goldman. **Renormalization and the Kosterlitz-Thouless transition in a two-dimensional superconductor**. *Physical Review B*, **27**(11):6691, 1983. vii, 42, 43, 44

[63] B. I. Halperin and David R. Nelson. **Resistive transition in superconducting films**. *Journal of Low Temperature Physics*, **36**(D):599–616, 1979. 43

[64] A. F. Hebard and A. T. Fiory. **Critical-exponent measurements of a two-dimensional superconductor**. *Physical Review Letters*, **50**:1603–1606, 1983. 43

[65] AT Fiory and AF Hebard. **Superconducting phase transitions in indium/indium-oxide thin-film composites**. *Physical Review B*, **28**(9):5075, 1983. 44

[66] AF Hebard and AT Fiory. **Evidence for the Kosterlitz-Thouless transition in thin superconducting aluminum films**. *Physical Review Letters*, **44**(4):291–294, 1980. 44

[67] S. R. Broadbent and J. M. Hammersley. **Percolation Processes**. *Mathematical Proceedings of the Cambridge Philosophical Society*, **53**(3):629 – 641, 1957. 45

[68] Richard Zallen. *The Physics of Amorphous Solids*. John Wiley & Sons, Inc., 1983. 45, 46

[69] Edward T. Gawlinski and H. Eugene Stanley. **Continuum percolation in two dimensions: Monte Carlo tests of scaling and universality for non-interacting discs**. *Journal of Physics A: Mathematical*, **291**, 1981. vii, 46

[70] M. Schulze, S. Gourley, Simon A. Brown, and A. Dunbar. **Electrical measurements of nanoscale bismuth cluster films**. *The European Physical*, 2003. 47

[71] René Reichel, Jim G. Partridge, Alan D. F. Dunbar, Simon A. Brown, Owen Caughley, and Ahmad I. Ayesh. **Construction and Application of a UHV Compatible Cluster Deposition System**. *Journal of Nanoparticle Research*, **8**(3-4):405–416, June 2006. 50, 51

[72] René Reichel. *Nano Scale Cluster Devices*. PhD thesis, University of Canterbury, 2007. viii, 52

[73] Abdul Sattar. *Electrical Characterization of Cluster Devices*. PhD thesis, University of Canterbury, 2011. 66

[74] M. Neuberger. **Lead oxide**. *Electronic Properties Information Center*, 1967. 72, 96, 100

[75] B. Damaschke and R. Tidecks. **Phase-slip centers in superconducting whiskers of Pb with small concentrations of In and Bi**. *Journal of Low Temperature Physics*, **79**(3/4):117–134, 1990. 99, 100

[76] Pierre Y. Convers, Abdul Sattar, Simon A. Brown, and Shaun C. Hendy. **Power law fitting procedures: The electrical conductance of coalescing nanocluster films**. *Journal of Applied Physics*, **109**(1):014910, 2011. 99